Biol Cybern (2007) 96:615–623
DOI 10.1007/s00422-007-0152-6

ORIGINAL PAPER

Biological Cybernetics

Computational consequences of experimentally derived spike-time and weight dependent plasticity rules

Dominic Standage · Sajiya Jalil · Thomas Trappenberg

Received: 30 August 2006 / Accepted: 15 March 2007 / Published online: 28 April 2007

Abstract We present two weight- and spike-time dependent synaptic plasticity rules consistent with the physiological data of Bi and Poo (J Neurosci 18:10464–10472, 1998). One rule assumes synaptic saturation, while the other is scale free. We extend previous analyses of the asymptotic consequences of weight-dependent STDP to the case of strongly correlated pre- and post-synaptic spiking, more closely resembling associative learning. We further provide a general formula for the contribution of any number of spikes to synaptic drift. Asymptotic weights are shown to principally depend on the correlation and rate of pre- and post-synaptic activity, decreasing with increasing rate under correlated activity, and increasing with rate under uncorrelated activity. Spike train statistics reveal a quantitative effect only in the pre-asymptotic regime, and we provide a new interpretation of the relation between BCM and STDP data.

1 Introduction

Change in synaptic efficacy is believed to underlie learning and memory and has long been established in the forms of long term potentiation (LTP) (Bliss and Lømo 1973) and long term depression (LTD) (Lynch et al. 1977). Experimental and theoretical work on plasticity has addressed the dependence of plasticity on pre-synaptic firing rates (Bienenstock et al. 1982; Dudek and Bear 1992; Kirkwood et al. 1996), the timing (Levy and Steward 1983; Markram et al. 1997; Bi and Poo 1998) and interaction (Sjöström et al. 2001; Bi 2002; Froemke and Dan 2002; Izhikevich and Desai 2003; Wang et al. 2005; Froemke et al. 2006; Shah et al. 2006) of pre- and post-synaptic spikes, and initial synaptic strength or *weight* (Bi and Poo 1998; Debanne et al. 1999; Montgomery et al. 2001; Wang et al. 2005). Theoretical studies have further investigated the relationship between rate based and spike-time dependent plasticity (STDP) frameworks (Izhikevich and Desai 2003; Burkitt et al. 2004) and the conditions under which STDP rules transduce correlations among pre-synaptic spike trains into correlations between pre- and post-synaptic activity (Kempter et al. 1999; Kistler and van Hemmen 2000; Kuhn et al. 2003; Gütig et al. 2003) as required by Hebb's postulate (Hebb 1949).

Here, we focus on weight-dependent STDP rules. In Sect. 2, we derive parameters for two weight-dependent STDP rules from experimental data. We calculate asymptotic weights resulting from these rules in Sect. 3. Where earlier studies of the asymptotic consequences of STDP rules consider uncorrelated or weakly correlated pre- and post-synaptic spike trains (Kempter et al. 1999; Kistler and van Hemmen 2000; Song et al. 2000; van Rossum et al. 2000; Rubin et al. 2001; Gütig et al. 2003; Burkitt et al. 2004), we extend these analyses to the case of strongly correlated spikes, where pre-synaptic activity 'repeatedly and persistently takes part in firing' the post-synaptic cell, as proposed by Hebb. Our analysis shows that the means of equilibrium weight distributions are principally determined by the correlation and rate of pre- and post-synaptic spiking, where weights decrease with increasing rate in the correlated case. In Sect. 4, we show that our qualitative results do not depend on our choice of spike train statistics or correlation model. Furthermore, we derive a general formula for the contribution of any number of individual spikes to synaptic drift, proving that our results do not depend on a specific implementation of spike interactions, in contrast to the interpretation of Izhikevich and Desai (2003). We end Sect. 4 by showing a novel instance of rate-based BCM curves (Bienenstock et al. 1982) under STDP. These

D. Standage · S. Jalil · T. Trappenberg (✉)
Faculty of Computer Science, Dalhousie University,
6050 University Avenue, Halifax, NS, Canada B3H 1W5
e-mail: tt@cs.dal.ca

curves emerge when temporal constraints prevent weights from reaching asymptotic values at lower spike rates.

2 Weight dependence of STPD

Weight-dependent plasticity has been shown by several groups (Bi and Poo 1998; Debanne et al. 1999; Montgomery et al. 2001; Wang et al. 2005), but only Bi and Poo (1998) have done so under the STDP pairing protocol. Not only did they use the same protocol in their weight- and spike-time-dependent experiments, but they controlled spike timing in their weight-dependent experiment, allowing us to relate these two data sets. We therefor derive our weight-dependent plasticity rules from their data.

For simplicity, our analysis of weight- and spike-time-dependent plasticity assumes these two factors are independent. A learning rule of this form may be written as

$$\Delta w_{\{p,d\}} = k f_{\{p,d\}}(w) e^{-c_{\{p,d\}}\Delta t}, \tag{1}$$

where $\Delta w_{\{p,d\}}$ is the change in weight for potentiation (index p) or depression (index d), $\Delta t = t_{post} - t_{pre}$ is the difference between the times of post-synaptic (t_{post}) and pre-synaptic (t_{pre}) firing, and c parameterizes the timescale of the plasticity window. The experimental data are commonly shown in relative terms (%) whereas our formulations express absolute changes in synaptic strength.

We consider two forms of the weight dependent factor f. Bi and Poo (1998) hypothesized a log-linear rule by drawing a line through these data in the semi-logarithmic plot. This hypothesis yields

$$f_{\{p,d\}}(w) = (a_{\{p,d\}} - b_{\{p,d\}} \log w) w\, \theta(w), \tag{2}$$

where $\theta(w)$ is the Heaviside function, keeping weights positive, and the parameters a and b differ for potentiation and depression. A maximum weight implicit in this rule agrees with evidence for saturable synapses (Petersen et al. 1998; O'Connor et al. 2005b). We contrast the above rule with a power rule of the form

$$f_{\{p,d\}}(w) = a_{\{p,d\}} w^{b_{\{p,d\}}}. \tag{3}$$

A power law more closely approximates the data plotted on a log scale, and, unlike the log rule, imposes no maximum weight. While synapses must surely have intrinsic limits, we include this rule for comparison with the limited case. We hereafter refer to Eq. 1 with weight-dependence determined by Eqs. 2 and 3 as the log and power rules, respectively.

The constants in Eqs. 2 and 3 were determined by first fitting the weight-dependent STDP data shown in Fig. 1b. The fitted curves for the log rule are shown as solid lines alongside the potentiation data (circles) and depression data (stars) of Bi and Poo (1998). The equivalent curves for the power rule are shown as dashed lines. The fits to the depression data are nearly indistinguishable. The fits to the potentiation data agree similarly with the data, but the intrinsic limit in the log rule generates a marked difference for large weight values.

2.1 Detailed fitting procedure

Bi and Poo (1998) controlled spike timing in their weight-dependent experiment by limiting their pre-before-post (LTP) time interval to $5 < \Delta t < 15$ ms and limiting their post-before-pre (LTD) interval to $3 < \Delta t < 30$ ms. For the weight-dependent fit, we replaced these intervals with their midpoint values ($\Delta t_p = 10$, $\Delta t_d = 17.5$). We then fit their spike-time dependent data (Fig. 1b) to determine the remaining parameter c in Eq. 1, capturing the time course of

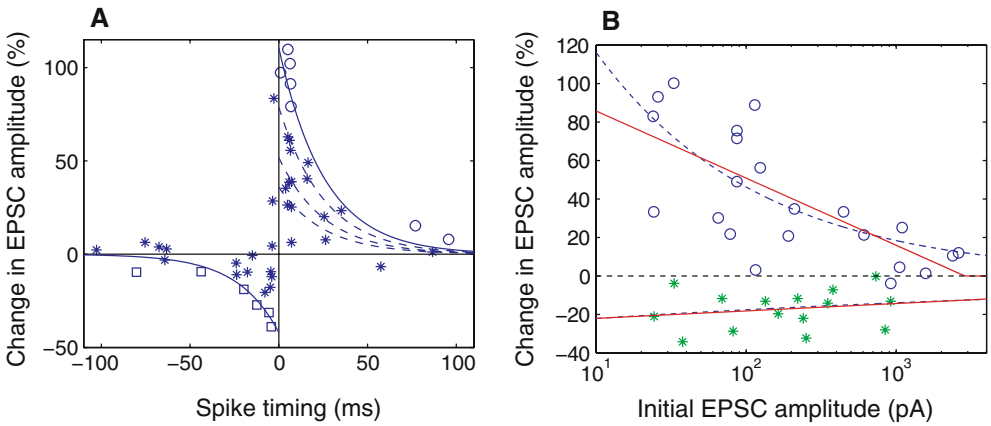

Fig. 1 **a** Fit of the power rule to Bi and Poo's (1998) spike-time dependent data for estimates of different initial weights w. *Circles* and *squares* represent $w = 30$ for potentiation and depression, respectively. Solid curves show fits to these data. *Dashed curves* for the potentiation data show fits for $w = \{70, 200, 500\}$ pA *top* to *bottom*. The log rule leads to similar fits. **b** Log and power fits to Bi and Poo's weight-dependent STDP data. A log fit imposes a maximum synaptic weight where the *upper solid line* meets the x-axis. A power fit (*dashed curve*) imposes no such maximum. These two fits are nearly indistinguishable for the LTD data

spike-time dependence for each of potentiation and depression. Because of the wide range of initial synaptic strengths in Bi and Poo's spike-time dependent experiment ($30 < w < 500$ pA) we assumed that for a given Δt, the largest relative changes in weight represent synapses with the smallest initial values. Thus, consistent with their initial weights, we assign an initial weight $w = 30$ pA to the data showing the largest STDP values, and only include these data in our time-dependent fit determining c. The resulting parameter values are $a_{\{p,d\}} = \{208, -54\}$, $b_{\{p,d\}} = \{26.4, 3.5\}$, $c_{\{p,d\}} = \{0.054, 0.042\}$ for the log rule and $a_{\{p,d\}} = \{431, -59\}$, $b_{\{p,d\}} = \{0.4, 0.1\}$, $c_{\{p,d\}} = \{0.039, 0.043\}$ for the power rule. We further assume that each of the 60 pre-before-post pairings in the experiment contributed equally to the overall synaptic change. This assumption is common in computational studies (van Rossum et al. 2000). A deviation from this linear assumption results in an altered learning rate that does not effect the means of equilibrium weight distributions. As the above parameters are deduced by fitting the percentage data, we include a factor of 100 in the learning rate to yield a fractional scale. The learning rate used in our analyses and simulations is therefore $k = 1/6{,}000$ unless otherwise stated.

Fitted curves for the power rule are shown as solid lines in Fig. 1a for our estimates of the data representing initial weights of 30 pA (open symbols). The large scatter in the figure is commonly interpreted as noise, but we interpret it according to the weight-dependence shown in Fig. 1b. For potentiation, we include dashed lines representing initial weights set to 70, 200 and 500 pA, respectively (top to bottom). The fit of the log rule leads to qualitatively similar plots.

3 Equilibrium weights for uncorrelated and time-locked pre- and post-synaptic Poisson spike trains

While the above plasticity rules are deterministic, they yield a stochastic drift of weights with stochastic spike trains. If this drift is driven by a novel correlation between pre- and post-synaptic spiking, weights will undergo considerable change from an initial random state. When weights have been driven for long periods by pre- and post-synaptic spiking with a given statistical profile, they begin to fluctuate around a mean value where the average potentiation equals the (negative) average depression. In this section, we calculate the means of these equilibrium weight distributions for the log and power rules. The drift of weights can be calculated with Fokker–Planck mean field theory (Kempter et al. 1999; Kistler and van Hemmen 2000; van Rossum et al. 2000; Rubin et al. 2001; Burkitt et al. 2004), but we are concerned with the means of equilibrium distributions and adopt the simplified methodology of Izhikevich and Desai (2003). We refer to these asymptotic values as equilibrium weights w^*.

First, we present our basic analysis for the cases of uncorrelated and time-locked pre- and post-synaptic spike trains (see Fig. 2a) where these spike trains are Poisson distributed (Bair et al. 1994) (exponential inter-spike intervals) and where only *nearest neighbour* spikes contribute to plasticity. Under nearest neighbour STDP, each pre-synaptic spike triggers LTP with the next post-synaptic spike and triggers LTD with the previous post-synaptic spike, as described by Izhikevich and Desai (2003). In Sect. 4, we show that our qualitative results do not change for partially correlated spike trains or for other spike train distributions or spike interactions.

3.1 Equilibrium weights for uncorrelated Poisson spiking

The average synaptic increase (LTP) for each pre-synaptic spike is given by

$$\langle \Delta w_p \rangle = \int_0^\infty p_p(\Delta t) \Delta w_p d\Delta t, \tag{4}$$

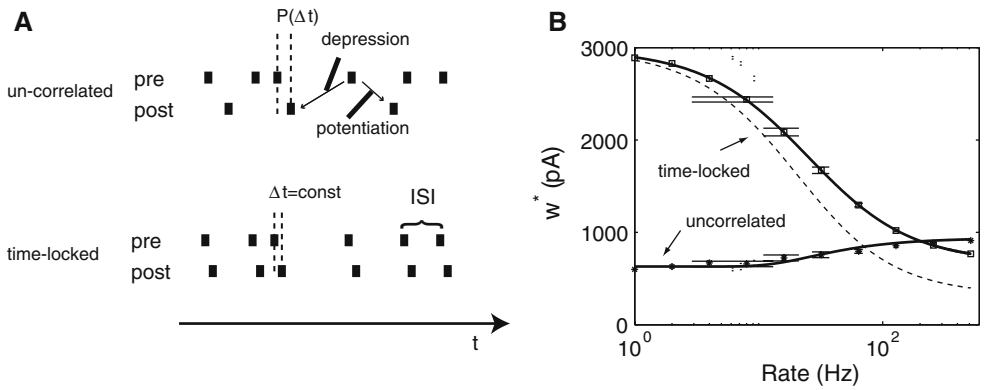

Fig. 2 **a** Illustration of uncorrelated and time-locked spike trains. **b** Equilibrium weights as a function of spike rate under the log rule for analytic (*curves*) and numeric (*symbols* with *error bars*) calculations. For time-locked spiking, the *solid* and *dashed curves* correspond to $\Delta t = 4$ and $\Delta t = 10$ ms, respectively. In numeric simulations, weights were averaged over 5,000 trials following an equilibrating 5,000 trials

where $p_p(\Delta t)$ is the probability density of a post-synaptic spike following a pre-synaptic spike with time lag Δt. Similarly, the average depression for each pre-synaptic event is given by

$$\langle \Delta w_d \rangle = \int_0^\infty p_d(\Delta t) \Delta w_d d\Delta t, \tag{5}$$

where $p_d(\Delta t)$ is the probability density of a post-synaptic spike preceding a pre-synaptic spike with time lag Δt. Thus, independent pre- and post-synaptic Poisson spike trains have an average depression and potentiation of

$$\langle \Delta w_{\{p,d\}} \rangle = f_{\{p,d\}}(w) \int_0^\infty r e^{-(c_{\{p,d\}}+r)\Delta t} d\Delta t \tag{6}$$

$$= f_{\{p,d\}}(w) \frac{r}{c_{\{p,d\}} + r}, \tag{7}$$

where r is the rate of the spike trains. We only consider the case where $r_{\text{pre}} = r_{\text{post}} = r$.

An equilibrium weight w^* is reached when the average potentiation equals the (negative) average depression. For the log rule this value is given by

$$w^* = \exp \frac{a_p(c_d + r) + a_d(c_p + r)}{b_p(c_d + r) + b_d(c_p + r)} \tag{8}$$

and for the power rule by

$$w^* = \left(-\frac{a_p}{a_d} \frac{c_d + r}{c_p + r}\right)^{\frac{1}{b_d - b_p}}. \tag{9}$$

Equilibrium weights for independent pre- and post-synaptic Poisson spike trains are shown as a function of rate in Fig. 2b for the log rule. Symbols represent the results of simulations where weights were averaged over 5,000 spike pairings following 5,000 equilibrating pairings.

3.2 Equilibrium weights for time-locked Poisson spiking

The above analysis of uncorrelated pre- and post-synaptic spikes is relevant if events represented by pre-synaptic firing are *not* associated with a post-synaptic response. In contrast, associative learning is achieved if a neuron becomes responsive to (correlated with) a pre-synaptic spike pattern. Studies have shown that STDP rules capture correlations among input spikes driving a model neuron (Kistler and van Hemmen 2000; Song et al. 2000), as synapses mediating correlated pre-synaptic activity learn to provide the strongest, fastest (Song et al. 2000) and most precisely timed (Kistler and van Hemmen 2000) inputs to the post-synaptic cell. Alternatively, plasticity may 'piggyback' other sources of activity driving pre- and post-synaptic neurons. In this section, we assume associations have been formed by one or both of these mechanisms, labelled self-organisation and associativity respectively under the terminology of Hasselmo (1995). We investigate the ongoing effect of these associations on the asymptotic strength of weights for rules grounded in Bi and Poo's data (Bi and Poo 1998).

For analytic simplicity and to illustrate the limiting case for informative spike timing, we consider the case where a post-synaptic spike is triggered with a short but fixed delay Δt following a pre-synaptic spike. We do not suggest that a single pre-synaptic spike should drive a post-synaptic neuron in this way. Rather, our pre-synaptic spikes represent the activity of one of many inputs from pre-synaptic neurons participating in an established association. We later relax this condition by varying the probability of a time-locked post-synaptic spike in Sect. 4.1.

Time-locked pre- and post-synaptic spikes result in an ongoing potentiation of weights given by

$$\langle \Delta w_p \rangle = f_p(w) e^{-c_p \Delta t} \tag{10}$$

for each pre-synaptic event. However, every pre-synaptic event can also trigger depression in conjunction with a previous (uncorrelated) post-synaptic spike (Eq. 6). An equilibrium weight w^* for time-locked pre- and post-synaptic spikes under the log rule is, therefore, given by

$$w^* = \exp \frac{a_p e^{-c_p \Delta t}(c_d + r) + a_d r}{b_p e^{-c_p \Delta t}(c_d + r) + b_d r} \tag{11}$$

and for the power rule by

$$w^* = \left(-\frac{a_p}{a_d} \frac{1}{r} e^{-c_p \Delta t} (r + c_d)\right)^{\frac{1}{b_d - b_p}}. \tag{12}$$

The rate-dependence of equilibrium weights for time-locked pre- and post-synaptic Poisson activity under the log rule is shown in Fig. 2b, where the solid and dashed lines represent analytic solutions for $\Delta t = 4$ and $\Delta t = 10$ ms, respectively. Symbols represent corresponding numeric simulations. The figure shows that equilibrium weights decrease with increasing spike rates in the strongly correlated Poisson case, but quantitatively, these values exceed biologically realistic values.

4 Equilibrium weights for alternative conditions

In the previous section, we determined equilibrium weights for the log and power rules under the specific conditions of Poisson-distributed pre- and post-synaptic spike trains, uncorrelated and time-locked pre- and post-synaptic spikes, and nearest neighbour spike interactions. Here, we show in Sect. 4.1 that partially correlated pre- and post-synaptic spike trains interpolate between the extreme cases of uncorrelated and time-locked pre- and post-synaptic spikes. We show in Sect. 4.2 that our results do not qualitatively depend on

Poisson-distributed spike trains. In Sect. 4.3, we show that our results do not depend on nearest neighbour spike interactions, in contrast to the claims of Izhikevich and Desai (2003). Finally, in Sect. 4.4, we demonstrate learning under a finite number of spike pairings, and discuss how BCM-like curves (Bienenstock et al. 1982) are generated by the log and power rules.

4.1 Equilibrium weights for partially correlated pre- and post-synaptic Poisson spiking

The cases of uncorrelated and time-locked pre- and post-synaptic spike trains define the extreme cases of possible spike train relations. Here we extend this analysis to some more realistic cases with partially correlated pre- and post-synaptic activity. We discuss two examples of correlation models, providing a biological interpretation of each. In both models, we again consider Poisson pre-synaptic spiking.

Correlation model 1: Post-synaptic spikes are generated with a probability given by constant p with a fixed time delay $\Delta t = 4$ ms. In the $(1-p)$ cases where there is no time-locked post-synaptic spike the time delay is distributed exponentially. This methodology approximates the biological case where pre-synaptic input generates a post-synaptic spike with a finite probability, but otherwise the post-synaptic neuron emits Poisson background activity. Figure 3a shows mean weights over 10,000 pairings following 10,000 equilibrating pairings under the log rule for $p = \{0, 0.2, 0.4, 0.6, 0.8, 1\}$. Low values of p lead to rate-dependent curves qualitatively similar to the perfectly time-locked case ($p = 1$) where lower means reflect the lower likelihood of correlated pre- and post-synaptic spikes.

Correlation model 2: We consider the case where correlations between pre- and post-synaptic spikes are expressed by an altered probability of a post-synaptic spike within a time Δt of a pre-synaptic event. Specifically, we consider an exponential distribution of delay times Δt, where the decay parameter is modulated for different correlations between pre- and postsynaptic spikes. The alteration of the probability density of Δt is accomplished by parameter s in Eq. 13. The mean delay Δt is set to be $(1-s)\lambda$, where $\lambda = 1/r$ is the inverse of the spike rate. For $s = 0$, this parameter yields the uncorrelated case discussed above. When s tends to 1, we expect a post-synaptic spike with a very short average time delay. The average potentiation (and similarly for depression) and the corresponding equilibrium weights are given by

$$\Delta w_p = (a_p - b_p \log w) w \int_0^\infty \frac{r}{1-s} e^{-(\frac{r}{1-s}+c_p)\Delta t} d\Delta t \quad (13)$$

$$\Leftrightarrow w^* = \exp \frac{a_p(1/((1-s)c_p+1) + a_d(1/(c_d+r))}{b_p(1/((1-s)c_p+1) + b_d(1/(c_d+r))}. \quad (14)$$

Analytic equilibrium weights for this correlation model are plotted in Fig. 3b for different values of s, where $s = 0$ is equivalent to the uncorrelated case in Fig. 2b and $s = 1$ is close to the time-locked case with $\Delta t = 1$ ms, shown with a dashed line in the figure. Both correlation models show that partial pre- and post-synaptic correlations interpolate the extreme cases discussed in Sect. 3.

4.2 Equilibrium weights for spike trains with non-Poisson statistics

We have thus far shown results for Poisson spike trains in our analysis, but similar derivations can be made for other spike distributions. While the specific values of equilibrium weights for a given rate depend on the distribution model, their qualitative dependence on rates and the correlation between pre- and post-synaptic spiking does not change. Examples from simulations for several ISI distributions are shown in Fig. 4. Figure 4a shows the cases of uncorrelated and time-locked pre- and post-synaptic spikes under the log rule. Figure 4b shows the time-locked case under the power rule. The dependence of equilibrium weights on rate is similar for these distributions, but could possibly differ for very different distributions such as those corresponding to bursting behaviour.

4.3 Equilibrium weights beyond nearest neighbour interactions

In the nearest neighbour case, we only consider the first post-synaptic spike following a pre-synaptic spike for potentiation and the first pre-synaptic spike following a post-synaptic spike for depression. While the first spike makes the greatest contribution to plasticity due to the decaying exponential term in STDP rules, it is possible that the sum of subsequent spikes has a pronounced effect on synaptic strength, as argued by Izhikevich and Desai (2003).

For Poisson spike trains, we use the following method to analytically calculate the average contribution to potentiation of the nth spike following a specific pre-synaptic spike (the method is the same for depression, where pre-synaptic spikes follow a specific post-synaptic spike). The first post-synaptic spike is expected to occur on average at $\Delta t_1 = 1/r$ for uncorrelated pre- and post-synaptic activity, and at $\Delta t_1 = \text{const}$ in the time locked case, and is weighted by $e^{-c_p \Delta t_1}$. The second spike, which we expect on average at $\Delta t_2 = \Delta t_1 + 1/r$,

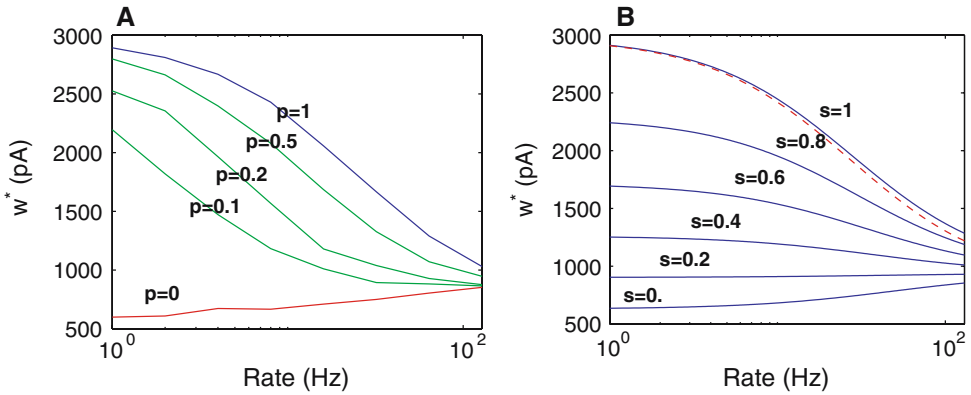

Fig. 3 **a** Correlation model with varying probability p of a time locked post-synaptic spike. Weights were averaged over 5,000 trials following 5,000 equilibrating trials. **b** Correlation model with varying exponential distribution for different correlation parameters s where $\Delta_t = r/(1-s)$. The *dashed line* shows the time looked case discussed in Sect. 3.2 with $\Delta t = 1$ ms

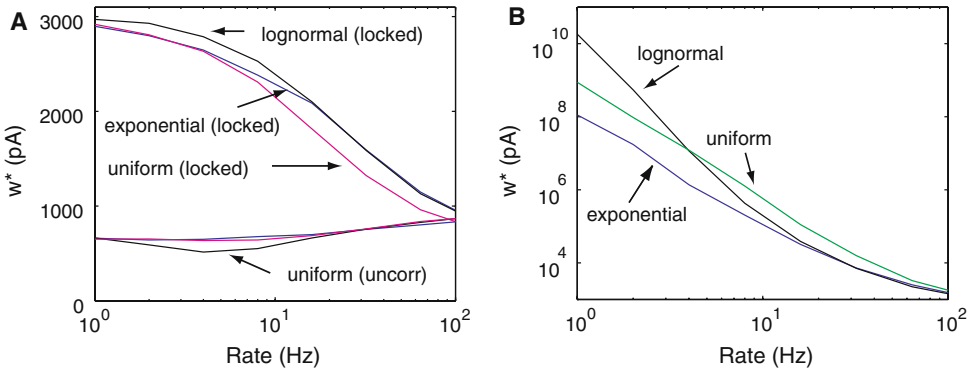

Fig. 4 Equilibrium weights as a function of rate for pre- and post-synaptic spike trains with different ISI distributions. **a** Time-locked (*top*) and uncorrelated (*bottom*) spiking with the log rule. **b** Time-locked spiking with the power rule

contributes less to potentiation because $e^{-c_p \Delta t_1} < e^{-c_p \Delta t_2}$. To calculate the average potentiation, we determine the density function of the n-th spike by convolving the density functions of all random variables in the sum. This convolution can be done analytically for Poisson spike trains by independently summing exponentially distributed random variables with equal mean λ. The resulting random variable is gamma distributed with mean $\lambda = 1/r$ and parameter n,

$$p(\Delta t_n) = \frac{(\Delta t/\lambda)^{n-1} e^{-\Delta t/\lambda}}{\lambda \Gamma(n)} \tag{15}$$

where n is the number of spikes considered. Thus, the average potentiation for uncorrelated pre- and post-synaptic spike trains is given by

$$\langle \Delta w_p \rangle = k f_{\{p,d\}}(w) \sum_{n=1}^{N} \int_0^\infty r^n (\Delta t)^{n-1} \frac{e^{-(r+c_p)\Delta t}}{\Gamma(n)} d\Delta t \tag{16}$$

and similarly for depression. Using the definition of the Gamma function,

$$\Gamma(x) = \int_0^\infty e^{-t} t^{x-1} dt, \tag{17}$$

we can evaluate this integral as

$$\langle \Delta w_p \rangle = k f_{\{p,d\}}(w) \sum_{n=1}^{N} \left(\frac{r}{r + c_p} \right)^n, \tag{18}$$

generalizing Eq. (7) to multiple spike contributions. Thus, equilibrium weights for the uncorrelated case are given for the log rule by

$$w^* = \exp \frac{a_p \sum_{n=1}^{N} (c_d + r)^n + a_d \sum_{n=1}^{N} (c_p + r)^n}{b_p \sum_{n=1}^{N} (c_d + r)^n + b_d \sum_{n=1}^{N} (c_p + r)^n}, \tag{19}$$

which reduces to Eq. (8) for $n = 1$. Furthermore, since

$$\sum_{n=1}^{\infty} x^n = \frac{1}{x-1} \quad \text{for } x < 1, \tag{20}$$

where $x = r/(r + c_{\{p,d\}})$, the all-to-all case for uncorrelated spike trains is independent of r,

$$w^*(n = \infty) = \exp \frac{a_p c_d + a_d c_p}{b_p c_d + b_d c_p}, \tag{21}$$

in agreement with Kempter et al. (1999). This value is also equivalent to the $r = 0$ limit for $n = 1$ (Eq. 8).

A similar evaluation for the time-locked case yields

$$w^* = \exp \frac{a_p \Delta P + a_d \Delta D}{b_p \Delta P + b_d \Delta D} \tag{22}$$

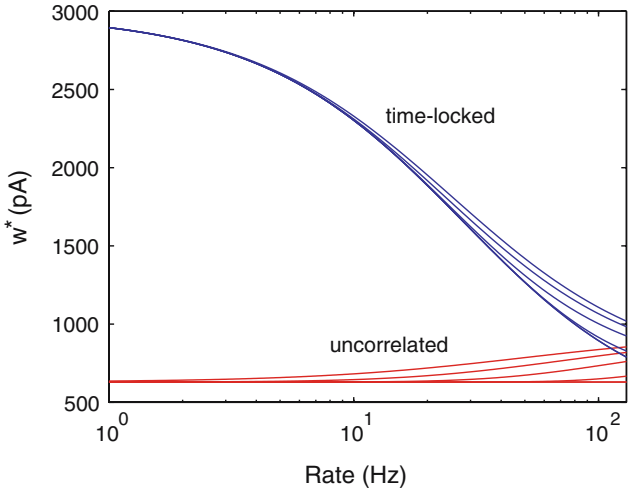

Fig. 5 Equilibrium weights under *nearest-n* interactions for time-locked and uncorrelated Poisson spike trains. In each case, *curves* correspond to values of $n = \{1, 2, 4, 10, 50, 100\}$ (*top* to *bottom*). *Curves* between $n = 50$ and $n = 100$ become indistinguishable and approximate the infinite (asymptotic) case

with

$$\Delta P = e^{-c_p \Delta t}\left(1 + \sum_{n=2}^{N} \frac{r^{n-1}(n-2)!}{(c_p + r)^{n-1}\Gamma(n-1)}\right) \tag{23}$$

and

$$\Delta D = \sum_{n=1}^{N} \frac{r^n (n-1)!}{(c_p + r)^n \Gamma(n)}. \tag{24}$$

Equilibrium values for interaction models with different n (*nearest-n* interactions) are shown in Fig. 5 for the time-locked and independent Poisson cases. These curves correspond to values of $n = \{1, 2, 4, 10, 50, 100\}$ (from top to bottom) although results between $n = 50$ and $n = 100$ become indistinguishable. As expected, an increasing number of neighbouring spikes will only influence equilibrium values at high rates due to the exponential decay of the STDP time window. Furthermore, increasing the number of neighbours n quickly converges to an asymptotic value. We reached machine precision around $n = 150$.

4.4 Convergence to equilibrium: BCM-like curves in the pre-asymptotic regime

The analysis above concerns the asymptotic regime, where equilibrium weights correspond to the infinite limit of pairings, and simulations approximate this limit with many thousands of pairings. Experiments in vitro are temporally constrained in that a plasticity-inducing stimulus is applied for a short time, after which synaptic responses are measured and compared to pre-stimulus measurements. While the duration of plasticity-inducing stimuli typically varies across protocols and the nature of experiments, the number of repetitions is typically on the order of 10–100 for STDP (Bi and Poo 1998; Froemke and Dan 2002) and pairing protocols (Petersen et al. 1998; O'Connor et al. 2005a) and 100–1000 repetitions for rate-based protocols (Dudek and Bear 1992; Kirkwood et al. 1996). We now consider the effects of the log and power rules under similar conditions.

Figure 6a shows mean percentage weight changes following $n = 100$ spike pairings where weights were initialised in the middle range of possible values (700 pA) and means were calculated over 100 trials. In this simulation, we use Poisson spike trains under the log rule with nearest neighbour spike interactions. Results for uncorrelated pre- and post-synaptic spikes correspond to the case studied by Izhikevich and Desai (2003). While we can generate BCM-like curves in this limited case of finite pairings and uncorrelated spiking, the effect is small and not found in the time-locked case. Results for time-locked spikes resemble those in the asymptotic regime (e.g., Fig. 2b) though here, percentage weight change is reduced by several orders of magnitude.

We can, however, show BCM-like curves with different spike train statistics. Figure 6b shows that BCM-like curves resembling those measured by Dudek and Bear (1992) and Kirkwood et al. (1996) are produced with time-locked, periodic pre- and post-synaptic spiking ($\Delta t = \frac{1{,}000}{2r}$ ms). Results are shown for the log rule. The solid line represents weight changes after 1,000 pairings for a synapse initialised to 700 pA. Performing the same experiment with 10,000 spike pairings results in the dashed line. The dotted line corresponds to weight changes for an infinite number of pairings (equilibrium weights). As shown in the figure, the depression valley becomes deeper and shifts to the left with an increased number of pairings, while changes in the potentiation portion of the curve are much smaller. Our investigation shows that BCM-like curves may be produced by STDP rules in the pre-asymptotic regime, but these curves depend on the precise form of pre- and post-synaptic firing. Further experiments are required to investigate this and other possible explanations for BCM-like curves, as experiments investigating BCM (Dudek and Bear 1992; Kirkwood et al. 1996) have not controlled post-synaptic firing, crucial to the BCM hypothesis.

5 Discussion and conclusions

Weight-dependent STDP rules are commonly used in modelling studies. We have presented two such rules with parameters fit to physiological data (Bi and Poo 1998) and studied their consequences in both the asymptotic and pre-asymptotic regimes. Our analysis includes the case where synapses are driven by noisy spike trains with little or no correlation between pre- and post-synaptic spikes, as done

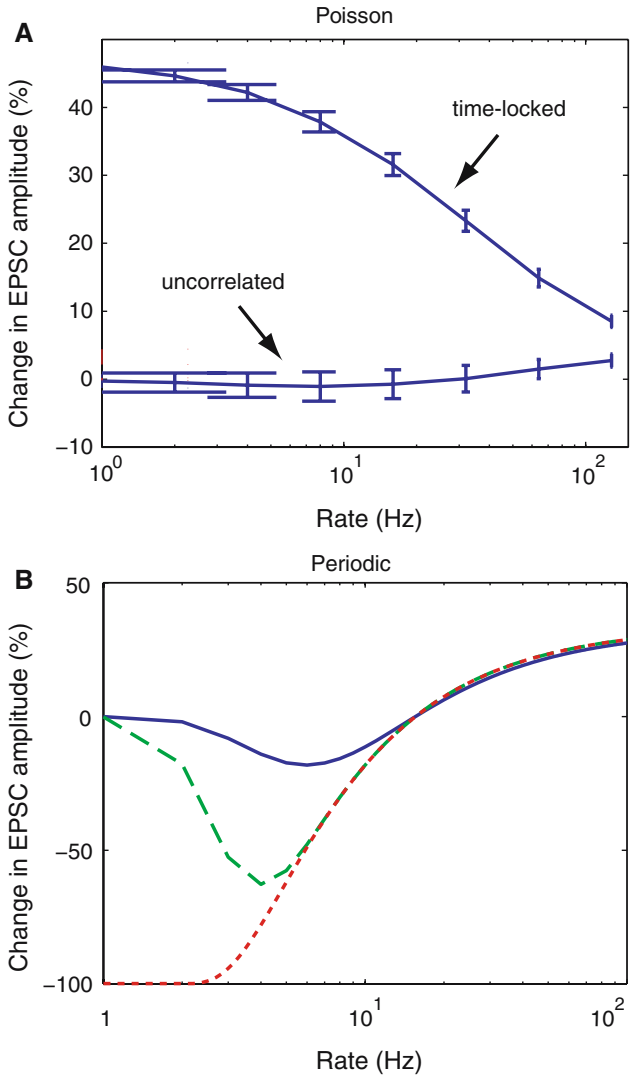

Fig. 6 Mean percentage weight change under the log rule for limited numbers of spike pairings. Weights were initialised to mid-range values (700 pA) and means were calculated over 100 trials. **a** Results for time-locked and uncorrelated Poisson spike trains for 100 pairings at rate r with nearest neighbour spike interactions. **b** Results for periodic, time-locked pre- and post-synaptic spike trains where pre- and post-synaptic spikes are 180 degrees out of phase. The *solid line* shows changes after 1,000 pairings for a synapse initialised to 700 pA. The same experiment with 10,000 spike pairings results in the *dashed line*. The *dotted curve* shows analytic equilibrium, corresponding to an infinite number of pairings

in previous studies, and also the case of highly correlated pre- and post-synaptic spike trains more closely resembling the case of associative learning. We found that 'runaway' synapses (Abbott and Nelson 2000) are still a problem for these rules, at least under parameters suggested by weight-dependent STDP data (Bi and Poo 1998).

In the pre-asymptotic regime, we show that BCM-like curves (Bienenstock et al. 1982) can be generated by weight-dependent STDP rules when low-rate activity prevents weights from reaching equilibrium values in finite time. While this effect is parameter dependent, it provides a novel instance of these curves and highlights the need for rate-based plasticity experiments that control post-synaptic spiking.

In the asymptotic regime, we find that for all spike train statistics considered, equilibrium weights for correlated spike trains decrease with increasing spike rate, a novel form of synaptic scaling. We prove this relationship for an arbitrary number of contributing spikes in the Poisson case, providing a general formula for the drift of potentiation and depression in the steady state. We further demonstrate this relationship for partially correlated Poisson spiking, showing that partial correlations interpolate between the extreme cases of time-locked and independent pre- and post-synaptic activity.

Equilibrium weights for uncorrelated spike trains increase with rate for a finite number of contributing spikes. This increase approaches 0 in the infinite limit of spike contributions, showing rate independence in this specific case, consistent with the analysis of (Kempter et al. 1999). Correlated and independent equilibrium weights converge at around 100 Hz. This effect suggests that low to intermediate rates provide a better regime for associative learning than high rates, or, stated differently, high rates may prevent weights from distinguishing between correlated and uncorrelated activity.

Under a rule imposing no maximum weight (the power rule) synapses do not reach infinite values because depression balances potentiation, but the resulting equilibrium values under both rules (with and without maxima) are too large to be useful in a biologically realistic regime. This problem has an additional, unwanted consequence. Weight-dependent STDP rules implicitly assume that a synapse can span the entire range of values in Bi and Poo's weight-dependent STDP data (Bi and Poo 1998), suggesting changes in synaptic efficacy of around 10,000%. No synapse in their experiments, however, changed in strength by more than around 100%. Many more pairings than the 60 of their protocol would be required to traverse this range, assuming their synapses could in fact be further strengthened. Alternatively, it is possible that the large variation in their initial weights (Fig. 1b) reflects varying populations of synapses. Neurons in culture often make multiple post-synaptic contacts (Debanne et al. 1996) and this possibility must be carefully addressed in future experiments on weight-dependent STDP.

Acknowledgments We thank Alan Fine and Stefan Krueger for helpful discussions. This work was supported in part by the NSERC grant RGPIN 249885-03.

References

Abbott LF, Nelson SB (2000) Synaptic plasticity: taming the beast. Nat Neurosci 3:1178–1183

Bair W, Koch C, Newsome W, Britten K (1994) power spectrum analysis of bursting cells in area mt in the behaving monkey. J Neurosci 14(5):2870–2892

Bi GQ (2002) Spatiotemporal specificity of synaptic plasticity: cellular rules and mechanisms. Biol Cybern 87:319–332

Bi GQ, Poo MM (1998) Synaptic modifications in cultured hippocampal neurons: dependence on spike timing, synaptic strength, and postsynaptic cell type. J Neurosci 18:10464–10472

Bienenstock EL, Cooper LN, Munro PW (1982) Theory for the development of neuron selectivity: orientation specificity and binocular interaction in visual cortex. J Neurosci 2(1):32–48

Bliss TVP, Lømo TJ (1973) Long-lasting potentiation of synaptic transmission in the dentate area of the anaesthetized rabbit following stimulation of the perforant path. J Physiol 232:331–356

Burkitt A, Meffin H, Grayden DB (2004) Spike-timing-dependent plasticity: the relationship to rate-based learning for models with weight dynamics determined by a stable fixed point. Neural Comput 16:885–940

Debanne D, Gahwiler BH, Thompson SM (1996) Cooperative interactions in the induction of long-term potentiation and depression of synaptic excitation between hippocampal ca3-ca1 cell pairs in vitro. Proc Natl Acad Sci USA 93:11225–11230

Debanne D, Gahwiler BH, Thompson SM (1999) Heterogeneity of synaptic plasticity at unitary ca3-ca1 and ca3-ca3 connections in rat hippocampal slice cultures. J Neurosci 19(24):10664–10671

Dudek SM, Bear MF (1992) Homosynaptic long-term depression in area ca1 of hippocampus and effects of n-methyl-d-aspartate receptor blockade. Proc Natl Acad Sci USA 89:4363–4367

Froemke RC, Dan Y (2002) Spike-timing-dependent synaptic modification induced by natural spike trains. Nature 416(6879):433–438

Froemke RC, Tsay IA, Raad M, Long JD, Dan Y (2006) Contribution of individual spikes in burst-induced long-term synaptic modification. J Neurophysiol 95:1620–1629

Gütig R, Aharonov R, Rotter S, Sompolinsky H (2003) Learning input correlations through nonlinear temporally asymmetric hebbian plasticity. J Neurosci 23:3697–3714

Hasselmo ME (1995) Neuromodulation and cortical function: modeling the physiological basis of behavior. Behav Brain Res 67:1–27

Hebb DO (1949) The organisation of behaviour. Wiley, New York

Izhikevich EM, Desai NS (2003) Relating stdp to bcm. Neural Comput 15(7):1511–1523

Kempter R, Gerstner W, van Hemmen JL (1999) Hebbian learning and spiking neurons. Phys Rev E 59(4):4498–4514

Kirkwood A, Rioult MG, Bear MF (1996) Experience-dependent modification of synaptic plasticity in visual cortex. Nature 381:526–528

Kistler WM, van Hemmen JL (2000) Modeling synaptic plasticity in conjunction with the timing of pre- and post-synaptic action potentials. Neural Comput 12:385–405

Kuhn A, Aertsen A, Rotter S (2003) Higher-order statistics of input ensembles and the response of simple model neurons. Neural Comput 15:67–101

Levy WB, Steward O (1983) Temporal contiguity requirements for long-term associative potentiation/depression in the hippocampus. Neuroscience 8:791–797

Lynch G, Dunwiddie T, Gribkoff V (1977) Heterosynaptic depression: a postsynaptic correlate of long-term potentiation. Nature 266:737–739

Markram H, Lübke J, Frotscher M, Sakmann B (1997) Regulation of synaptic efficacy by coincidence of postsynaptic aps and epsps. Science 275(5297):213–215

Montgomery JM, Pavlidis P, Madison DV (2001) Pair recordings reveal all-silent synaptic connections and the postsynaptic expression of long-term potentiation. Neuron 29:691–701

O'Connor DH, Wittenberg GM, Wang SSH (2005a) Dissection of bidirectional synaptic plasticity into saturable unidirectional processes. J Neurophysiol 94:1565–1573

O'Connor DH, Wittenberg GM, Wang SSH (2005b) Graded bidirectional synaptic plasticity is composed of switch-like unitary events. Proc Natl Acad Sci USA 102(27):9679–9684

Petersen CC, Malenka RC, Nicoll RA, Hopfield JJ (1998) All-or-none potentiation at ca3-ca1 synapses. Proc Natl Acad Sci USA 95:4732–4737

van Rossum MCW, Bi GQ, Turrigiano GG (2000) Stable hebbian learning from spike timing-dependent plasticity. J Neurosci 20(23):8812–8821

Rubin J, Lee DD, Sompolinsky H (2001) Equilibrium properties of temporally asymmetric hebbian plasticity. Phys Rev Lett 86:364

Shah NT, Yeung LC, Cooper LN, Cai Y, Shouval HZ (2006) A biophysical basis for the inter-spike interaction of spike-timing-dependent plasticity. Biol Cybern 95:113–121

Sjöström PJ, Turrigiano GG, Nelson SB (2001) Rate, timing, and cooperativity jointly determine cortical synaptic plasticity. Neuron 32:1149–1164

Song S, Miller KD, Abbott LF (2000) Competitive hebbian learning through spike-timing-dependent synaptic plasticity. Nat Neurosci 3(9):919–926

Wang HX, Gerkin RC, Nauen DW, Bi GQ (2005) Coactivation and timing-dependent integration of synaptic potentiation and depression. Nat Neurosci 8(2):187–193

frontiers in
COMPUTATIONAL NEUROSCIENCE

ORIGINAL RESEARCH ARTICLE
published: 11 February 2011
doi: 10.3389/fncom.2011.00007

Gain modulation by an urgency signal controls the speed–accuracy trade-off in a network model of a cortical decision circuit

Dominic Standage[1]*, Hongzhi You[2], Da-Hui Wang[2] and Michael C. Dorris[1]

[1] *Canadian Institutes of Health Research Group in Sensory-Motor Integration, Department of Physiology, Queen's University, Kingston, ON, Canada*
[2] *Department of Systems Science, Beijing Normal University, Beijing, China*

Edited by:
Ken Miller, Columbia University, USA

Reviewed by:
Surya Ganguli, University of California, USA
Philip Holmes, Princeton University, USA

****Correspondence:***
Dominic Standage, Queen's University, Botterell Hall, Room 453, Kingston, ON, Canada K7L 3N6.
e-mail: standage@biomed.queensu.ca

The speed–accuracy trade-off (SAT) is ubiquitous in decision tasks. While the neural mechanisms underlying decisions are generally well characterized, the application of decision-theoretic methods to the SAT has been difficult to reconcile with experimental data suggesting that decision thresholds are inflexible. Using a network model of a cortical decision circuit, we demonstrate the SAT in a manner consistent with neural and behavioral data and with mathematical models that optimize speed and accuracy with respect to one another. In simulations of a reaction time task, we modulate the gain of the network with a signal encoding the urgency to respond. As the urgency signal builds up, the network progresses through a series of processing stages supporting noise filtering, integration of evidence, amplification of integrated evidence, and choice selection. Analysis of the network's dynamics formally characterizes this progression. Slower buildup of urgency increases accuracy by slowing down the progression. Faster buildup has the opposite effect. Because the network always progresses through the same stages, decision-selective firing rates are stereotyped at decision time.

Keywords: decision making, speed–accuracy trade-off, gain modulation, urgency, neural model, recurrent network

1 INTRODUCTION

Subjects in decision making experiments trade speed and accuracy at will (van Veen et al., 2008). Under otherwise identical conditions, they make faster, less accurate decisions when motivated to favor speed, and make slower, more accurate decisions when motivated to favor accuracy. The speed–accuracy trade-off (SAT) is ubiquitous across decision making paradigms, but while the neural mechanisms underlying decisions are generally well characterized (Gold and Shadlen, 2001; Schall, 2001), the neural basis of the SAT is an open question (Gold and Shadlen, 2002).

Experimental and theoretical work indicates that decisions result from mutual inhibition between neural populations selective for each option of a decision (see Gold and Shadlen, 2007), where intrinsic (recurrent) synapses support the integration of evidence over time (Usher and McClelland, 2001; Wang, 2002). Mutual inhibition ensures that the representation of evidence accumulating in each population comes at the expense of evidence accumulating in the other(s), implementing a subtractive operation (see Smith and Ratcliff, 2004; Bogacz, 2007). This neural framework instantiates a class of algorithms frequently referred to as the drift diffusion model (DDM), known to yield the fastest decisions for a given level of accuracy and the most accurate decisions for a given decision time (see Bogacz et al., 2006). Speed and accuracy can be traded in the DDM by adjusting the level of evidence required for a decision (the decision threshold; Gold and Shadlen, 2002). Empirical studies, however, indicate that decision-correlated neural activity reaches a fixed threshold at decision time (Hanes and Schall, 1996; Roitman and Shadlen, 2002; Churchland et al., 2008). How, then, can the SAT be accomplished by neural populations with a fixed decision threshold?

A convergence of evidence offers an answer. In neuronal networks with extensive intrinsic connectivity, integration times are determined by network dynamics (Usher and McClelland, 2001; Wang, 2002, 2008; Wong and Wang, 2006). Control of these dynamics is therefore a potential means of trading speed and accuracy. Gain modulation offers a means of control, where the magnitude of the neural response to sensory evidence changes as a function of a second input signal (Salinas and Thier, 2000; Salinas and Sejnowski, 2001). We propose that the neural encoding of elapsed time (Leon and Shadlen, 2003; Janssen and Shadlen, 2005; Genovesio et al., 2006; Mita et al., 2009) provides this second input.

We model a decision circuit in the lateral intraparietal area (LIP) of posterior parietal cortex with a recurrent network model. We choose LIP because this area is extensively correlated with decision making (Roitman and Shadlen, 2002; Huk and Shadlen, 2005; Thomas and Pare, 2007; Churchland et al., 2008), gain modulation (Andersen and Mountcastle, 1983; Andersen et al., 1985), and the encoding of temporal intervals (Leon and Shadlen, 2003; Janssen and Shadlen, 2005). In simulations of a decision task, the responsiveness of the network is modulated by an increasing function of time, referred to as the buildup of urgency (Churchland et al., 2008; Cisek et al., 2009). Across all task conditions, network activation reaches a fixed threshold at decision time, consistent with neural data (Roitman and Shadlen, 2002; Huk and Shadlen, 2005; Churchland et al., 2008). Our results are explained by network dynamics. As urgency builds up, the network progresses through a series of processing stages supporting noise filtering, integration of evidence, amplification of integrated evidence, and choice selection. The rate of urgency buildup controls the rate of this progression and consequently the SAT.

2 MATERIALS AND METHODS

A cortical decision circuit was simulated with a network from a class of models widely used in population and firing rate simulations of cortical circuits (Wilson and Cowan, 1973; Pouget et al., 2000; Douglas and Martin, 2007), including feature maps in V1 (Ben-Yishai et al., 1995), posterior parietal cortex (Salinas and Abbott, 1996; Standage et al., 2005), frontoparietal cortex (Cisek, 2006), and dorsolateral prefrontal cortex (Camperi and Wang, 1998). The model assumes a columnar organization, where intercolumnar interactions are characterized by a smooth transition from net excitation between adjacent columns to net inhibition between distal columns, furnishing a continuum of overlapping on-center, off-surround population codes (see **Figure 1**).

The model is constrained by signature characteristics of neural and behavioral data from visuospatial decision making experiments. The neural data we consider were recorded in LIP, but similar activity is seen in other decision-correlated cortical areas, e.g., the frontal eye fields (see Schall, 2002). These characteristics are (1) decision-correlated neural activity showing an initial "featureless" response (equal magnitude regardless of feature value) followed by a decline in the rate of activity, competitive interactions, and a stereotyped excursion of the "winning" representation (e.g., Dorris and Glimcher, 2004; Sugrue et al., 2004; Ipata et al., 2006; Thomas and Pare, 2007; Churchland et al., 2008); (2) a fixed level of decision-selective activity at the time of the decision (e.g., Roitman and Shadlen, 2002; Churchland et al., 2008); and (3) psychometric and chronometric curves, where accuracy and decision time decrease and increase respectively as a function of task difficulty (see Section 3.1 and **Figure 3**) and decision times are in the hundreds of milliseconds range (e.g., Roitman and Shadlen, 2002; Palmer et al., 2005; Churchland et al., 2008; Shen et al., 2010). In the context of cortical processing, the first of these characteristics corresponds to a transition from feedforward dominance to feedback dominance, hypothesized to be a fundamental principle of local-circuit cortical processing (see Douglas and Martin, 2007). As we will see, the rate of this transition controls the SAT in our model. The second characteristic provides the motivation for our study, described above. The third characteristic is implicit in the SAT, on the relevant timescale for perceptual decisions.

We simulated a two-choice visual discrimination task by providing two noisy inputs to the model for 1000 ms. The task was to distinguish the stronger input (the target) from the weaker input (the distractor). While the spatial and temporal profiles of the inputs were constrained by the above data, the task clearly generalizes to other decision tasks, just as the model generalizes to other cortical regions. The neural coding of elapsed time (urgency) was simulated with a piecewise linear function (**Figure 2C**), where the slope of the function was assumed to reflect subjects' learned estimate of the time available to respond (see Durstewitz, 2004). The activation of each column was simulated with sigmoid function of its input. Gain modulation was implemented by scaling the slope of the sigmoid by the urgency signal during a given trial (Equation 2). As shown in Sections 3.4, 3.5, and 3.6, this approach permits an analysis of the gain-modulated network in trials *without* gain modulation, where urgency is omitted and the slope of the sigmoid can be set to any value spanned by the scaled slope under gain modulation.

We ran 1000 trials across a range of task difficulties and rates of buildup of urgency (Section 2.3). Task difficulty was controlled by the mean similarity of the input signals, ranging from highly distinguishable (90% similar) to indistinguishable (100% similar) on average (Equation 4). Ideal observer analysis of a population of target and distractor-selective columns was used to determine the timing and accuracy of target discrimination on each trial (Section 2.4).

2.1 THE MODEL

The network is a fully connected recurrent rate model with $N = 100$ nodes, each representing a spatially clustered population of neurons with similar response characteristics (effectively, a cortical column). The firing rate of each population represents the proportion of its neurons emitting a spike at any moment in time (Wilson and Cowan, 1972; Gerstner, 2000). The state of each node $i = 1{:}N$ (column) is described by

$$\tau_v \frac{dv_i(t)}{dt} = -v_i(t) + \sum_j W_{ij} r\left(v_j(t)\right) + h_i(t) + s_i(t), \qquad (1)$$

where the phenomenological state variable v is interpreted as the average membrane potential of each neuron in the column (Amari, 1977; Cremers and Herz, 2002), $\tau_v = 20$ ms is the average membrane

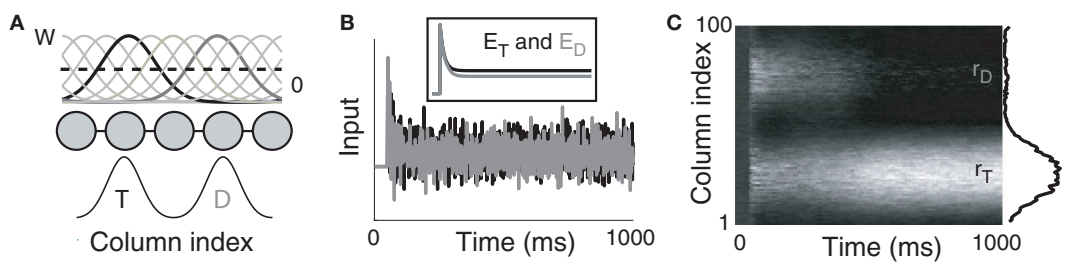

FIGURE 1 | (A) Fully recurrent network simulating 100 cortical columns. Intercolumnar interactions are scaled by down-shifted Gaussian weights W, providing local excitation (support), and distal inhibition (competition) between columns. Gaussian response fields mediate target (T) and distractor (D) input signals. **(B)** Noisy inputs at the response field centers of the target- (black) and distractor-selective (gray) populations. Inset depicts the mean input. **(C)** Surface plot of network activity during the decision task. r_T and r_D refer to firing rates of the target- and distractor-selective populations. Lighter shades correspond to higher-rate activity. The state of the network at the end of the trial is shown on the right side of the figure.

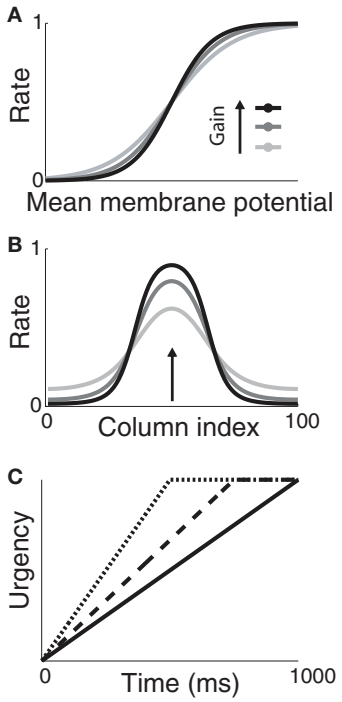

FIGURE 2 | (A) Sigmoid gain function with different values of the slope parameter β. Lighter shades of gray correspond to smaller values of β. **(B)** Network response (without gain modulation) to a single stimulus for each value of β in **(A)** above. Curves show network activation at the end of the trial. The simulation was identical to the decision task, but noise was omitted for clarity and only one stimulus was used, centered on column 50 (indicated by the arrow). **(C)** Urgency signal $U(t)$ building up over 1000 ms (solid), 750 ms (dashed), and 500 ms (dotted). Under gain modulation, β was scaled by $U(t)$ during each trial (see Equation 2, Section 2), akin to a transition from light gray to black in **(A,B)** with increasing urgency.

time constant, W governs interactions between columns indexed by $j = 1{:}N$, s is selective input, described in Section 2.2, and h is normally distributed random noise with mean $\mu_h = -10$ and SD $|\mu_h|$, determining the rate to which the network relaxes without selective input, i.e., the resting state (Amari, 1977; Doubrovinski and Herrman, 2009).

The population rate r of each node is related to the state variable v by a sigmoid gain function

$$r(v(t)) = 1/\left(1 + e^{-(1+U(t))\beta v(t)}\right) \tag{2}$$

where β determines the slope of the function, scaled by urgency signal $U(t)$ as it builds up on each trial. This scaling causes a pivot of the sigmoid around its axis (**Figure 2A**), but does not shift it to the left or right (Chance et al., 2002). The effect of the scaling on network activation is shown in **Figure 2B**. In trials with gain modulation, $\beta = 0.0275$. In trials without gain modulation (see Section 3.1), $U = 0$ and we refer to the slope parameter of the sigmoid as $\hat{\beta}$, corresponding to $(1 + U(t))\cdot\beta$ at any time t under gain modulation.

The intercolumnar interaction structure W is a Gaussian function of the spatial distance between columns arranged in a ring, where excitation-dependent inhibition is provided by subtracting a constant C from this shift-invariant weight matrix (Amari, 1977; Trappenberg and Standage, 2005), depicted in **Figure 1A**. The strength of interaction between any two columns i and j is thus given by

$$W_{i,j} = \Delta x \cdot \gamma_w \cdot \left(e^{-d^2/2\sigma^2} - C\right) \tag{3}$$

where $d = min(|i - j|\Delta x, 2\pi - |i - j|\Delta x)$ defines distance in the ring, $\Delta x = 2\pi/N$ is a scale factor, and $\gamma_w = 100$ determines the strength of intrinsic (recurrent) activity. Constants $\sigma = 0.75$ mm and $C = 0.5$ support population codes consistent with tuning curves in visual cortex (Mountcastle, 1997; Sompolinsky and Shapley, 1997).

2.2 SIMULATED TWO-CHOICE DECISION TASK

To simulate a reaction time version of a two-choice visual discrimination task, Gaussian response fields (RF) were defined for all columns i by $RF_i = e^{-d^2/2\sigma^2}$, where d and σ are given above for the intercolumnar interaction structure W. Each column i received selective input $s_i = s_i^t + s_i^d$ for time $T = 1$ s (the stimulus interval). Columns 25 (the target column) and 75 (the distractor column) were maximally responsive to s_i^t and s_i^d respectively, i.e., the RF centers of the selective inputs were 180° apart in the ring network. Spike response adaptation in upstream visually responsive neurons was modeled by a step-and-decay function (Trappenberg et al., 2001; Wong et al., 2007)

$$\mu(t) = \begin{cases} \left(\gamma_s - \gamma_\mu \gamma_s / \mu_{div}\right) e^{-(t - t_{vrd})/\tau_\mu} + \gamma_\mu \gamma_s / \mu_{div} & \text{for } t > t_{vrd} \\ 0 & \text{for } t \le t_{vrd} \end{cases} \tag{4}$$

where $\gamma_s = 75$ determines the initial strength of input at the target and distractor columns, $\mu_{div} = 3$ determines the asymptotic input strength, $\tau_\mu = 25$ ms determines the rate of input decay, and $t_{vrd} = 50$ ms is a visual response delay (Thomas and Pare, 2007). Constant γ_μ was set to 1 for the target and to γ_{ext} for the distractor, where $0.9 \le \gamma_{ext} \le 1$ determined target-distractor similarity. The strength of s_i^t and s_i^d respectively was scaled by RF_i at each column according to its proximity to the target and distractor columns. In noisy simulations, Gaussian noise with mean and SD μ was added to s_i^t and s_i^d (Salinas and Abbott, 1996). Our use of the same value of σ for the (extrinsic) RFs and the (intrinsic) lateral interaction structure W is consistent with the feedforward multiplication of accumulators by Gaussian input signals in the multiple-choice decision task of McMillen and Behseta (2010), shown by these authors to be required for asymptotically optimal hypothesis testing. Simulations were run with Euler integration and timestep $\Delta t = 1$ ms. A 200-ms equilibration period was used. Mean input to the target and distractor columns is shown in **Figure 1B**.

2.3 GAIN MODULATION BY THE URGENCY SIGNAL

The urgency signal was simulated with a piecewise linear function

$$U(t) = \begin{cases} U_{max}/\tau_u \cdot t & \text{for } t \le \tau_u \\ U_{max} & \text{for } t > \tau_u \end{cases} \tag{5}$$

where $U_{max} = 0.5$ and $\tau_{\mu} \in \{500, 750, 1000\}$ ms determines time over which the signal increases toward U_{max}, depicted in **Figure 2C**. Gain modulation was implemented by multiplying the slope parameter $\beta = 0.0275$ of the columnar gain function by $1 + U(t$; Equation 2 above).

2.4 DETERMINING THE TIMING AND ACCURACY OF DISCRIMINATION

Signal detection theory (Green and Swets, 1966) was used to quantify the degree to which an ideal observer of network activation could discriminate the target from the distractor, estimating the separation of the distributions of target and distractor-selective rates at successive 1 ms intervals. Signal detection theory is commonly applied to electrophysiological recordings under conditions in which a target stimulus is inside and (on separate trials) outside a neuron's response field, averaged over all trials (Thompson et al., 1996; Thomas and Pare, 2007). Because we can observe all the activity in the model, we applied this method to a population of target and distractor-selective columns on each trial. Each population $p = 25$ included the target and distractor columns plus the adjacent $12 \approx \sigma/2\pi N$ columns on each side of these response field centers. Receiver operating characteristic curves (ROC) were calculated from the mean rates of these populations, determining mean discrimination for each level of task difficulty and urgency signal $U(t)$. The area under the ROC (AUROC) quantifies the separation of the distributions of target and distractor activation (see Thompson et al., 1996). The probability of discrimination was quantified by a least squares fit of the AUROCs to a cumulative Weibull function

$$w(t) = c - (c - d) \cdot e^{-(t/a)^b} \quad (6)$$

where t is the time after stimulus onset, and a, b, c, and d are fitted parameters: a is the time at which the function reaches 63% of its maximum, b is the slope (shape parameter), and c and d are the upper and lower limits of the function respectively. Parameter c quantifies discrimination magnitude and is typically close to 1 (separate distributions of target and distractor activation at the end of a trial), whereas d is typically close to 0.5 (overlapping distributions at the beginning of a trial, see **Figures 4B,C**). Because either target or distractor activation could dominate the network on any given trial (correct and error trials respectively), the AUROCs could be fit with increasing or decreasing Weibull functions w. On error trials (decreasing function), a in Equation 6 refers to the time at which w reached 63% of $1 - \min(w)$, and c and d are the lower and upper limits respectively. The time at which w reached 0.75 was considered the discrimination time (Thompson et al., 1996; 0.25 on error trials). The resulting decision times were averaged over all trials to determine the speed of decision making for each task difficulty and urgency $U(t)$. Trials on which w reached neither 0.75 nor 0.25 were considered "no decision" trials.

3 RESULTS

We begin the Section 3 by showing that gain modulation of the network by a growing urgency signal produces the SAT (Section 3.1), where decision-selective activation at decision time is approximately constant across all task conditions, referred to as reaching a fixed threshold (Section 3.2). We subsequently explain these results in terms of the network's dynamics. Before doing so, it is useful to define some terminology. We define the decision variable as the difference between the activation of the target and distractor columns, and we define the time over which the noise-free model can calculate the decision variable as the network's effective time constant of integration τ_{eff} (Section 3.3). In Section 3.4, we show that as the urgency signal builds up, the network progresses through processing stages supporting a range of integration times, dominated by leakage early in each trial and by feedback inhibition later on (Usher and McClelland, 2001; Bogacz et al., 2006). The latter entails an acceleration of the decision variable, which we refer to as amplification. Note that our use of this term refers to the decision variable only, not to the network processing more generally. In Section 3.5, we show that the within-trial progression from leakage to inhibition-dominated processing allows the network to take advantage of dynamics inherently suited to different stages of the decision process, distinguishing the network from earlier models that produced the SAT with a constant within-trial signal (variable between blocks of trials). In Section 3.6, we take a dynamic systems approach, showing that our numeric explanation corresponds to a bifurcation between dynamic regimes. We analytically calculate the time constant of the linear approximate system, referred to as τ_{lin}, which undergoes the same qualitative progression as τ_{eff} in Section 3.4. Note that in simulations and analysis *without* gain modulation, we refer to the network as the fixed-gain network and to the slope parameter of its gain function as $\hat{\beta}$. Thus, for a given value of urgency $U(t)$ in the gain-modulated network, $(1 + U(t)) \cdot \beta = \hat{\beta}$ in the fixed-gain network. In Section 3.7, we show that the network earns more reward per unit time than a fixed-gain network with $\hat{\beta}$ tuned for best performance.

3.1 SPEED AND ACCURACY OF DECISIONS

For all rates of buildup of urgency U, decisions took longer and became less accurate with increasing task difficulty. The gain-modulated network thus produced typical psychometric and chronometric curves, demonstrating speed, and accuracy of decisions consistent with behavioral data (e.g., Roitman and Shadlen, 2002). Longer buildup of U resulted in slower, more accurate decisions for a given task difficulty (**Figure 3**). Under the same conditions, shorter buildup resulted in faster, less accurate decisions. The network thus produced the SAT. Of note, with lower task difficulty (90–97% similarity), the network showed another kind of SAT for all U, maintaining near-perfect accuracy by taking longer to make decisions as difficulty was increased, a feature demonstrated by earlier neural models of decision circuits (Wong and Wang, 2006).

3.2 TARGET-SELECTIVE ACTIVATION IN THE NETWORK

Consistent with neural data (Hanes and Schall, 1996; Churchland et al., 2008), target-selective activation is approximately constant at decision time across all task conditions (between 0.365 and 0.385; **Figure 4A**). It also reaches a common maximum rate across all conditions (**Figures 4B,C**), as seen in LIP during visual tasks (Roitman and Shadlen, 2002; Huk and Shadlen, 2005; Churchland et al., 2008). These two findings demonstrate a subtle but important distinction. We used ideal observer analysis to determine stimulus discrimination, so the constant level of activation at decision time

demonstrates that a downstream network could employ a fixed threshold when making decisions based on network activity (e.g., the superior colliculus reading out LIP activity). The stereotyped maximum rate of selective activation demonstrates that the network could also employ a fixed threshold to make decisions on its own, i.e., without an observer of its activity. Our results therefore demonstrate that gain modulation by the encoding of urgency can account for the SAT with a fixed threshold, whether a downstream network is reading out the modulated network or if the modulated network has the "final say" on the decision itself. Using a constant threshold to determine speed and accuracy produced similar results to those produced by ideal observer analysis (not shown).

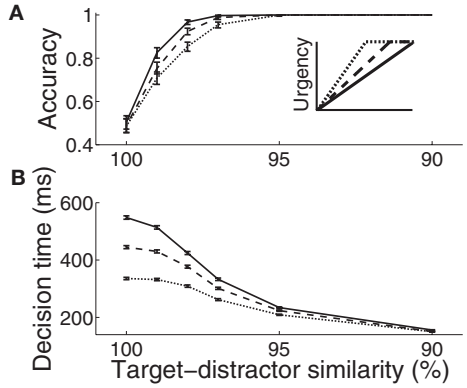

FIGURE 3 | Psychometric (A) and chronometric (B) curves show the SAT in the gain-modulated network. (A) Accuracy: the proportion of trials on which the network correctly discriminated the target. Error bars show 95% confidence intervals. **(B)** Decision time: mean time of target discrimination (see Section 2). Solid (1000 ms), dashed (750 ms), and dotted (500 ms) curves correspond to the different rates of buildup of *U*. Error bars show SE. The figure legend corresponds to **Figure 2C**.

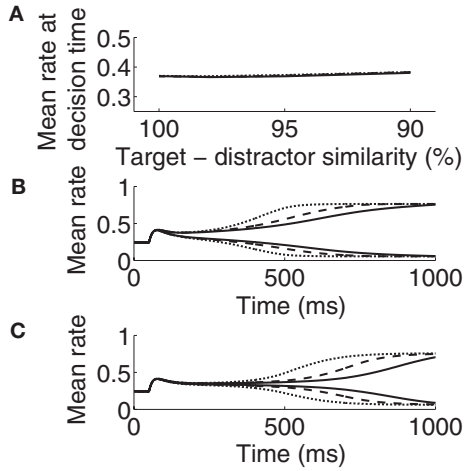

FIGURE 4 | Target-selective activation at decision time is approximately constant (A) and reaches a stereotyped maximum (B,C) across all task difficulties and rates of buildup of *U*. Solid, dashed, and dotted curves correspond to *U* building up over 500, 750, and 1000 ms respectively (see **Figure 2C**). **(A)** Target-selective rates at discrimination time on correct trials for all task difficulties and buildup of *U*, determined by ideal observer analysis (see Section 2). **(B)** Mean activation over the target and distractor populations (25 columns each, see Section 2) on correct trials for 90% target-distractor similarity. The three upper curves show target-selective rates for each *U*. The three lower curves show distractor-selective rates. **(C)** Same as in B, but for 99% target-distractor similarity.

3.3 THE EFFECTIVE TIME CONSTANT OF INTEGRATION OF THE NETWORK

The time over which a recurrent network can accumulate evidence (its effective time constant of integration τ_{eff}) can be controlled by parameters determining the strength of network dynamics (Wang, 2002; Wong and Wang, 2006). Above and below an optimal regime, τ_{eff} is progressively shortened (Wang, 2008), dominated by amplification and leakage of accumulated evidence respectively (Usher and McClelland, 2001). Larger values of τ_{eff} favor accuracy because the network can accumulate evidence for longer. Smaller values favor speed. The ability of the network to trade speed and accuracy as a function of urgency can thus be understood by considering the effect of urgency on its integration time.

We approximated τ_{eff} under gain modulation by running a noise-free trial for each *U* and task difficulty. In each of these trials, we integrated the difference between the firing rates at the target and distractor columns, where τ_{eff} was the time at which this difference (the decision variable) stopped growing (precision 10^{-6}). Longer buildup of *U* yielded longer integration times (**Figure 5A**). Target-selective rates reached a stereotyped maximum (~0.85) at τ_{eff} for all *U* and task difficulties. These results are not surprising after the results shown in **Figures 3 and 4**, but they demonstrate an important principle: slower (faster) buildup of *U* facilitated longer (shorter) accumulation of evidence under gain modulation, precisely the requirement for the DDM to trade speed and accuracy. We build on this principle below.

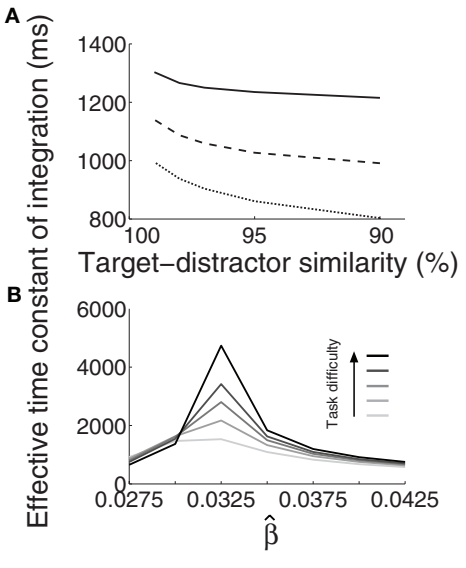

FIGURE 5 | The effective time constant of integration τ_{eff} of the network. **(A)** Solid, dashed, and dotted curves show τ_{eff} for urgency buildup over 1000, 750, and 500 ms respectively. Slower buildup yields longer τ_{eff}. **(B)** For all distinguishable tasks ($\gamma_{ext} < 1$) in the fixed-gain network (no gain modulation), τ_{eff} increases with $\hat{\beta}$ for $0 < \hat{\beta} < 0.0325$, and decreases for $\hat{\beta} < 0.0325$. Shades of gray show that this effect is more pronounced with increasing task difficulty, where lighter shades correspond to easier tasks.

3.4 URGENCY CONTROLS THE SPEED OF TRANSITIONS THROUGH PROCESSING STAGES WITH DIFFERENT EFFECTIVE TIME CONSTANTS

The above calculation of the network's effective time constant τ_{eff} for each urgency condition explains why the model produces the SAT: slower buildup of U furnishes a longer time constant. But it does not explain how. The mechanism by which gain modulation controls integration time can be understood by measuring τ_{eff} in the network *without* gain modulation (the fixed-gain network) for different values of the slope parameter $\hat{\beta}$. Here, the values of τ_{eff} can be thought of as successive snapshots of the network's effective time constant under gain modulation. Consistent with earlier analysis (Wang, 2008), τ_{eff} decreased as $\hat{\beta}$ deviated from the value supporting the longest τ_{eff} (**Figure 5B**), that is, above and below this optimal value, the decision variable was increasingly dominated by amplification and leakage respectively.

Under gain modulation, the network progresses through all these processing stages on each trial. As such, the decision variable is dominated by leakage early in the trial when urgency is low and is amplified later in the trial when urgency is high (see **Figure 6B**). τ_{eff} is thus progressively lengthened over the early part of the trial and contracted later on, terminating the decision process. This progression corresponds to a transition from left to right in **Figure 5B**. In effect, slower buildup of urgency allows the network to spend more time in processing stages with a longer time constant.

Note that our method of calculating τ_{eff} is conservative. For example, time constants are often taken at some percentage of the completion of a process, such as half-life. With and without gain modulation (**Figures 5A,B** respectively), the computed values of τ_{eff} are consistent with earlier approximations of cortical network time constants of up to several seconds (Wang, 2002). This would remain the case if τ_{eff} was taken at half rise time. Note also that this theoretical construct is not the same thing as decision time, i.e., the decision variable is saturating for much of τ_{eff} and a downstream network could read out the decision before saturation.

3.5 A PROGRESSION FROM LEAKAGE TO AMPLIFICATION OF THE DECISION VARIABLE

The progression from leakage to amplification of the decision variable with the buildup of urgency can be further understood by observing the activity in the fixed-gain network during the decision task for different values of $\hat{\beta}$. Mean activation over the target and distractor populations on a noise-free trial is shown for one task difficulty (97% similarity) in **Figure 6**. With low gain, the network distinguishes one signal from the other, but cannot accumulate much of the difference between the signals as the trial progresses (**Figure 6B**, lightest gray curves). As such, the network is capable of functioning as a noise filter, recognizing a difference between input signals, but leakage and inhibition are soon balanced (Usher and McClelland, 2001). With increased gain, the network integrates the difference between signals over the full trial, approximating the DDM, as evidenced by the near-linear increase of the decision variable (medium gray). With a further increase in gain, the network amplifies an integrated difference between inputs (dark gray). With high gain, the network quickly amplifies a small difference, demonstrating dynamics suitable for categorical choice (black). The precise correspondence between the slope parameter $\hat{\beta}$ of the gain function and each of these stages depends on the mean difference between signals, but other task difficulties yield similar curves.

Whereas the fixed-gain network implements a single regime for each value of $\hat{\beta}$, the gain-modulated network transitions through these regimes on each trial, where the rate of transition is determined by the timecourse of the urgency signal U. Thus, with gain modulation, the network smoothly progresses through a series of processing stages implementing noise filtering, difference integration, difference amplification, and selection. As such, the network begins each trial conservatively (dominated by leakage), but becomes less so as information is accumulated. The slower the buildup of U, the longer the network spends in more conservative stages, enabling higher accuracy at the expense of speed. This progression is depicted by the vertical arrow in **Figure 6B**. The outcome of the different rates of progression can be seen in the mean target and distractor-selective activation under gain modulation shown in **Figures 4A,B**, where activation diverges more slowly with slower buildup of U. **Figure 3** shows the resulting SAT.

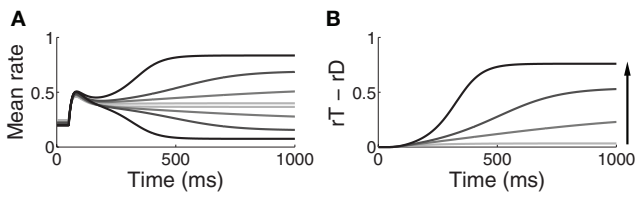

FIGURE 6 | (A) Mean activation over the target- and distractor-selective populations (25 columns each, see Section 2) on a noise-free trial for 97% target-distractor similarity in the fixed-gain network for different values of $\hat{\beta}$. Light gray, medium gray, dark gray, and black curves correspond to $\hat{\beta} = 0.0275$, $\hat{\beta} = 0.0325$, and $\hat{\beta} = 0.04$ respectively. The four upper curves show target activation. The four lower curves show distractor activation. **(B)** The difference between the target and distractor activation shown in A. The vertical arrow depicts the transition through processing stages corresponding to each value of $(1 + U(t))\cdot\beta$ under gain modulation.

3.6 NON-LINEAR DYNAMIC ANALYSIS OF THE MODEL

The above simulations demonstrate the SAT with a fixed neural threshold and provide an intuitive picture of network dynamics with growing urgency. In this section, we take a non-linear dynamics approach to formally characterize this picture.

3.6.1 Two regimes for decision making

From a dynamic systems point of view, the accumulation of evidence in the network is the evolution of a dynamic system from an initial state to an attractor corresponding to the target or the distractor. The evolution is determined by the structure of the steady states of the system (Strogatz, 2001). In our model, the slope parameter β, urgency signal U, and the target-distractor similarity γ_{ext} determine the steady states of the system defined by Equation 1. By setting the right hand side of Equation 1 to zero, we obtain a set of algebraic equations, the solution of which gives the steady states. Based on the steady state of the system, the decision process can be classified according to two regimes: in regime 1, the system evolves directly from the initial state to a single attractive stable steady state (see **Figure 7A**). In regime 2, the system is driven away from one unstable steady state to one of two stable steady states (see **Figure 7B**).

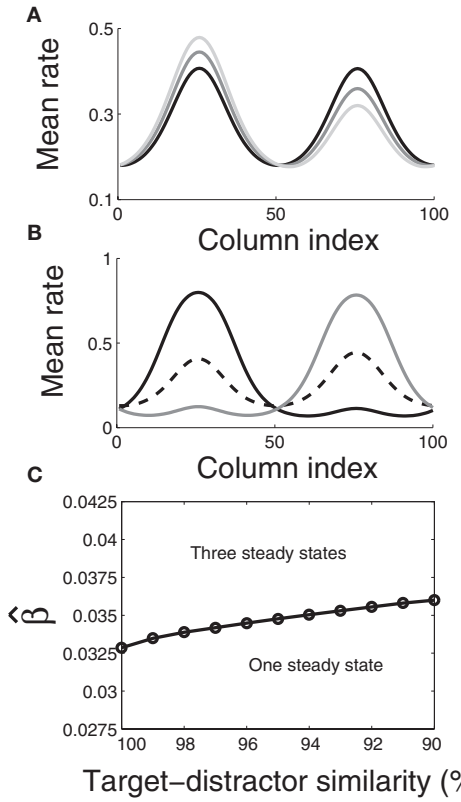

FIGURE 7 | The steady states of the system. (A) The system (Equation 1) has one steady state, which is stable. For $U = 0$ and target-distractor similarity $\gamma_{ext} \in \{1.0, 0.95, 0.9\}$, the stable steady state has two bumps, corresponding to the target and the distractor. In the indistinguishable case ($\gamma_{ext} = 1$), the stable steady state is symmetric. Otherwise, the height of the target bump is higher than the distractor bump. **(B)** The system has three steady states. Black and gray solid lines correspond to the stable steady states and the dashed line corresponds to the unstable steady state ($U = 0.4$ and $\gamma_{ext} = 0.97$). The height of the larger bump in each of the two stable steady states is almost equal and changes slightly with γ_{ext}. The difference in height of the two bumps in the unstable steady state increases with decreasing γ_{ext}. **(C)** The bifurcation diagram of the system. The parameter domain is separated into two regions: a region with one steady state and a region with three steady states.

The two regimes have several notable features. Firstly, the similarity of the target and the distractor plays a different role in each regime. In regime 1, the height of the bump related to the target is higher than the bump related to the distractor for distinguishable tasks ($\gamma_{ext} < 1$, see **Figure 7A**). The difference between the two bumps decreases with increasing target-distractor similarity γ_{ext}. In regime 2, one stable steady state has a higher bump corresponding to the target and a lower bump corresponding to the distractor; the other stable steady state has a higher bump corresponding to the distractor and a lower bump corresponding to the target. The unstable steady state has two comparable bumps, where the higher bump corresponds to the distractor and the lower bump corresponds to the target (see **Figure 7B**). The difference between the two bumps in the unstable steady state also decreases with increasing target-distractor similarity.

Secondly, by variation of the target-distractor similarity γ_{ext} and the urgency signal U (or the slope parameter β), we obtain the bifurcation diagram of the system. As shown in **Figure 7C**, there are two regions in the plane of $(1 + U)\cdot\beta$ over γ_{ext}. The system has one stable steady state in one region and three steady states in the other.

Thirdly, the evolution from the initial state to the stable steady state is determined by the structure of the steady states. In regime 1, the system evolves directly from the initial state to the single stable steady state of the target. The dynamics in the vicinity of this stable state determine the characteristics of the decision. In regime 2, the initial firing rate of the target population equals that of the distractor population (see **Figure 4**), so the initial state is in the vicinity of the two-bump unstable steady state. Therefore, the evolution from the initial state to the stable steady state is determined by the dynamics in the vicinity of the unstable steady state.

3.6.2 Regimes for accuracy and decisiveness

As described above, the decision ensues with the evolution of the system to the stable steady state. The dynamics in the vicinity of the steady state (the stable steady state in regime 1 and the unstable steady state in regime 2) thus determine task performance, such as speed, accuracy, and decisiveness (whether or not a decision is made). We have used signal detection theory to determine the decision on each trial, where the AUROC is used to estimate the separation of the distributions of target and distractor-selective activation. On any given trial, the activation of the noisy system fluctuates around the rates of the noise-free system. Therefore, the overlap of the two distributions decreases (and thus the AUROC increases) with the increase of the difference between the target and distractor-selective activation in the noise-free system. In regime 1, if the difference between the two bumps of the stable steady state is small [i.e., a low value of $(1 + U)\cdot\beta$ and a high value of γ_{ext}], the two distributions overlap too much to be discriminated and the network cannot make a decision. However, if the difference between the two bumps of the stable steady state is large enough to be discriminated, the network cannot make errors.

In regime 2, the system is driven away from the unstable steady state to one of the two stable steady states, where the difference between target and distractor-selective activation is large enough to make a decision (see $\hat{\beta} = 0.04$ in **Figure 6**). Because the system is sensitive in the vicinity of the unstable steady state, it may be driven in the wrong direction by noise, i.e., it can make errors in regime 2. Thus, the network is decisive, but makes some mistakes in regime 2, whereas it either makes correct decisions or no decision at all in regime 1.

3.6.3 The time constant of the approximate linear system

In the vicinity of the steady state, the dynamic system (Equation 1) can be linearized as

$$v(\vec{t}) = \overline{v} + \sum c_i e^{\lambda_i t} \vec{\mu}_i \tag{7}$$

where $\vec{v}$ is interpreted as the mean membrane potential, $\overline{v}$ is the steady state of the system, $\vec{\mu}_i$ is the ith eigenvector, λ_i is the ith eigenvalue, and c_i is the projection of the difference between the initial state and the steady state, defined by

$$c_i = \frac{\vec{\mu}_i{}^T(\vec{v}_0 - \overline{v})}{\vec{\mu}_i{}^T\vec{\mu}_i} \tag{8}$$

In regime 1, the eigenvalues for the stable steady state are negative, and the evolution of the system along the invariant manifold tangent to the eigenvector corresponding to the largest eigenvalue (i.e., the one closest to 0) determines how slowly the system reaches the stable steady state. Therefore, the absolute value of the reciprocal of the largest eigenvalue can be used to approximate the time it takes for the system to reach the stable steady state and is defined as the time constant. In regime 2, we consider the time it takes for the system to evolve away from the unstable steady state. The reciprocal of the largest positive eigenvalue approximates the time over which the system departs from the unstable steady state of the invariant manifold tangent to the eigenvector corresponding to the largest eigenvalue. Therefore, the absolute reciprocal of the largest eigenvalue of the stable steady state in regime 1 and the unstable steady state in regime 2 depicts the time over which the system makes a decision and is denoted τ_{lin}.

For a given target-distractor similarity γ_{ext}, the system operates in regime 1 or regime 2, depending on the value of $\hat{\beta} = (1+U)\cdot\beta$ (**Figure 7**). The time constant τ_{lin} is shown for three values of γ_{ext} in **Figure 8**, where for each curve, the left side of the discontinuity shows the time constant of the stable steady state in regime 1, and the right side shows the time constant of the unstable steady state in regime 2. These curves show the same qualitative increase and subsequent decrease with increasing of $\hat{\beta}$ shown for integration times in **Figure 5B**, where more difficult tasks have longer time constants. The slight exceptions to these characteristics occur in the vicinity of the bifurcation, where the time constant is undefined because the eigenvector is zero at the bifurcation point, but the progression through processing stages with different time constants described in Sections 3.3 and 3.5 is clear. Notably, the time constants in **Figures 5 and 8** peak at approximately the same value of $\hat{\beta}$.

3.6.4 The dynamics of decision making with growing urgency

With growing urgency, decision processing under gain modulation can be described according to the above two regimes. In the early stages of a decision, the system operates in regime 1 because the urgency signal is low. The system has only one stable steady state with activation bumps centered at the target and distractor columns. As the urgency signal grows, the target and distractor-selective activation in the steady state gradually increases and decreases respectively (see **Figures 9A–C**). This changing stable steady state is tracked by the system and consequently the target and distractor-selective activation in the network gradually increases and decreases respectively before the urgency signal exceeds the bifurcation threshold (**Figure 7C**). If the urgency signal does not cross the bifurcation threshold, the system will approach the stable steady state of the final urgency signal. If the difference between the target and distractor-selective activation is large enough, the system makes a correct decision, otherwise, it makes no decision. Once the urgency signal exceeds the bifurcation threshold, the system operates in regime 2 and the stable steady state splits into three steady states, one unstable and two stable (see **Figures 9D–F**). At the same time, the state of the system, which tracks the stable steady state in regime 1 and whose target-selective activation is stronger than the distractor-selective activation, falls into the vicinity of the unstable steady state in regime 2. Driven away from the unstable steady state, the system evolves to one of the stable steady states (corresponding to the target or the distractor) and makes a decision.

In the fixed-gain network, the decision process occurs either in regime 1 or in regime 2, depending on the slope parameter $\hat{\beta}$ and the target-distractor similarity γ_{ext}. For distinguishable tasks under gain modulation, if the urgency signal is big enough to cross the bifurcation threshold ($0.95 < \gamma_{ext} < 1$), the progression from regime 1 to regime 2 allows the network to begin regime 2 in a state closer to the target attractor than would be the case in the fixed-gain network with slope parameter $\hat{\beta}$ equal to $1+U(\bar{t})\cdot\beta$, where $\bar{t}$ is the time at which U crosses the bifurcation threshold. This advantageous position of the network state formally characterizes the progression described in Section 3.5, where early noise filtering allows late amplification of a high-quality decision variable. As described in Section 3.6.3, the progression stretches the time constant τ_{lin} as the system moves through regime 1, before contracting it in regime 2 on the way to the stable steady state of the target or the distractor. Speed and accuracy are traded because the time constant τ_{lin} and the decision variable are larger at decision time with slower buildup of U (not shown). When the decision occurs in regime 1, the decision variable is larger at decision time with faster buildup of U, but accuracy is not compromised because the network cannot make errors.

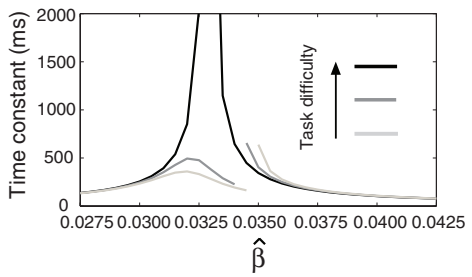

FIGURE 8 | The time constant of the steady state τ_{lin}. For each target-distractor similarity γ_{ext}, the network operates in regime 1 with low $(1 + U)\cdot\beta$ and subsequently in regime 2 with high $(1 + U)\cdot\beta$. Thus, the left side of each curve shows the time constant for the stable steady state of regime 1, and the right side shows the time constant for the unstable steady state of regime 2. For $\gamma_{ext} = 1$, the time constant increases in regime 1 and decreases in regime 2. For $\gamma_{ext} = 0.97$ and 0.95, the time constant increases and then decreases in regime 1, peaking at approximately $\hat{\beta} = 0.0325$, consistent with the simulations in **Figure 5**. The time constant decreases in regime 2 for all γ_{ext}.

3.7 OPTIMAL DECISION MAKING

The above analysis shows that the bifurcation between regime 1 and regime 2 under gain modulation puts the network in a state closer to the target attractor when it enters regime 2 than would be the case in the fixed-gain network with slope parameter $\hat{\beta}$ equal to $(1+U(\bar{t}))\cdot\beta$ at the time of the bifurcation $\bar{t}$. This analysis suggests that gain modulation by the urgency signal may produce more accurate decisions per unit time than the fixed-gain network. To investigate this possibility, we calculated the reward rate over a full block of 6000 trials (1000 trials for six values of target-distractor similarity γ_{ext}) under gain modulation for each of the above rates of buildup of U. Because the urgency signal simulates

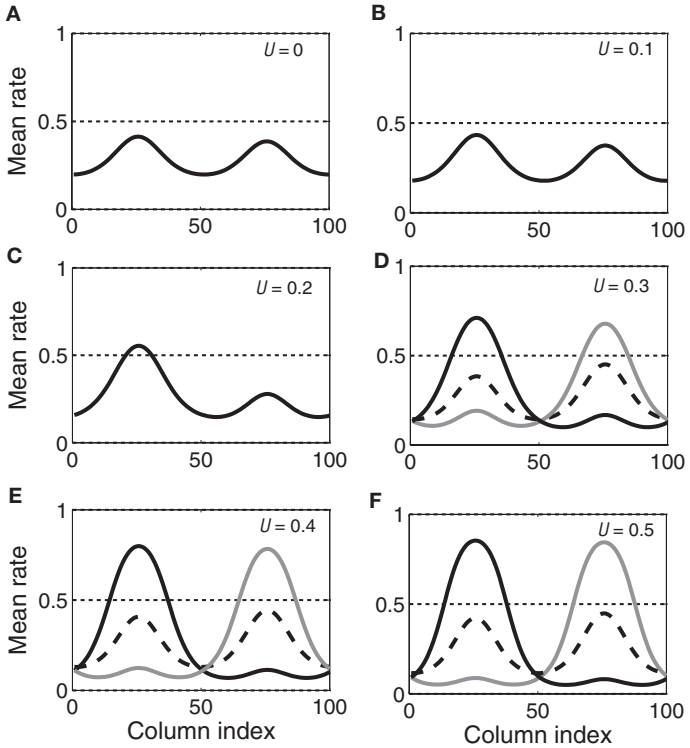

FIGURE 9 | The evolving steady states of the network with growing urgency. As urgency $U(t)$ builds up on each trial, the network undergoes a bifurcation from a regime with a single stable steady state (**A–C**, regime 1 in the text) to a regime with one unstable steady state and two stable steady states (**D–F**, regime 2 in the text). In the latter, one stable steady state corresponds to the target (solid black) and one to the distractor (gray). Target-distractor similarity in the figure was $\gamma_{ext} = 0.97$. The dotted horizontal line **(A–F)** helps to gage the size of the bumps and has no other significance.

an estimate of the time available to respond (see Durstewitz, 2004), $\tau_u = 1000$ ms corresponds to an accurate estimate of the deadline and $\tau_u < 1000$ ms corresponds to an underestimate. We also considered an overestimate of τ_u, running a full block of trials for $\tau_u = 1250$ ms, where the trial time was still 1000 ms, i.e., $U(t)$ never reaches U_{max}. We also ran a full block of trials with the fixed-gain network for a range of values of $\hat{\beta}$, including several values near the best-performing $\hat{\beta}$ to ensure we were not missing a finely tuned optimum (see **Figure 10**).

Because mean decision time on error trials was longer than on correct trials under gain modulation (see Section 4.3), we followed the reward rate definition of Eckhoff et al. (2009), where penalties on error trials were considered implicit in decision time. Reward rate was thus defined on each trial as $R = A/(DT + NDL)$, where A is accuracy (one for correct decisions and zero for errors or no decision trials), DT is decision time, and NDL is non-decision latency. NDL subsumed the post-decision motor response (≈200 ms), an interval between trials (≈1750 ms), and the visual response delay (50 ms, see Section 2). Non-decision latency was thus $2000 - 50 = 1950$ ms. As shown in **Figure 10**, reward rates were systematically higher in the gain-modulated network and were maximal when $U(t)$ peaked at the trial deadline, i.e., of the urgency signals tried, an accurate estimate of the trial length was optimal in terms of maximizing reward (**Figure 10**). These findings were qualitatively reproduced with the reward rate definition of Gold and Shadlen (2002; not shown).

This finding is instructive in several regards. Earlier work showed that a spatially non-selective signal, variable between blocks of trials, but constant within each trial, could potentially produce the SAT with a fixed threshold (Bogacz et al., 2006; Furman and Wang, 2008). This approach is equivalent to setting U to a fixed value between trials in our model and could be instantiated by goal-directed persistent activity in higher association cortical areas (see Goldman-Rakic, 1995; Wang, 2001). This mechanism is plausible, though we are unaware of any data showing the rate of persistent activity to vary systematically between trials or blocks of trials, as would be required. There is a growing body of data showing the neural encoding of elapsed time relative to learned intervals (see Durstewitz, 2004), previously correlated with decisions (Churchland et al., 2008) and proposed here to control the SAT. The analysis in Section 3.6 and the calculation of reward rate in this section show that a within-trial signal is optimal in our model, though we expect within-trial and between-trial gain modulation to play complimentary roles in decision making and cognitive function more generally (see Section 4.4).

4 DISCUSSION

Our model offers a candidate neural mechanism for the SAT. We propose that gain modulation by the encoding of urgency controls the time constant of cortical decision circuits "on the fly." The rate of buildup of urgency determines how long the circuit integrates evidence before the decision variable is amplified. Longer (shorter)

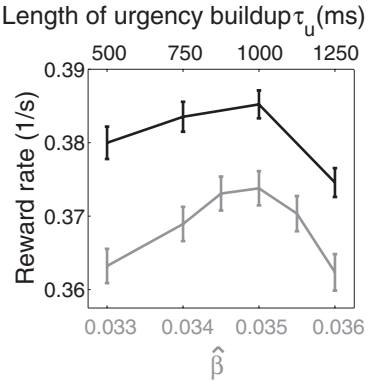

FIGURE 10 | Reward rate over a full block of trials as a function of the buildup of urgency under gain modulation (black) and the slope parameter of the gain function $\hat{\beta}$ in the fixed-gain network (gray). The time over which the urgency signal $U(t)$ builds up corresponds to an underestimate ($\tau_u \in \{500, 750\}$ ms), an accurate estimate ($\tau_u = 1000$ ms) and an overestimate ($\tau_u = 1250$ ms) of the trial deadline. Error bars show SE.

estimates of the time available to respond result in slower (faster) buildup of the signal, so the circuit spends more (less) time integrating evidence. Importantly, decision-correlated neural activation reaches a fixed level at decision time, consistent with neural data (see Schall, 2001). In effect, the encoding of urgency determines the rate of growth of the decision variable, instantiated by the well established mechanisms of gain modulation (Salinas and Thier, 2000; Salinas and Sejnowski, 2001) and the encoding of the passage of time (Durstewitz, 2004; Mauk and Buonomano, 2004; Buhusi and Meck, 2005).

4.1 A NEURAL MECHANISM FOR TIME-VARIANT DRIFT DIFFUSION WITH A FIXED THRESHOLD

Our neural model is grounded in abstract, mathematical models that have been instrumental in characterizing decision processes. Sequential sampling models are based on the premise that evidence is integrated until it reaches a threshold level (see Smith and Ratcliff, 2004). Because evidence may be incomplete or ambiguous and neural processing is noisy, temporal integration provides an average of the evidence, preventing decisions from being made on the basis of momentary fluctuations in either the evidence or processing. The longer the integration time, the better the average (see Bogacz, 2007). In two-choice tasks, integrating the difference between the evidence favoring each option implements the DDM, known to yield the fastest decisions for a given level of accuracy and the most accurate decisions for a given decision time (see Bogacz et al., 2006). The DDM thus optimizes speed and accuracy for a given threshold. The SAT can be achieved by varying the threshold, a principle suggested to be instantiated in the brain (Gold and Shadlen, 2002).

The DDM has been augmented with a time-variant mechanism similar in principle to our use of urgency (differences between the models are described below). In the model by Ditterich (2006b), the decision threshold is lowered over the course of each trial. This approach is functionally equivalent to an increasing multiplication of the evidence as the trial progresses, demonstrated to earn more reward per unit time than the standard DDM in a two-choice task with no explicit deadline (Ditterich, 2006a). The time-dependent multiplication of evidence permits the effect of urgency with a fixed threshold, so this abstract model is consistent with neural data in that regard. Although the SAT was not a focus of these studies, varying the rate of either time-dependent mechanism would effectively trade speed and accuracy.

Neural models have addressed the possible mechanisms underlying the above mathematical models, several of which have been shown to be equivalent to the DDM under biophysical constraints. In these models, the subtractive operation is implemented by mutual inhibition between neural populations selective for each option of a decision (Bogacz et al., 2006), a ubiquitous neural process that scales naturally with the number of options (Usher and McClelland, 2001). Recurrent processing allows slow integration, where network dynamics yield effective time constants much longer than those of contributing biophysical processes (e.g., the time constants of synaptic receptors; Wang, 2002). This neural framework accounts for wealth of neural and behavioral data (see Schall, 2001; Gold and Shadlen, 2007; Wang, 2008). Varying a threshold firing rate will trade speed and accuracy in these models, but, as described above, it conflicts with experimental data (see Schall, 2001).

Our model trades speed and accuracy with a fixed threshold by exploiting the time constant of recurrent networks (Sections 3.3 and 3.6.3). Previous work showed that biophysically based parameters determine an optimal processing regime (Wang, 2002; Wong and Wang, 2006), above and below which the time constant is monotonically shortened (Wang, 2008), dominated by inhibition and leakage respectively (Usher and McClelland, 2001; Bogacz et al., 2006). In these studies, networks were tuned to a single set of parameters that were chosen for best performance. This configuration was then used in a decision task. Unlike these models, our network employs a range of time constants on each trial, where speed and accuracy are traded according to the rate of progression from leakage to inhibition-dominated processing (Sections 3.4 and 3.5). The rate of progression is determined by the urgency signal. Because the network passes through the same processing stages in all cases, its activity follows the same trajectory and decisions can be made with a fixed threshold. In effect, faster (slower) buildup of urgency contracts (expands) the progression in time, but nothing else changes.

4.2 BIOLOGICAL CORRELATES OF THE MODEL

We have used a network belonging to a class of local-circuit models (Wilson and Cowan, 1973; Amari, 1977) widely used to simulate cortical processing of continuous feature values such as spatial location (Camperi and Wang, 1998; Standage et al., 2005). These models are referred to by a number of names, including dynamic neural fields (Trappenberg, 2008), line attractor networks (Furman and Wang, 2008) and basis function networks (Pouget et al., 2000). The model's foundations are based on a columnar structure where inhibition is broadly tuned and the probability of lateral excitatory synaptic contact is normally distributed (see White, 1989; Abeles, 1991; Goldman-Rakic, 1995).

We have modeled subjects' estimates of the passage of time with a piecewise linear function, where different slopes correspond to different urgency conditions (**Figure 2C**). While this first approximation is clearly simplistic, it is supported by neural data showing approximately linear ramping that reaches a common peak around the time of an anticipated event (see Durstewitz,

2004). In reaction time tasks with a deadline (Schall and Hanes, 1993; McPeek and Keller, 2004; Thomas and Pare, 2007), such activity would provide an explicit encoding of the urgency to respond. Even in reaction time tasks without a deadline, it is common to constrain the timing of reward to discourage fast reaction times (Roitman and Shadlen, 2002; Huk and Shadlen, 2005), motivating subjects to self-impose deadlines that limit the time between trials (and thus rewards). Neural correlates of temporal estimates have been described in posterior parietal cortex (Leon and Shadlen, 2003; Janssen and Shadlen, 2005), prefrontal cortex (Genovesio et al., 2006), premotor cortex (Mita et al., 2009), and the mid-brain superior colliculus (Thevarajah et al., 2009) among other structures. These data suggest that temporal coding mechanisms can be more complex than linear ramping activity, but the model is by no means limited to the linear case. For example, in the DDM with a collapsing threshold, best performance was achieved with a logistic function of time, rather than a linear function (Ditterich, 2006b). Whether and how different urgency signals affect the model is left to a follow up study.

Neural mechanisms that may underlie gain modulation include recurrent processing of spatially non-selective input (Salinas and Abbott, 1996), voltage-dependent dendritic non-linearities (Mel, 1993; Larkum et al., 2004), and changes in cellular input–output relationships caused by temporal correlations in input activity (Salinas and Sejnowski, 2001), background noise (Chance et al., 2002; Prescott and Koninck, 2003; Higgs et al., 2006), and other factors leading to variable conductance states (Destexhe et al., 2003). Our method of gain modulation was meant to abstract over such mechanisms. Note that alternative methods of gain modulation lead to similar results, including the multiplication of network activity by the urgency signal, and the urgency-dependent increase in the strength of recurrent connections (not shown).

4.3 DIFFERENCES WITH EARLIER TIME-VARIANT MODELS OF DECISION MAKING

While conceptually similar to Ditterich's (2006a) time-variant DDM, our network model differs in a crucial respect: the evolving decision variable is subject to gain modulation, not just the instantaneous evidence. Consider the DDM performing a two-choice decision task. As above, let s^t and s^d refer to noisy evidence for the target and distractor respectively. At any instant, the difference between the evidence for each option is $x(t) = s^t(t) - s^d(t)$, which is integrated over time. Let X refer to the running total (the decision variable). The time at which the absolute value $|X|$ exceeds a threshold $\theta > 0$ is the decision time. If X is positive at the decision time, the target is chosen. If X is negative, the distractor is chosen. We may therefore express the DDM as

$$\frac{dX}{dt} = s^t(t) - s^d(t); \quad |X| \le \theta. \tag{9}$$

In the time-variant DDM (Ditterich, 2006a), s^t and s^d are multiplied by an increasing temporal signal similar to the urgency signal U. Thus, Ditterich's model may be expressed as

$$\frac{dX}{dt} = U(t) \cdot \left[s^t(t) - s^d(t) \right]; \quad |X| \le \theta. \tag{10}$$

Like Equation 10, the input signals to our network model are subject to an increase in gain, but so is the recurrent processing of the decision variable. The subtractive operation is supported by recurrent inhibition. We may thus express our model as

$$\frac{dX}{dt} = \alpha \cdot U(t) \cdot X(t) + U(t) \cdot \left[s^t(t) - s^d(t) \right]; \quad |X| \le \theta, \tag{11}$$

where α is a (positive) scale factor. The practical difference between the two models is the time of arrival of the evidence subject to strong amplification. In Equation 10 (and in Ditterich's model), an increasing urgency signal gives greater weight to later evidence than earlier evidence because only the input is amplified. In Equation 11 (and in our network model), there is a transition from a heavier weighting of the input to a heavier weighting of the decision variable, similar to the transition from extrinsic to intrinsic processing hypothesized to be a fundamental principle of local-circuit cortical processing (see Douglas and Martin, 2007). The urgency signal governs the rate of this transition.

The implications of the difference between the two models can be seen in **Figure 11A** for a noisy trial with 99% target-distractor similarity, where Equations 10 and 11 were given the same inputs received by the target and distractor columns in the network, $U_{max} = 10$ (Equation 5) and $\alpha = 1/1000$. Equation 11 makes different decisions for different rates of urgency buildup. With faster buildup, the model effectively ignores later evidence (see figure caption). In contrast, Equation 10 is always dominated by its inputs. This feedforward dominance is clearly shown in **Figures 11B,C**, where the evidence for the target and the distractor was switched in the fourth and first quartiles of a noise-free trial respectively (see figure caption). An attractive feature of Equation 11 is the explosion of the decision variable (black curves in the figure), alleviating the need for fine tuning of the decision threshold, similar in principle to the subcritical bifurcation in the non-linear diffusion model by Roxin and Ledberg (2008).

While the difference between these time-variant DDMs is clear from Equations 10 and 11 and **Figure 11**, we do not further investigate the novel DDM introduced by Equation 11 in this paper. Suffice to say, we anticipate that Equations 10 and 11 will produce similar results over a block of trials with constant mean evidence (within each trial), the dominant experimental approach to date (e.g., Roitman and Shadlen, 2002; Thomas and Pare, 2007; Churchland et al., 2008). However, in trials with interference stimuli (Huk and Shadlen, 2005) or changing evidence (Cisek et al., 2009), results will differ due to the timing of amplification. It is worth noting that both models produce error trials that are longer than correct trials, but they do so for different reasons. As elegantly explained by Ditterich (2006b), error trials are longer than correct trials in his model because noise grows faster than drift rate; the lower signal-to-noise ratio later in trials leads to more errors, so error trials are longer on average. Here, error trials take longer because the system has to cross the invariant manifold of the unstable steady state, which takes more time.

Our model also bears conceptual similarities with the "urgency gating" models of Cisek et al. (2009). In their study, mathematical models were compared for their ability to explain data from decision tasks with changing evidence. Under noisy conditions, the

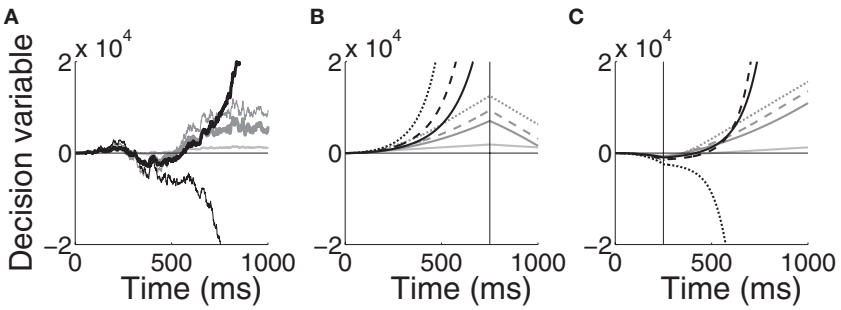

FIGURE 11 |Time-variant DDMs given by Equations 10 (dark gray, modulation of the inputs) and 11 (black, modulation of the inputs and the decision variable). (A) A noisy trial with mean target-distractor similarity 99%. The DDMs received the same inputs as the target and distractor columns in the network with urgency building up over 1000 ms (thick curves) and 500 ms (thin curves). The inputs to each model were identical, including noise. The light gray curve shows the standard DDM (Equation 9, no urgency). Parameters are given in the text. **(B)** Noise-free trial with changing evidence for target-distractor similarity 90% and urgency buildup over 1000 ms (solid), 750 ms (dashed) and 500 ms (dotted). The vertical line indicates the switching of the target and distractor stimuli over the last quarter of the trial. Step inputs were used (no decay) and the visual response delay was omitted. The light grey curve shows the standard DDM (Equation 9, no urgency). **(C)** Same as in **(B)**, but the evidence was switched during the first quarter and in Equation 11 was increased from 1/1000 to 1/750.

most successful model multiplied elapsed time by a low-pass filter of the evidence, which can be thought of as a brief spatiotemporal average. Notably, their data suggest that urgency controls the SAT. Our model provides a neural mechanism by which such control may be exerted.

4.4 FLEXIBLE MODULATION OF DECISION CIRCUITRY ON MORE THAN ONE TIMESCALE

Ultimately, the modulation of decision circuitry is likely to occur on more than one timescale. Two such timescales are captured by the mathematical models of Gold and Shadlen (2002) and Ditterich (2006b). The former specifies a decision threshold for the DDM for all trials of an experiment (or some set of decisions). The latter adjusts the decision threshold on a within-trial basis, lowering it over the course of each trial. Although our neural model uses a within-trial approach, it offers a time-variant mechanism that in principle, can flexibly implement either or both approaches. The gain-modulated network began and ended each trial in extreme regimes dominated by leakage and inhibition respectively. These rough parameters account for the SAT, but modulation of cortical processing occurs on longer timescales as well, providing a mechanism for instantiating the approach of Gold and Shadlen (2002). Trial-to-trial modulation could be implemented in our model by varying the initial strength of the network on each trial (the initial value of β) depending on previous choices and their reward outcomes (Dorris et al., 2000; Thevarajah et al., 2010). Within-trial and between-trial modulation are both potentially supported by the different timescales of dopamine signals (see Schultz, 2007). Dopamine is extensively correlated with reward (see Schultz, 2006) and can modulate gain in cortical circuitry (see Seamans and Yang, 2004). We thus envision trial-to-trial and within-trial modulation playing complementary roles in decision making.

4.5 SUMMARY AND CONCLUSIONS

Models of decision circuits have demonstrated that network dynamics determine time constants of integration (Wang, 2002, 2008; Wong and Wang, 2006) and that corresponding processing regimes are subject to modulation (Eckhoff et al., 2009). To date, however, neural models instantiating the DDM have used a single mechanism to control speed and accuracy: the difference between the decision threshold and the level of activity on which the decision variable builds (see Bogacz et al., 2006 for analysis of these models). If sufficiently variable, initial levels of activity could account for the SAT with a constant threshold. Here, we propose another, compatible mechanism. In the context of sequential sampling models, the crucial factor is integration time, control of which is not limited to the difference between initial and threshold levels of activity. In this regard, it is instructive to distinguish between the quality of the decision variable and the rate of neural activation sufficient for the decision. For example, network dynamics force decisions in our model when the target and distractor are identical on average, also shown by earlier models (Wang, 2002; Wong and Wang, 2006). This property is useful because decisions often have deadlines, but the quality of the decision variable is low in these cases.

The notion of urgency in decision making is not new (Reddi and Carpenter, 2000) and is an instance of the concept of hazard rate, or the anticipation of an upcoming event (Luce, 1986; Janssen and Shadlen, 2005). A growing body of experimental data suggests that the encoding of time is as natural a process as the encoding of space (see Durstewitz, 2004; Mauk and Buonomano, 2004; Buhusi and Meck, 2005). When faced with deadlines, either self-imposed or imposed by the environment, it appears we automatically encode the urgency to respond. At least one empirical study has quantified the representation of urgency along these lines, where neural activity was correlated with both the passage of time and subjects' decisions in a decision task, independent of the evidence (Churchland et al., 2008). Our study proposes a neural mechanism by which integration and urgency are combined: decisions are based on integrated evidence, but integration time is controlled by the representation of urgency.

ACKNOWLEDGMENTS

This work was supported by the Canadian Institutes of Health Research. Da-Hui Wang was supported by NSFC under Grant 60974075. Dominic Standage thanks Martin Paré and Thomas Trappenberg for helpful discussions.

REFERENCES

Abeles, M. (1991). *Corticonics: Neural Circuits of the Cerebral Cortex*. Cambridge: Cambridge University Press.

Amari, S. (1977). Dynamics of pattern formation in lateral-inhibition type neural fields. *Biol. Cybern.* 27, 77–87.

Andersen, R. A., Essick, G. K., and Siegel, R. M. (1985). Encoding of spatial location by posterior parietal neurons. *Science* 230, 456–458.

Andersen, R. A., and Mountcastle, V. B. (1983). The influence of the angle of gaze upon the excitability of the light-sensitive neurons of the posterior parietal cortex. *J. Neurosci.* 3, 532–548.

Ben-Yishai, R., Bar-Or, R. L., and Sompolinsky, H. (1995). Theory of orientation tuning in visual cortex. *Proc. Natl. Acad. Sci. U.S.A.* 92, 3844–3848.

Bogacz, R. (2007). Optimal decision-making theories: linking neurobiology with behaviour. *Trends Cogn. Sci.* 11, 118–125.

Bogacz, R., Brown, E., Moehlis, J., Holmes, P., and Cohen, J. D. (2006). The physics of optimal decision making: a formal analysis of models of performance in two-alternative forced-choice tasks. *Psychol. Rev.* 113, 700–765.

Buhusi, C. V., and Meck, W. H. (2005). What makes us tick? Functional and neural mechanisms of interval timing. *Nat. Rev. Neurosci.* 6, 755–765.

Camperi, M., and Wang, X.-J. (1998). A model of visuospatial working memory in prefrontal cortex: recurrent network and cellular bistability. *J. Comput. Neurosci.* 5, 383–405.

Chance, F. S., Abbott, L., and Reyes, A. D. (2002). Gain modulation from background synaptic input. *Neuron* 35, 773–782.

Churchland, A. K., Kiani, R., and Shadlen, M. N. (2008). Decision-making with multiple alternatives. *Nat. Neurosci.* 11, 693–702.

Cisek, P. (2006). Integrated neural processes for defining potential actions and deciding between them: a computational model. *J. Neurosci.* 26, 9761–9770.

Cisek, P., Puskas, G. A., and El-Murr, S. (2009). Decisions in changing conditions: the urgency-gating model. *J. Neurosci.* 29, 11560–11571.

Cremers, D., and Herz, A. V. M. (2002). Traveling waves of excitation in neural field models: equivalence of rate descriptions and integrate-and-fire dynamics. *Neural. Comput.* 14, 1651–1667.

Destexhe, A., Rudolph, M., and Paré, D. (2003). The high-conductance state of neocortical neurons in vivo. *Nat. Rev. Neurosci.* 4, 739–751.

Ditterich, J. (2006a). Evidence for time-variant decision making. *Euro. J. Neurosci.* 24, 3628–3641.

Ditterich, J. (2006b). Stochastic models of decisions about motion direction: behavior and physiology. *Neural Netw.* 19, 981–1012.

Dorris, M. C., and Glimcher, P. W. (2004). Activity in posterior parietal cortex is correlated with the relative subjective desirability of action. *Neuron* 44, 365–378.

Dorris, M. C., Pare, M., and Munoz, D. P. (2000). Immediate neural plasticity shapes motor performance. *J. Neurosci.* 20, 1–5.

Doubrovinski, K., and Herrman, J. M. (2009). Stability of localized patterns in neural fields. *Neural. Comput.* 21, 1125–1144.

Douglas, R. J., and Martin, K. A. C. (2007). Recurrent neuronal circuits in the neocortex. *Curr. Biol.* 17, R496–R500.

Durstewitz, D. (2004). Neural representation of interval time. *Neuroreport* 15, 745–749.

Eckhoff, P., Wong-Lin, K. F., and Holmes, P. (2009). Optimality and robustness of a biophysical decision-making model under norepinephrine modulation. *J. Neurosci.* 29, 4301–4311.

Furman, M., and Wang, X.-J. (2008). Similarity effect and optimal control of multiple-choice decision making. *Neuron* 60, 1153–1168.

Genovesio, A., Tsujimoto, S., and Wise, S. P. (2006). Neuronal activity related to elapsed time in prefrontal cortex. *J. Neurophysiol.* 95, 3281–3285.

Gerstner, W. (2000). Population dynamics of spiking neurons: fast transients, asynchronous states, and locking. *Neural. Comput.* 12, 43–89.

Gold, J. I., and Shadlen, M. N. (2001). Neural computations that underlie decisions about sensory stimuli. *Trends Cogn. Neurosci.* 5, 10–16.

Gold, J. I., and Shadlen, M. N. (2002). Banburismus and the brain: decoding the relationship between sensory stimuli, decisions, and reward. *Neuron* 36, 299–308.

Gold, J. I., and Shadlen, M. N. (2007). The neural basis of decision making. *Annu. Rev. Neurosci.* 30, 535–574.

Goldman-Rakic, P. (1995). Cellular basis of working memory. *Neuron* 14, 477–485.

Green, D. M., and Swets, J. A. (1966). *Signal Detection Theory and Psychophysics*. New York: Wiley.

Hanes, D. P., and Schall, J. D. (1996). Neural control of voluntary movement initiation. *Science* 274, 427–430.

Higgs, M. H., Slee, S. J., and Spain, W. J. (2006). Diversity of gain modulation by noise in neocortical neurons: regulation by the slow afterhyperpolarization conductance. *J. Neurosci.* 26, 8787–8799.

Huk, A. C., and Shadlen, M. N. (2005). Neural activity in macaque parietal cortex reflects temporal integration of visual motion signals during perceptual decision making. *J. Neurosci.* 25, 10420–10436.

Ipata, A. E., Gee, A. L., Gottlieb, J., Bisley, J. W., and Goldberg, M. E. (2006). LIP responses to a popout stimulus are reduced if it is overtly ignored. *Nat. Neurosci.* 9, 1071–1076.

Janssen, P., and Shadlen, M. N. (2005). A representation of the hazard rate of elapsed time in macaque area LIP. *Nat. Neurosci.* 8, 234–241.

Larkum, M. E., Senn, W., and Luscher, H.-R. (2004). Top-down dendritic input increases the gain of layer 5 pyramidal neurons. *Cereb. Cortex* 14, 1059–1070.

Leon, M. I., and Shadlen, M. N. (2003). Representation of time by neurons in the posterior parietal cortex of the macaque. *Neuron* 38, 317–327.

Luce, R. D. (1986). *Response Times: Their Role in Inferring Elementary Mental Organization*. New York: Oxford University Press.

Mauk, M. D., and Buonomano, D. V. (2004). The neural basis of temporal processing. *Annu. Rev. Neurosci.* 27, 307–340.

McMillen, T., and Behseta, S. (2010). On the effects of signal acuity in a multi-alternative model of decisionmaking. *Neural. Comput.* 22, 539–580.

McPeek, R. M., and Keller, E. L. (2004). Deficits in saccade target selection after inactivation of superior colliculus. *Nat. Neurosci.* 7, 757–763.

Mel, B. W. (1993). Synaptic integration in an excitable dendritic tree. *J. Neurophysiol.* 70, 1086–1101.

Mita, A., Mushiake, H., Shima, K., Matsuzaka, Y., and Tanji, J. (2009). Interval time coding by neurons in the presupplementary and supplementary motor areas. *Nat. Neurosci.* 12, 502–507.

Mountcastle, V. B. (1997). The columnar organization of the neocortex. *Brain* 120, 701–722.

Palmer, J., Huk, A. C., and Shadlen, M. N. (2005). The effect of stimulus strength on the speed and accuracy of a perceptual decision. *J. Vis.* 5, 376–404.

Pouget, A., Dayan, P., and Zemel, R. (2000). Information processing with population codes. *Nat. Rev. Neurosci.* 1, 125–132.

Prescott, S. A., and Koninck, Y. D. (2003). Gain control of firing rate by shunting inhibition: roles of synaptic noise and dendritic saturation. *Proc. Natl. Acad. Sci. U.S.A.* 100, 2076–2081.

Reddi, B. A. J., and Carpenter, R. H. S. (2000). The influence of urgency on decision time. *Nat. Neurosci.* 3, 827–830.

Roitman, J. D., and Shadlen, M. N. (2002). Response of neurons in the lateral intraparietal area during a combined visual discrimination reaction time task. *J. Neurosci.* 22, 9475–9489.

Roxin, A., and Ledberg, A. (2008). Neurobiological models of two-choice decision making can be reduced to a one-dimensional nonlinear diffusion equation. *PLoS Comput. Biol.* 4, 1–13. doi: 10.1371/journal.pcbi.1000046

Salinas, E., and Abbott, L. F. (1996). A model of multiplicative neural responses in parietal cortex. *Proc. Natl. Acad. Sci. U.S.A.* 93, 11956–11961.

Salinas, E., and Sejnowski, T. J. (2001). Gain modulation in the central nervous system: where behavior, neurophysiology, and computation meet. *Neuroscientist* 7, 430–440.

Salinas, E., and Thier, P. (2000). Gain modulation: a major computational principle of the central nervous system. *Neuron* 27, 15–21.

Schall, J. D. (2001). Neural basis of deciding, choosing and acting. *Nat. Rev. Neurosci.* 2, 33–42.

Schall, J. D. (2002). The neural selection and control of saccades by the frontal eye field. *Philos. Trans. R. Soc. Lond.* 357, 1073–1082.

Schall, J. D., and Hanes, D. P. (1993). Neural basis of saccade target selection in frontal eye field during visual search. *Nature* 366, 467–469.

Schultz, W. (2006). Behavioural theories and the neurophysiology of reward. *Annu. Rev. Neurosci.* 57, 87–115.

Schultz, W. (2007). Multiple dopamine functions at different time courses. *Annu. Rev. Neurosci.* 30, 259–288.

Seamans, J. K., and Yang, C. R. (2004). The principal features and mechanisms of dopamine modulation in the prefrontal cortex. *Prog. Neurobiol.* 74, 1–57.

Shen, K., Kalwarowsky, S., Clarence, W., Brunamonti, E., and Pare, M. (2010). Beneficial effects of the NMDA antagonist ketamine on decision processes in visual search. *J. Neurosci.* 30, 9947–9953.

Smith, P. L., and Ratcliff, R. (2004). Psychology and neurobiology of simple decisions. *Trends Neurosci.* 27, 161–168.

Sompolinsky, H., and Shapley, R. (1997). New perspectives on the mechanisms for orientation selectivity. *Curr. Opin. Neurobiol.* 7, 514–522.

Standage, D. I., Trappenberg, T. P., and Klein, R. M. (2005). Modelling divided visual attention with a winner-take-all network. *Neural Netw.* 18, 620–627.

Strogatz, S. (2001). *Nonlinear Dynamics and Chaos: with Applications to Physics, Biology, Chemistry, and Engineering.* Cambridge, MA: Perseus Books Group.

Sugrue, L. P., Corrado, G. S., and Newsome, W. T. (2004). Matching behavior and the representation of value in the parietal cortex. *Science* 304, 1782–1787.

Thevarajah, D., Mikulic, A., and Dorris, M. C. (2009). Role of the superior colliculus in choosing mixed-strategy saccades. *J. Neurosci.* 29, 1998–2008.

Thevarajah, D., Webb, R., Ferrall, C., and Dorris, M. C. (2010). Modeling the value of strategic actions in the superior colliculus. *Front. Behav. Neurosci.* 3:57. doi: 10.3389/neuro.08.057.2009

Thomas, N. W. D., and Pare, M. (2007). Temporal processing of saccade targets in parietal cortex area LIP during visual search. *J. Neurophysiol.* 97, 942–947.

Thompson, K., Hanes, D., Bichot, N., and Schall, J. (1996). Perceptual and motor processing stages identified in the activity of macaque frontal eye field. *J. Neurophysiol.* 76, 440–455.

Trappenberg, T. P. (2008). Tracking population densities using dynamic neural fields with moderately strong inhibition. *Cogn. Neurodyn.* 2, 171–177.

Trappenberg, T. P., Dorris, M. C., Munoz, D. P., and Klein, R. M. (2001). A model of saccade initiation based on the competitive integration of exogenous and endogenous signals in the superior colliculus. *J. Cogn. Neurosci.* 13, 256–271.

Trappenberg, T. P., and Standage, D. I. (2005). Multi-packet regions in stabilized continuous attractor networks. *Neurocomputing* 65–66, 617–622.

Usher, M., and McClelland, J. L. (2001). On the time course of perceptual choice: the leaky competing accumulator model. *Psychol. Rev.* 108, 550–592.

van Veen, V., Krug, M. K., and Carter, C. S. (2008). The neural and computational basis of controlled speed–accuracy tradeoff during task performance. *J. Cogn. Neurosci.* 20, 1952–1965.

Wang, X.-J. (2001). Synaptic reverberation underlying mnemonic persistent activity. *Trends Neurosci.* 24, 455–463.

Wang, X.-J. (2002). Probabilistic decision making by slow reverberation in cortical circuits. *Neuron* 36, 955–968.

Wang, X.-J. (2008). Decision making in recurrent neuronal circuits. *Neuron* 60, 215–234.

White, E. L. (1989). *Cortical Circuits: Synaptic Organization of the Cerebral Cortex; Structure, Function and Theory.* Boston: Birkhauser.

Wilson, H. R., and Cowan, J. D. (1972). Excitatory and inhibitory interactions in localized populations of model neurons. *Biophys. J.* 12, 1–24.

Wilson, H. R., and Cowan, J. D. (1973). A mathematical theory of the functional dynamics of cortical and thalamic nervous tissue. *Kybernetik* 13, 55–80.

Wong, K.-F., Huk, A. C., Shadlen, M., and Wang, X.-J. (2007). Neural circuit dynamics underlying accumulation of time-varying evidence during perceptual decision making. *Front. Comput. Neurosci.* 1:6. doi: 10.3389/neuro.10/006.2007

Wong, K.-F., and Wang, X.-J. (2006). A recurrent network mechanism of time integration in perceptual decisions. *J. Neurosci.* 26, 1314–1328.

Conflict of Interest Statement: The authors declare that the research was conducted in the absence of any commercial or financial relationships that could be construed as a potential conflict of interest.

Received: 27 February 2010; accepted: 26 January 2011; published online: 11 February 2011.

Citation: Standage D, You H, Wang D-H and Dorris MC (2011) Gain modulation by an urgency signal controls the speed–accuracy trade-off in a network model of a cortical decision circuit. Front. Comput. Neurosci. ***5****:7. doi: 10.3389/fncom.2011.00007*

Neural Networks 24 (2011) 1062–1073

Contents lists available at SciVerse ScienceDirect

Neural Networks

journal homepage: www.elsevier.com/locate/neunet

Persistent storage capability impairs decision making in a biophysical network model

Dominic Standage [a,b,*], Martin Paré [a,b,c]

[a] Canadian Institutes of Health Research Group in Sensory-Motor Integration, Queen's University, Canada
[b] Department of Physiology, Queen's University, Canada
[c] Department of Psychology, Queen's University, Canada

ARTICLE INFO

Article history:
Received 18 March 2010
Received in revised form 21 February 2011
Accepted 11 May 2011

Keywords:
Decision making
Persistent mnemonic activity
Network model
NMDA receptor
Working memory
Posterior parietal cortex
Lateral intraparietal area

ABSTRACT

Two long-standing questions in neuroscience concern the mechanisms underlying our abilities to make decisions and to store goal-relevant information in memory for seconds at a time. Recent experimental and theoretical advances suggest that NMDA receptors at intrinsic cortical synapses play an important role in both these functions. The long NMDA time constant is suggested to support persistent mnemonic activity by maintaining excitatory drive after the removal of a stimulus and to enable the slow integration of afferent information in the service of decisions. These findings have led to the hypothesis that the local circuit mechanisms underlying decisions must also furnish persistent storage of information. We use a local circuit cortical model of spiking neurons to test this hypothesis, controlling intrinsic drive by scaling NMDA conductance strength. Our simulations provide further evidence that persistent storage and decision making are supported by common mechanisms, but under biophysically realistic parameters, our model demonstrates that the processing requirements of persistent storage and decision making may be incompatible at the local circuit level. Parameters supporting persistent storage lead to strong dynamics that are at odds with slow integration, whereas weaker dynamics furnish the speed–accuracy trade-off common to psychometric data and decision theory.

1. Introduction

The length and variability of the time needed to discriminate visual stimuli and the susceptibility of this behaviour to errors indicate that decisions intervene between sensory and motor processing (see Schall, 2001, for review). The eye movement system has been invaluable as a model of decision making and experiments on non-human primates show that decisions can be decoded from neural activity in several cortical regions, including the lateral intraparietal area (LIP) of posterior parietal cortex (PPC) (Roitman & Shadlen, 2002; Thomas & Paré, 2007) and the frontal eye fields (FEF) (Schall & Hanes, 1993) and dorsolateral region of pre-frontal cortex (PFC) (Hasegawa, Matsumoto, & Mikami, 2000).

Abstract mathematical models have long provided phenomenological explanations of decision making. Sequential sampling models assume that decision making involves an integration process, where evidence is integrated until a threshold is reached (see Smith & Ratcliff, 2004). Because neural processing is noisy and evidence may be incomplete or ambiguous, integration is slower than the sampling rate, so decisions are based on an average of the evidence and not on momentary fluctuations in processing (see Bogacz, 2007). Several models have addressed the neural mechanisms underlying such a process (Usher & McClelland, 2001; Wang, 2002; Wong & Wang, 2006). The underlying premise of these models is that a discrete population of pyramidal neurons is selective for each decision option, and that competition between these populations is provided by a common pool of inhibitory interneurons. Activity in each stimulus-selective population therefore comes at the expense of the other(s), providing a natural means of selection that scales with the number of decision options. Under constraints with biophysical correlates, mutual inhibition instantiates a calculation of the difference between the evidence favouring each option in two-choice tasks, a process known to optimize speed and accuracy with respect to one another with independent sequential samples (see Bogacz, Brown, Moehlis, Holmes, & Cohen, 2006). Consistent with cortical processing (Douglas & Martin, 2004, 2007), intrinsic (recurrent) activity is crucial to these models, where the time constant of integration depends on a balance between the passive leakage of information and the amplification of information by recurrent activity (Usher & McClelland, 2001).

Biophysically based models predict that NMDA receptors (NMDAR) at intrinsic synapses onto pyramidal neurons provide

* Corresponding address: Department of Physiology, Queen's University, Botterell Hall, Room 453, 18 Stuart Street, K7L 4K9 Kingston, Ontario, Canada. Tel.: +1 613 533 3256; fax: +1 613 533 6880.
E-mail address: standage@biomed.queensu.ca (D. Standage).

0893-6080/$ – see front matter © 2011 Elsevier Ltd. All rights reserved.
doi:10.1016/j.neunet.2011.05.004

an important mechanism underlying the integration of evidence, where their long time constant enables the slow buildup of evidence (Wang, 2002; Wong & Wang, 2006). It is widely believed that intrinsic synapses also provide a mechanism for persistent mnemonic activity following the extinction of a stimulus, though this mechanism is just one of a number of mechanisms hypothesized to support persistent mnemonic activity (see the Discussion). Such activity is extensively correlated with working memory, the active retention of information for use in cognitive tasks (Goldman-Rakic, 1995; Wang, 2001). In this regard, NMDARs are hypothesized to provide an excitatory plateau (Fransén & Lansner, 1995; Lisman, Fellous, & Wang, 1998) while limiting network oscillations (Durstewitz, Seamans, & Sejnowski, 2000; Wang, 1999), a hypothesis supported by observations that injection of NMDA blockers in PFC impairs working memory (Aura & Riekkinen, 1999; Dudkin, Kruchinin, & Chueva, 1997). Because persistent mnemonic activity has been recorded in cortices correlated with perceptual decisions, including PFC (Funahashi, Bruce, & Goldman-Rakic, 1989; Fuster, 1973), FEF (Bruce & Goldberg, 1985) and PPC (Gnadt & Andersen, 1988), it has been proposed that intrinsic excitation strong enough to support persistent mnemonic activity is a property of decision circuits (Wang, 2002, 2008; Wong & Wang, 2006), similar in principle to suggestions that persistent storage (PS) capability may be required for coordinate transformations in PPC (Salinas & Sejnowski, 2001).

To address the hypothesis that decision making relies on local circuit PS capability (Wang, 2002, 2008; Wong & Wang, 2006), we model a decision-correlated circuit in LIP with a spiking implementation (Ardid, Wang, & Compte, 2007; Compte, Brunel, Goldman-Rakic, & Wang, 2000; Furman & Wang, 2008; Gutkin, Laing, Colby, Chow, & Ermentrout, 2001; Ma, Beck, Latham, & Pouget, 2006) of a local circuit model widely used in population and firing rate simulations of cortical circuits (Douglas & Martin, 2007; Pouget, Dayan, & Zemel, 2000; Wilson & Cowan, 1973), including visuospatial maps in PFC (Camperi & Wang, 1998), PPC (Standage, Trappenberg, & Klein, 2005) and frontoparietal cortex (Cisek, 2006). A spiking implementation provides synaptic resolution, enabling the manipulation of intrinsic NMDARs. Unlike earlier models with discrete stimulus-selective neural populations (Usher & McClelland, 2001; Wang, 2002), the model assumes a columnar organization where the strength of intercolumnar pyramidal interactions decreases with axial distance (see Abeles, 1991; Goldman-Rakic, 1995; White, 1989). Combined with unstructured or more broadly tuned synapses onto inhibitory interneurons, this synaptic profile creates centre-surround activity in which pyramidal neurons support each other locally via intrinsic projections and inhibit each other distally via interneurons. This family of networks is often used to model persistent mnemonic activity in visuospatial working memory tasks (Camperi & Wang, 1998; Trappenberg & Standage, 2005), where intrinsic excitation must be sufficiently strong for a selective population to drive itself over a memory interval, necessitating strong inhibition to limit the spread of excitation. These constraints lead to strong intrinsic dynamics that naturally cater to choice selection in decision making tasks, but are potentially at odds with the slow, simultaneous buildup of activity seen in decision-related cortices in multiple-choice tasks (see Schall, 2001).

In simulated visuospatial tasks, we control the network's intrinsic drive by scaling NMDA conductance at intrinsic synapses onto pyramidal neurons. In a simulated visuospatial working memory task, we determine values of this parameter that support (and do not support) PS. In a simulated two-choice visual search task, we measure the decision making abilities of the network for a range of values of this parameter. Our decision making task has no memory component, so there is no *a priori* requirement of local circuit PS capability for task completion. Under parameters consistent with biophysical data, we find that parameters supporting PS lead to intrinsic dynamics too strong for slow integration of evidence, amplifying momentary fluctuations and leading to hasty, inaccurate decisions. The model is a much more accurate decision maker under parameters that do not support PS. Indeed, the best decision making network is far from the PS regime (Fig. 2). In this case, the network enacts a speed–accuracy trade-off with increasing task difficulty (eg. Palmer, Huk, & Shadlen, 2005), simulated reaction times and their distributions are consistent with those of psychophysical experiments, and simulated neural data are consistent with neural recordings in LIP during visual search tasks. This finding is different from that of earlier studies, but the mechanisms underlying it are much the same. Intrinsic processing fosters a balance between leakage and amplification of accumulated evidence (Usher & McClelland, 2001) that corresponds to a given NMDAR conductance strength (Wang, 2008). Under our parameters, the balance that best supports the task is outside the PS regime.

Our results fit with a distributed framework in which no single microcircuit is responsible for all aspects of a decision task, but where different functions (e.g. integration of evidence and choice selection) are mediated by different circuits (Beck et al., 2008). Our results further speak to the functions of decision-related cortical regions in distributed circuitry. For example, the prediction that decision circuits in LIP are characterized by weak intrinsic dynamics is consistent with reports that LIP represents the relative importance of items in the visual field (Goldberg, Bisley, Powell, & Gottlieb, 2006; Serences & Yantis, 2006), a function for which categorical dynamics are not well suited. The difference between our findings and those of earlier studies is explained by consideration of the network's time constant of integration, optimization of which is parameter dependent. We thus do not claim that PS capability cannot be a property of local circuits mediating decision processes, but under biophysically realistic parameters, we demonstrate the potential incompatibility of persistent mnemonic activity and decision making in the same local circuit at the same time.

2. Materials and methods

We simulated a decision circuit in LIP with a fully connected recurrent network of leaky integrate-and-fire neurons (Tuckwell, 1988) with 1000 pyramidal neurons and 250 interneurons, depicted in Fig. 1(A). Intrinsic (recurrent) activity from pyramidal cells was mediated by AMPA and NMDA conductances and from interneurons by GABA conductances (Fig. 1(B)). The strength or *weight* of pyramidal-to-pyramidal synapses was thus scaled by a decreasing function of spatial location (see Abeles, 1991; Goldman-Rakic, 1995; White, 1989), added to a baseline weight (Ardid et al., 2007; Compte et al., 2000; Tegnér, Compte, & Wang, 2002) (Fig. 1(C)). Combined with unstructured synapses between pyramidal cells and inhibitory interneurons, this synaptic profile creates a centre-surround network where pyramidal neurons support each other locally via intrinsic projections and inhibit each other distally via interneurons. In simulated visuospatial working memory and visual discrimination tasks, stimuli were simulated by Poisson spike trains where spike rates were drawn from a normal distribution and the mean corresponded to the centre of a Gaussian receptive field, depicted in Fig. 1(A) for the discrimination task. Spike response adaptation among upstream, visually responsive neurons was mimicked by a decaying function of input rate (Trappenberg, Dorris, Munoz, & Klein, 2001; Wong, Huk, Shadlen, & Wang, 2007) with a 40 ms (Thomas & Paré, 2007) response delay (Fig. 1(D)). These selective inputs were superimposed on non-selective Poisson input spikes that lead to background spike

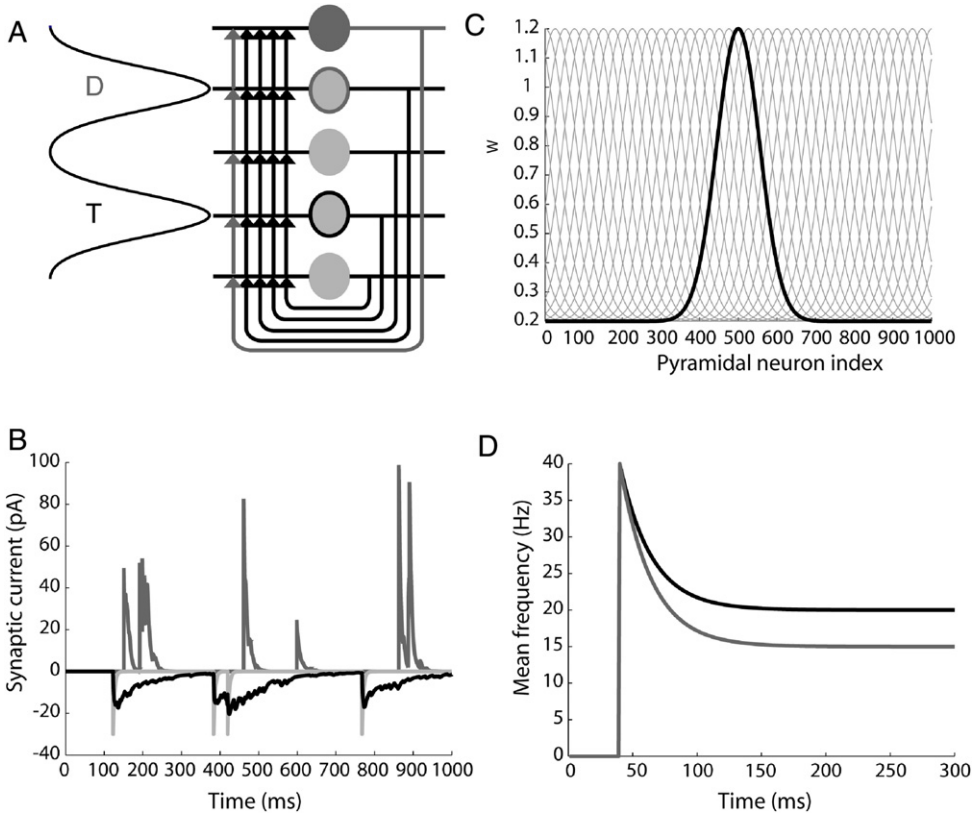

Fig. 1. (A) Fully recurrent network of pyramidal neurons (light grey with black projections) and interneurons (dark grey neuron and projections). The 4/1 ratio of pyramidal neurons to interneurons preserves population sizes in the spiking model (1000/250). Target (T) and distractor (D) neurons are given Gaussian RFs and are outlined in black and dark grey respectively. (B) Intrinsic AMPA (light grey) and NMDA (black) currents onto a pyramidal neuron are consistent with *in vitro* recordings from cortical slices (e.g. Wang et al., 2008). Currents are shown at the peak of the connectivity structure in *C* and are thus mediated by the strongest intrinsic synapses in the model. GABA currents onto the same neuron are shown in dark grey and are also consistent with *in vitro* cortical data (e.g. Galarreta & Hestrin, 1998). (C) Structured pyramidal-to-pyramidal weights W. Black curve shows weights to all pyramidal neurons from neuron 500. Grey curves show periodic shift-invariance of W. (D) Mean input frequency at the centre of the target (black) and distractor (grey) RFs during the stimulus interval. Curves are shown for the easiest level of target–distractor similarity ($\gamma_{NMDA} = 0.75$). Only the first 300 ms is shown.

rates of 1–2 Hz among pyramidal neurons and 7–8 Hz among interneurons (Destexhe & Paré, 1999), depending on the strength of intrinsic NMDARs.

Each model neuron is described by

$$C_m dV/dt = -g_L(V - E_L) - I,$$

where C_m is the membrane capacitance of the neuron, g_L is the leakage conductance, V is the membrane potential, E_L is the equilibrium potential, and I is the total input current. When V reaches a firing threshold ϑ_V, it is reset to V_{res}, after which it is unresponsive to its input for an absolute refractory period τ_{ref}. For pyramidal neurons, $C_m = 0.5$ nF, $g_L = 25$ nS, $E_L = -70$ mV, $\vartheta_V = -50$ mV, $V_{res} = -60$ mV and $\tau_{ref} = 2$ ms. For interneurons, $C_m = 0.2$ nF, $g_L = 20$ nS, $E_L = -70$ mV, $\vartheta_V = -50$ mV, $V_{res} = -60$ mV and $\tau_{ref} = 1$ ms (Compte et al., 2000; Wang, 1999).

The total input current I is given by

$$I = I^{ext}_{AMPA} + I_{AMPA} + I_{NMDA} + I_{GABA}.$$

For each neuron, I^{ext}_{AMPA} is AMPAR-mediated afferent current, and I_{AMPA}, I_{NMDA} and I_{GABA} are the summed AMPAR, NMDAR, and GABAR currents from recurrent synapses. These currents are each defined by

$$I_{syn} = G \cdot g(V - V_{syn}) \cdot \eta \cdot W \cdot \kappa, \quad (1)$$

where subscript *syn* refers to $\{AMPA^{ext}, AMPA, NMDA, GABA\}$. For each synapse contributing to the current, G is the conductance strength, g is the receptor activation, V_{syn} is the synaptic reversal potential, η captures the voltage dependence of NMDARs (set to 1 for AMPARs and GABARs and described below for NMDARs) and κ is a scale factor (set to 1 for all intrinsic synapses and described below for extrinsic activity). The constant W distinguishes between structured and unstructured network connections (see below). For AMPA and NMDA synapses, $V_{syn} = 0$ mV. For GABA synapses, $V_{syn} = -70$ mV. For AMPARs and GABARs, the receptor activation g follows a step-and-decay formula $dg/dt = -g/\tau_g + \delta(t - t_f)$, where δ is the Dirac delta function and t_f is the time of firing of a pre-synaptic neuron. The decay constant τ_g is given values $\tau_{AMPA} = 4$ ms (Gonzalez-Burgos et al., 2008) and $\tau_{GABA} = 10$ ms (Salin & Prince, 1996) respectively for these synapses. For NMDA currents, g has a slower rise and decay and is described by

$$dg_{NMDA}/dt = -g_{NMDA}/\tau_{NMDA} + \alpha_{NMDA} \cdot x_{NMDA}(1 - g_{NMDA}),$$

where $\tau_{NMDA} = 100$ ms (Wang, Stradtman, Wang, & Gao, 2008), $\alpha_{NMDA} = 0.5$ kHz controls receptor saturation, and x_{NMDA} is defined by

$$dx_{NMDA}/dt = -x_{NMDA}/\tau_x + \delta(t - t_f).$$

Decay constant τ_x is set to 2 ms. The voltage dependence of NMDARs is captured by $\eta = 1/(1 + Mg \cdot \exp(-0.062 \cdot V)/3.57)$, where $Mg = 1$ mM describes the extracellular Magnesium concentration (Jahr & Stevens, 1990). Conductance strengths G at recurrent synapses are $G_{AMPA,p} = G_{AMPA,i} = 0.5$ nS, $G_{NMDA,p} = 4.1$ nS, $G_{NMDA,i} = 2.5$ nS, $G_{GABA,p} = 6$ nS, and $G_{GABA,i} = 5.75$ nS, where subscripts p and i refer to synapses onto pyramidal neurons and interneurons respectively. The strength of extrinsic AMPA conductances onto pyramidal neurons and interneurons are $G^{ext}_{AMPA,p} = 2.75$ nS and $G^{ext}_{AMPA,i} = 2$ nS respectively. Example currents mediated by these synapses are shown in Fig. 1(B).

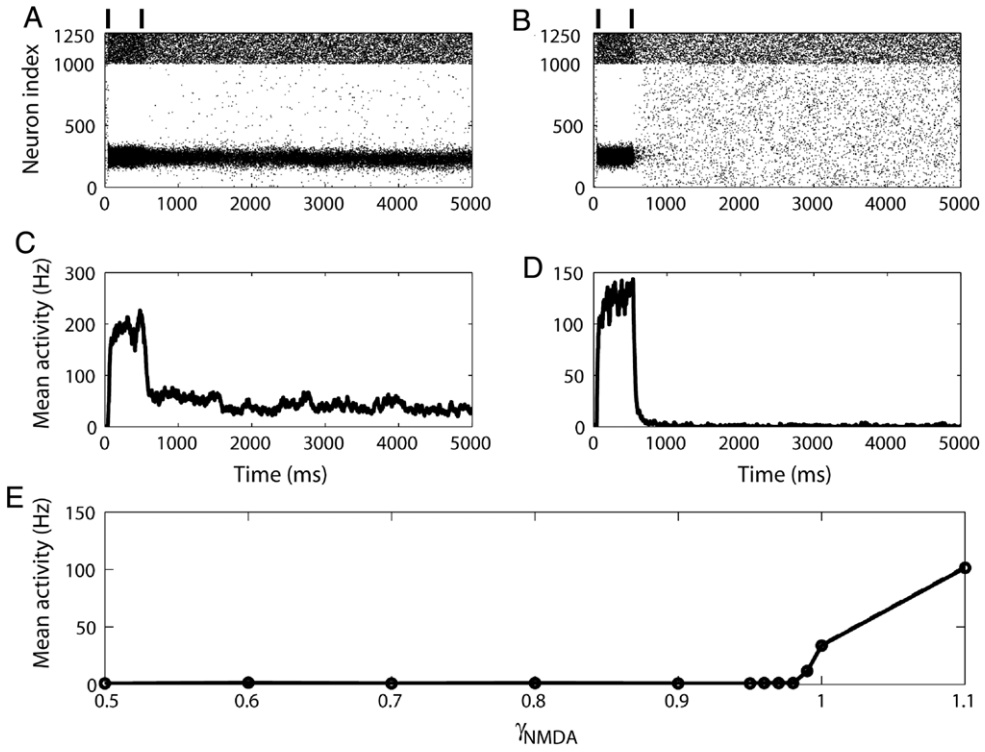

Fig. 2. Establishing persistent storage (PS) parameters in the model. (A–D) Rasters and spike density functions (SDF, rounded to the nearest millisecond) for a simulated PS task in which the stimulus interval (first 500 ms) was followed by a memory interval (5000 ms, no selective input) under parameters that support (A, C, $\gamma_{NMDA} = 1$) and do not support (B, D, $\gamma_{NMDA} = 0.8$) PS. SDFs were built by convolving spike trains with a rise and decay function $(1 - exp(-t/\tau_r) \cdot \exp(-t/\tau_d)/(\tau_d^2/(\tau_r + \tau_d)))$ where t is the time following stimulus onset, and $\tau_r = 1$ ms and $\tau_d = 20$ ms are the time constants of rise and decay respectively (Thompson et al., 1996). In rasters, pyramidal cells are indexed from 1–1000. Interneurons are indexed from 1001–1250. The beginning (40 ms) and end (540 ms) of the stimulus interval are indicated by the vertical bars at the top of the figure. Selective input was provided at the target only and SDFs are averaged over the target-selective population (41 neurons, see Discrimination Time). (E) Mean population SDF (solid curve) over the final 1000 ms of the memory interval for $\gamma_{NMDA} = \{1.1, 1.0, 0.99, 0.98, 0.97, 0.96, 0.9, 0.8, 0.7, 0.6, 0.5\}$. For $\gamma_{NMDA} = 1$ (PS baseline) the network supports PS. For $\gamma_{NMDA} \leq 0.98$, the network shows no mnemonic activity. $\gamma_{NMDA} = 0.99$ is effectively the PS border. The dashed curve shows the population spike count rate over the same interval. The two curves are barely distinguishable.

2.1. Structured pyramidal-to-pyramidal synapses

All pyramidal-to-interneuron, interneuron-to-interneuron and interneuron-to-pyramidal and extrinsic synapses are unstructured, so in Eq. (1), $W = 1$ for all these cases. For pyramidal-to-pyramidal synapses, W is a Gaussian function of the distance between neurons in a ring. The weight $W_{i,j}$ between any two pyramidal neurons i and j is thus given by

$$W_{i,j} = \lambda + exp(-d^2/2\sigma^2),$$

where $\lambda = 0.2$ provides an unstructured baseline weight between all pyramidal neurons (Ardid et al., 2007; Compte et al., 2000; Tegnér et al., 2002), $d = \min(|i - j|dx, 2\pi - |i - j|dx)$ defines distance in the ring, $dx = 2\pi/N_E$ is a scale factor and $\sigma = 0.35(20^\circ)$. Pyramidal-to-pyramidal weights are depicted in Fig. 1(C).

2.2. Background activity

Extrinsic currents $I^{ext}_{AMPA,\{p,i\}}$ mediate non-selective background activity, simulating background firing from other brain regions and generating background activity in the network. We simulate the convergent activity of 1000 pre-synaptic neurons firing independent, homogeneous Poisson spike trains at 1 Hz each with a single homogeneous Poisson spike train at 100 Hz, where the conductance strength $G^{ext}_{AMPA,\{p,i\}}$ is scaled by $\kappa = 10$, trading spatial and temporal summation (Prescott & De Koninck, 2003).

2.3. Visual discrimination task

Our discrimination task corresponds to a visual search task with two stimuli, one of which is designated the target by virtue of a feature contrast difference. Following a 300 ms equilibration period (background activity only), the spike rates of the target and distractor stimuli were drawn from a normal distribution with mean μ corresponding to the centre of a Gaussian RF defined by $\exp(-d^2/2\sigma^2_{ext})$. Constant d is given above for structured weights W and $\sigma_{ext} = 0.52(30^\circ)$. The target and distractor RF centres were separated from each other by 180° in the ring network. Spike response adaptation in upstream visually responsive neurons is modelled by a step-and-decay function (Trappenberg et al., 2001; Wong et al., 2007)

$$d\mu/dt = (\mu - \mu_{init}/\mu_{div} \cdot \gamma_\mu)/\tau_\mu + \mu_{init}\delta(t - \alpha_\mu),$$

where $\mu_{div} = 2$ determines the asymptotic input spike rate, $\tau_\mu = 25$ ms determines the rate of (upstream) spike response adaptation, and $\alpha_\mu = \Delta t$ ms is the onset of selective input following the 40 ms visual response delay, prior to which $\mu = 0$. Constant γ_μ is set to 1 for the target and to γ_{ext} for the distractor, where $0.75 \leq \gamma_{ext} \leq 0.99$ determines target–distractor similarity. As with non-selective inputs, $G^{ext}_{AMPA,p}$ is scaled by $\kappa = 10$. With an initial frequency $\mu_{init} = 400$ Hz, our selective inputs thus approximate a population of 100 upstream neurons firing at an initial rate of 40 Hz, attenuating to rates of 20 Hz and $20 \cdot \gamma_{ext}$ Hz at the target and distractor neurons respectively (Chafee & Goldman-Rakic, 1998; Paré & Wurtz, 1997), depicted in Fig. 1(D). Simulations were run with timestep $\Delta t = 0.1$ ms and the standard forward implementation of Euler's method, and were verified with the standard fourth order Runge–Kutta method.

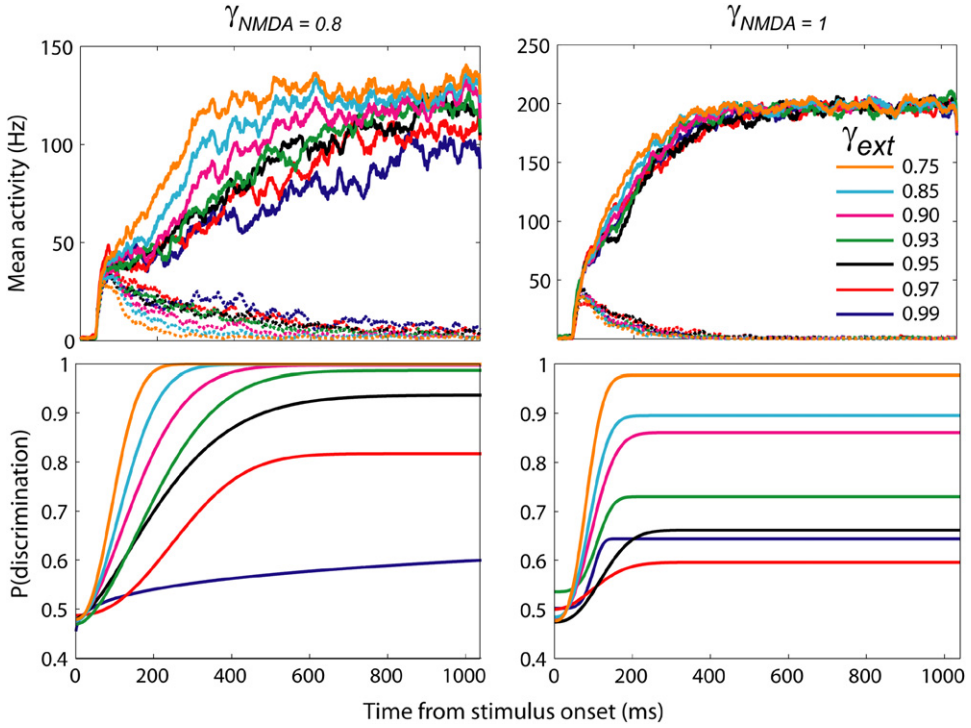

Fig. 3. (Top) Mean spike density (100 trials) at the target and distractor neurons for each level of target–distractor similarity γ_{ext} (see legend, top right). Correct trials only. In the non-PS network ($\gamma_{NMDA} = 0.8$, left) target and distractor activation is slower to diverge with increasing task difficulty. Mean spike densities for the PS baseline network ($\gamma_{NMDA} = 1$, right) are similar for all task difficulties. (Bottom) Quantifying the probability of target discrimination. Weibull fits to AUROCs (see text) calculated at the target and distractor neurons. With increasing task difficulty, curves from the non-PS network asymptote with increasing latency, trading speed for accuracy (left). All curves from the PS baseline network asymptote with similar latency, with corresponding loss of accuracy (right).

3. Results

3.1. Establishing persistent storage parameters

We determined the PS capability of the network as a function of the strength of intrinsic NMDARs, multiplying conductance strength at these synapses by a factor γ_{NMDA}. Fig. 2 shows results from a simulated visuospatial working memory task in which the network was driven for 500 ms by selective input (stimulus interval) followed by 5000 ms without selective input (memory interval). Raster plots are shown on the top row and spike density functions (SDF, see Fig. 2 caption) in the middle row. Spike rates are consistent with LIP data (e.g. Thomas & Paré, 2007). As shown on the left of the figure (top two rows), for $\gamma_{NMDA} = 1$, the network supports persistent neural activity during the memory interval at a much lower rate than during the stimulus interval (Paré & Wurtz, 1997). The network is thus inside the PS regime, but close to the onset of PS dynamics, previously suggested to be optimal for decision circuits (Wang, 2002). We refer to this configuration as PS baseline. The network on the right does not support PS ($\gamma_{NMDA} = 0.8$), as evidenced by the cessation of stimulus-selective activation during the memory interval.

The bottom row of the figure plots the respective firing rates for $0.5 \leq \gamma_{NMDA} \leq 1.1$ over the last 1000 ms of the memory interval. For $\gamma_{NMDA} \geq 1$, the network supports PS, where higher rates are due to higher values of γ_{NMDA}. For $\gamma_{NMDA} = 1.1$ (referred to as strong PS below), the network supports strong PS states, but beyond this parameter value (increments of 0.1), the network develops persistent, selective states from background noise. Consequently, we do not consider $\gamma_{NMDA} > 1.1$. Note that the bottom row does not show the rate of decline of activation following removal of the stimulus; among the non-PS networks, stimulus-selective activation drops off more slowly with higher values of γ_{NMDA}. For $\gamma_{NMDA} = 0.8$ (above right), the drop-off in activation is very sharp, indicating that the network is far from the PS regime. Unless otherwise specified, we refer to this configuration as 'the non-PS network' below.

3.2. Simulated visual discrimination task

We simulated a two-choice visual discrimination task by centring extrinsic activity at two network locations for 1000 ms, one designated the target and the other the distractor. Initial 'visual' responses were equal (Thomas & Paré, 2007) and the rate of target and distractor inputs diverged to separate steady states (Trappenberg et al., 2001; Wong et al., 2007), determining their similarity (and thus task difficulty). Average input spike rates at the target and distractor RF centres (henceforth the target neuron and distractor neuron respectively) are shown in Fig. 1(D). We ran 100 trials of the two-choice task for a range of target–distractor similarities γ_{ext} and NMDA scale factors γ_{NMDA}, recording the spike times of each neuron in the network. Fig. 3 (top row) shows mean activation of the target and distractor neurons on correct trials (see Discrimination Time) for the two values of γ_{NMDA} shown for the visuospatial working memory task in Fig. 2. For the non-PS network, target and distractor activation is slower to diverge and less distinguishable as input similarity increases, consistent with reaction times and recordings from PPC during visual discrimination tasks (Roitman & Shadlen, 2002). Regardless of task difficulty, activation follows an invariant profile in the PS baseline network.

3.3. Discrimination accuracy

We used signal detection theory (Green & Swets, 1966) to determine how well an ideal observer could discriminate between the target and the distractor from spiking activity in the model, estimating the separation of the distributions of target and

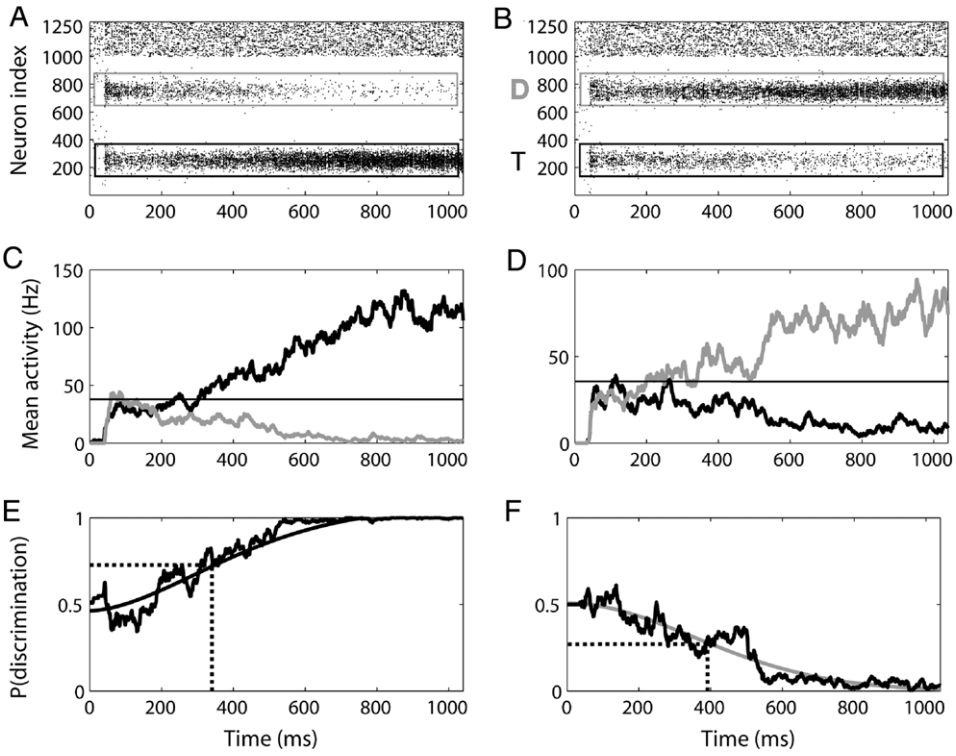

Fig. 4. Determining discrimination time in the two-choice task. A correct trial (A, C, E) and error trial (B, D, F) where $\gamma_{NMDA} = 0.8$ and $\gamma_{ext} = 0.97$. (A, B) In raster plots, pyramidal neurons are indexed 1–1000. Interneurons are indexed 1001–1250. Target (T) and distractor (D) neurons are numbered 250 and 750 respectively. Stimulus interval begins at 40 ms. (C, D) Mean spike densities for target (black) and distractor (grey) populations (41 neurons each). Horizontal black bars depict threshold method for checking discrimination time (see text). (E, F) AUROC and Weibull fits corresponding to spike densities above. Dotted black bars indicate discrimination time, when the Weibull function reaches 0.75 on correct trials and 0.25 on error trials.

distractor activity at successive 1 ms intervals. To this end, we calculated receiver operating characteristic curves (ROC) from the mean activation of the target and distractor neurons over the 100 trials. The area under the ROC (AUROC) quantifies the separation of their distributions (see Thompson, Hanes, Bichot, & Schall, 1996). We quantified the probability of neuronal discrimination by a least squares fit of the AUROCs to a Weibull function

$$w(t) = \gamma - (\gamma - \delta) \cdot \exp(-(t/\alpha)^{\beta}) \quad (2)$$

where t is the time after stimulus onset, α is the time at which the function reaches 64% of its maximum, β is the slope, and γ and δ are the upper and lower limits of the function respectively. Discrimination magnitude (accuracy) was the upper limit of the function.

Fig. 3 (bottom row) shows w for all levels of target–distractor similarity for the PS baseline network and for the best-performing non-PS network. Our ideal observer analysis shows that both networks quickly discriminate the target from the distractor on the easiest task, but as the task is made harder, only the non-PS network discriminates more slowly, reaching a high level of accuracy for all but the hardest task. The non-PS network thus trades speed for accuracy with increasing task difficulty, consistent with neural and psychometric data from subjects performing visual discrimination tasks (eg. Palmer et al., 2005; Roitman & Shadlen, 2002). In contrast, the PS baseline network cannot enact this trade-off, evidenced by the early asymptotes of these curves at low values. The strong PS network performs even worse (not shown).

3.4. Discrimination time

We quantified the timecourse of neuronal discrimination by calculating AUROCs for a population of target and distractor-selective neurons during each trial. The population $p = 41$ included the target neuron, the distractor neuron, and an additional 20 neurons either side of these RF centres. The fitting procedure on each trial was thus equivalent to that described above for determining accuracy across all trials, but averaged over p neurons instead of 100 trials. Additionally, because either the target or distractor population could dominate the network on any given trial (correct and error trials respectively), the AUROCs could be correspondingly fit with increasing or decreasing Weibull functions w. On error trials (decreasing function), α in Eq. (2) refers to the time at which w reached 64% of $1 - \min(w)$, and γ and δ are the lower and upper limits respectively. The time at which w reached 0.75 was considered the discrimination time (Thompson et al., 1996) (0.25 on error trials). We averaged discrimination times (DT) over all trials to determine the speed of decision making under each combination of task difficulty and strength of recurrent NMDARs, depicted in Fig. 4. Trials on which w reached neither 0.75 nor 0.25 were discarded. For difficult tasks with weak recurrent NMDARs ($\gamma_{ext} \geq 0.97$ & $\gamma_{NMDA} < 0.7$) there were substantial numbers of discarded trials with a 1000 ms stimulus interval (see Fig. 6 caption), but results under these parameter values are informative about the discrimination abilities of the network because an ideal observer analysis does not require categorical choice. Quantifying DT on a trial-by-trial basis allows direct comparison with psychometric data, but if there is little to discriminate between target and distractor stimuli, it is reasonable not to choose at all, as in non-forced choice tasks. This important decision-theoretic issue is considered in the Discussion.

We compared the above method for determining the time-course of discrimination with an alternative method, similar to that of Wang (2002), comparing the mean activity of the target and distractor populations to a threshold frequency. Under this method, DT was considered to be the time at which the target

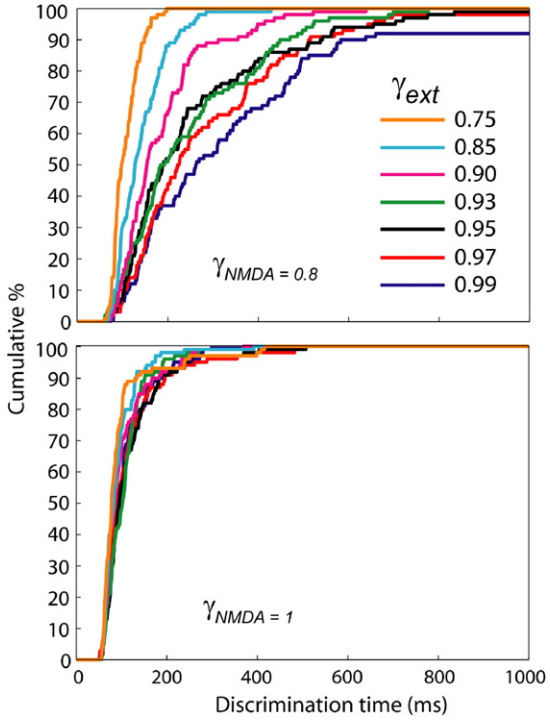

Fig. 5. Cumulative distribution of discrimination times for the best-performing non-PS network ($\gamma_{NMDA} = 0.8$, top) and the PS baseline network ($\gamma_{NMDA} = 1$, bottom) for all levels of target–distractor similarity γ_{ext}. Discrimination times are broader with longer tails with increasing task difficulty for the non-PS network, but are approximately constant for the PS network.

activity (distractor activity for error trials) exceeded this threshold, with the additional constraints that (1) one activation function remain above threshold for 100 ms and (2) the other concurrently remain below threshold for 100 ms. These additional constraints served to distinguish the initial 'visual' response from the subsequent, decision-related activity. Results under the two methods were similar for thresholds between approximately 20 and 60 Hz. We do not systematically investigate the similarities between the two methods here, though we note that their use captures a subtle distinction in the context of distributed processing. ROC analysis implements an ideal observer of the network, akin to a downstream circuit making decisions based on the network's activity (e.g. the superior colliculus reading out LIP activity). A neural threshold enables the network to make its own decisions, i.e. without an observer of its activity. However, in a model with competitive interactions between selective populations, the reaching of the threshold by one population entails a difference between its activation and that of the other, the same criterion used by ROC analysis to discriminate between the two populations. It is thus not surprising that the two methods yield similar results. See Standage, You, Wang, and Dorris (in press) for a dynamic systems perspective on ROC with a network from the same family as this one.

As expected due to the longer latency of maximum discrimination as a function of task difficulty (Fig. 3, bottom left), mean DTs for the best-performing network increased with target–distractor similarity, rising from 109 ms to 283 ms as γ_{ext} was increased from 0.75 to 0.99. These DTs not only indicate a speed–accuracy tradeoff on a trial-by-trial basis, but are consistent with reaction times in visual search tasks (Thomas & Paré, 2007). In contrast, mean DTs for the PS baseline network showed a very slight increase from 97 ms to 107 ms as task difficulty was increased.

Fig. 5 shows cumulative distributions of DTs for the non-PS network and the PS baseline network. Not only does mean DT increase with task difficulty in the non-PS network (62% from the easiest to hardest task), but so does the standard deviation (84%), consistent with greater variability in reaction times with increasing task difficulty in monkeys performing a visual search task (Cohen et al., 2007). Furthermore, DT distributions show an increasingly long tail with increasing task difficulty ($0.75 \leq \gamma_{ext} < 0.99$), consistent with typical human reaction times in decision making tasks (see Smith & Ratcliff, 2004) and mathematical models known to be optimal for two-choice tasks (Bogacz et al., 2006). Not only are mean DTs approximately constant across task difficulty in the PS baseline network (increasing by 9% from the easiest to hardest task), but their standard deviations *decrease* by 18%.

3.5. Target discrimination with PS and non-PS networks

Fig. 6 shows mean discrimination accuracy and time as functions of target–distractor similarity for a range of values of γ_{NMDA}. The top figure shows results for accuracy. The curves cluster for the easiest and most difficult tasks, though values of γ_{NMDA} leading to the strongest and weakest recurrent dynamics furnish the least accurate networks. For task difficulties between these extremes, accuracy steadily improves as the strength of recurrent NMDARs is reduced from $\gamma_{NMDA} = 1.1$ to $\gamma_{NMDA} = 0.8$. This effect bottoms out at $\gamma_{NMDA} = 0.7$ and network accuracy decreases for $\gamma_{NMDA} = 0.6$, comparable to (though slightly better than) the PS baseline network. At $\gamma_{NMDA} = 0.5$, the network is less accurate than baseline, performing comparably to the strong PS network.

The bottom figure shows results for DT. The curves cluster for the easiest level of target–distractor similarity, much like the accuracy curves above. In general, as the task is made harder, all networks except the strong PS network show an increase in DT, though this effect is slight for PS baseline (an increase of ∼10% from the easiest to the hardest task). This increase in DT with task difficulty is more pronounced as γ_{NMDA} is reduced, though for $\gamma_{NMDA} \leq 0.6$, the network makes too few decisions to be useful as a categorical decision maker. Indeed, these two parameter values yield no decisions at all for the hardest task (see Fig. 6 caption). Such a non-committal description of ambiguous evidence could be valuable to a downstream integrator reading the output of more than one circuit (see the Discussion). Note that longer DTs coincide with lower accuracy for $\gamma_{NMDA} \leq 0.6$ because the network is dominated by leakage of information (see Discussion and Supplementary Material).

We checked that decision making followed a performance gradient near the onset of PS dynamics by running simulations with $\gamma_{NMDA} = \{0.99, 0.97, 0.95, 0.93\}$. These parameter values lead to results for accuracy and DT that transitioned smoothly between PS baseline and $\gamma_{NMDA} = 0.9$, shown by the thin solid curves in Fig. 6 for $\gamma_{NMDA} = 0.95$. Notably, for $\gamma_{NMDA} = 0.99$, network performance was nearly indistinguishable from PS baseline (not shown).

3.6. Robustness of the results

Our study is based on earlier work in which the long time constant of NMDARs at intrinsic synapses onto pyramidal neurons was hypothesized to support persistent mnemonic activity and the integration of evidence in decision processing (Wang, 2002, 2008; Wong & Wang, 2006). We followed these authors in using an NMDAR time constant of $\tau_{NMDA} = 100$ ms, but measurements of τ_{NMDA} differ according to experimental methods, receptor subtype and function (see Cull-Candy, Brickley, & Farrant, 2001; Cull-Candy & Leszkiewicz, 2004). The value of τ_{NMDA} used here and in earlier work is consistent with the upper end of measurements for intrinsic cortical processing, so we also ran simulations with $\tau_{NMDA} = 50$ ms, consistent with measurements at the lower end of the data (Kumar & Huguenard, 2003; Wang et al., 2008). Under this

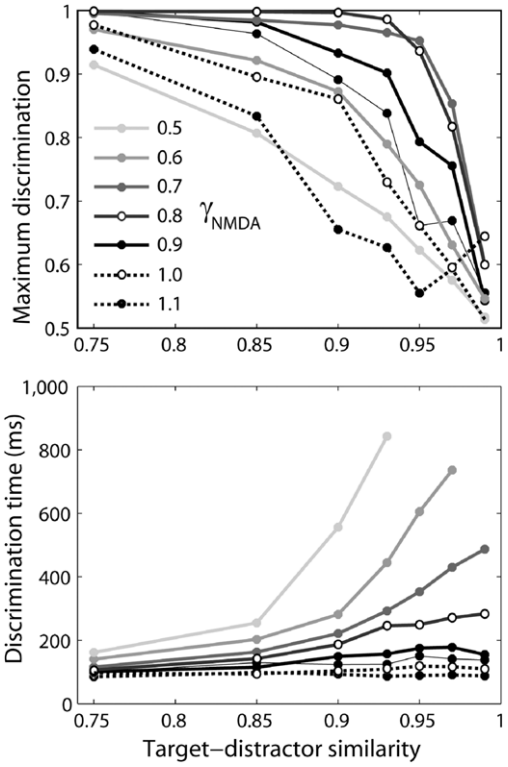

Fig. 6. Accuracy (top) and speed (bottom) of target discrimination in the model. Dotted curves correspond to PS networks, where open and closed circles show PS baseline ($\gamma_{NMDA} = 1$) and strong PS ($\gamma_{NMDA} = 1.1$) respectively. Solid curves correspond to non-PS networks, where lighter curves correspond to lower values of γ_{NMDA} ($0.5 \leq \gamma_{NMDA} \leq 0.95$, see colour legend). Results from the best-performing network ($\gamma_{NMDA} = 0.8$) are plotted with open circles. The thin black curves (one in each figure) correspond to $\gamma_{NMDA} = 0.95$. The bottom figure shows that the weakest networks do not make decisions on the hardest tasks with a stimulus interval of 1 s and discrimination criterion of 0.75 (see Results, Discrimination time). For $\gamma_{NMDA} = 0.5$, the network makes decisions on 35% of trials for $\gamma_{ext} = 0.9$, 8% for $\gamma_{ext} = 0.93$ and 0% for $\gamma_{ext} \geq 0.95$. For $\gamma_{NMDA} = 0.6$, the network makes decisions on 85% of trials for $\gamma_{ext} = 0.93$, 44% for $\gamma_{ext} = 0.95$, 7% for $\gamma_{ext} = 0.97$ and 0% for $\gamma_{ext} = 0.99$. For $\gamma_{NMDA} = 0.7$, the network makes decisions on 75% of trials for $\gamma_{ext} = 0.97$ and 44% for $\gamma_{ext} = 0.99$. All other combinations of γ_{NMDA} and γ_{ext} yield decisions on more than 90% of trials.

parameter value, the PS network corresponded to $\gamma_{NMDA} = 1.2$, while $\gamma_{NMDA} = 0.8$ was far outside the PS regime. The shorter NMDAR time constant did not qualitatively effect our results (Fig. 7, solid curves).

To determine if the results depend on the details of selective input, we ran 100 trials with the PS baseline network and the non-PS network, where the initial input rate at the target RF centre was reduced from 400 to 200 Hz — simulating 100 upstream visually responsive neurons at 20 Hz instead of 40 Hz. We also ran 100 trials with a step input (no decay) at 100 Hz. These alternate input parameters did not qualitatively affect the results (not shown). As long as the inputs were strong enough to furnish a transition from extrinsic to intrinsic processing (Douglas & Martin, 2004, 2007; Wilson & Cowan, 1973), results were qualitatively invariant.

We also examined the signal-to-noise ratio (SNR) of the selective input. This ratio is determined by the relative rates of background and selective input spike trains and the spatial and temporal profiles of selective input. At the centre of the target RF, the selective input SNR was 4 in the simulations above, decaying to 2 with a time constant of 25ms (see Methods). This ratio is within range of neuronal responses in LIP (Paré & Wurtz, 2001), but is two orders of magnitude higher than in earlier work in which PS capability was advantageous in a network model of a decision circuit (Wang, 2002). This difference remains when the

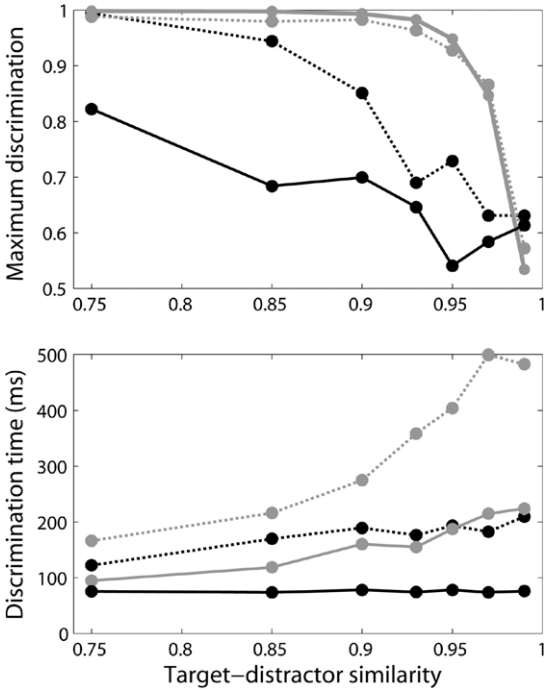

Fig. 7. Accuracy (top) and speed (bottom) of target discrimination under alternative parameters. Persistent storage (PS) capability impaired decision making in the network when simulations were run with a shorter NMDA time constant ($\tau_{NMDA} = 50$ ms, solid curves) and when the signal-to-noise ratio of selective inputs and the strength of synaptic conductances were decreased (dotted curves, see Robustness of the Results). Black and grey curves correspond to PS and non-PS networks respectively.

SNR is integrated over the RFs (Gaussian vs. square) and temporal input profiles (step-and-decay vs. step only) used in each study, normalized for network size and trial length. Synaptic conductance strength also differed markedly (one order of magnitude greater here), so we reduced both these differences to further test the robustness of our findings. All synaptic conductance strengths were divided by 2, the background rate was multiplied by 2 and selective rates were multiplied by 3/4. We ran 100 trials across all task difficulties for PS baseline and the non-PS network and we confirmed that these new configurations remained inside and outside the PS regime respectively. These simulations further demonstrated that the specific values of our original parameters are not crucial to our findings. Accuracy was very similar to Fig. 6 for both configurations. DTs were longer than in Fig. 6, but were well within range of DTs in visual search tasks (Fig. 7, dotted curves). These simulations do not exhaust the parameter variations that may affect our results, but they address major differences between our model and earlier modelling work where results differed from ours (Wang, 2002; Wong & Wang, 2006). Further parameter dependence is described in the Discussion.

4. Discussion

We have interpolated between strong and weak dynamics in a spiking network model of a decision circuit in LIP, investigating the hypothesized dependence of decision making on local circuit PS capability (Wang, 2002, 2008; Wong & Wang, 2006). Building on earlier studies demonstrating the potential importance of intrinsic NMDARs to persistent mnemonic activity (Compte et al., 2000; Durstewitz et al., 2000; Fransén & Lansner, 1995; Lisman et al., 1998; Tegnér et al., 2002; Wang, 1999) and decision making (Wang, 2002; Wong & Wang, 2006), we systematically controlled both these functions by manipulating the strength of

NMDA conductance at intrinsic synapses onto pyramidal neurons. We controlled task difficulty by manipulating target–distractor similarity in a simulated visual search task, finding that parameters that support PS entail poor decision making. Non-PS parameters (far from the PS regime, see Fig. 2) enable more effective integration of decision options for a broad range of task difficulties, yielding signature characteristics of reaction time distributions and reproducing the speed–accuracy trade-off predicted by decision theory (Ratcliff & Smith, 2004; Smith & Ratcliff, 2004) and shown by psychometric data from visual discrimination tasks (eg. Churchland, Kiani, & Shadlen, 2008; Palmer et al., 2005; Roitman & Shadlen, 2002).

While this finding is different from those of earlier studies, the principle mechanisms at play are not. The long NMDA time constant at intrinsic synapses allows the slow integration of decision options, instantiating the accumulators of classic sequential sampling models (Ratcliff & Smith, 2004; Smith & Ratcliff, 2004). A common pool of inhibitory interneurons among stimulus-selective pyramidal neurons effectively creates a diffusion process (Bogacz, 2007; Usher & McClelland, 2001), where evidence for one option accumulates at the expense of the other. If intrinsic NMDARs are too strong, however, recurrent dynamics dominate the network's input, amplifying noise and eliminating the advantage of slow evidential buildup. See Wong and Wang (2006) for an analysis of these dynamics in a simplified model. In the model used here, recurrent dynamics strong enough to furnish persistent mnemonic activity are too strong for slow integration under parameters determined by experimental data (see Materials and Methods). In this respect, the difference between earlier findings and ours is the onset of this 'too strong' regime.

There are a number of differences between our simulations and those of earlier studies (Wang, 2002; Wong & Wang, 2006) that may contribute to the difference in network dynamics. A difference of an order of magnitude in intrinsic synaptic conductance strength and a difference of two orders of magnitude in selective input SNR are described above. Additionally, different network architectures were used to simulate tasks where reaction times occur on different timescales and spike rates differ markedly in LIP (visual search vs. random dot motion tasks). Ultimately, the decision making ability of a recurrent network depends on its time constant of integration, reflecting a balance between the leakage and amplification of accumulated input (Usher & McClelland, 2001). This balance has been expressed in terms of the strength and time constant of intrinsic NMDARs (Wang, 2008). As such, there is an optimal NMDAR conductance strength above and below which the network is dominated by amplification and leakage respectively (see the Supplementary Material). The more the conductance exceeds the optimum, the more quickly activation is amplified, leading to earlier choice selection (thus preventing further integration). The more the conductance falls short of the optimum, the more quickly activation reaches a level at which it leaks as fast as it accumulates (also preventing further integration). The optimum in our model is furnished by $\gamma_{NMDA} \approx 0.8$ (Fig. 6), but this value depends on other model parameters, such as the relative strength of excitatory and inhibitory synaptic conductance, the spatial extent of intrinsic interactions governing tuning curves, and the level of background noise in the network. We thus do not claim that our results are general. Indeed, outside the PS regime, the model cannot make decisions if the stimuli offset before discrimination of the target or distractor. We have, however, clearly shown that local circuit PS capability is not a general requirement of biophysically based models of decision circuits. Decision-theoretic analyses have identified biophysical parameters under which models with discrete stimulus-selective populations are equivalent to drift diffusion models in two-choice tasks (Bogacz et al., 2006). An extension of these analyses to the spatial continuum of interactions in centre-surround models (here and e.g. Beck et al., 2008; Furman & Wang, 2008) is an important next step.

4.1. Processing requirements of a salience map

The incompatibility between the processing requirements of decision making and persistent storage in our PPC model is consistent with reports that LIP represents the relative importance (salience, priority) of items in the visual field (Goldberg et al., 2006; Serences & Yantis, 2006). Our model belongs to a family of cortical models (Wilson & Cowan, 1973) in which PS capability entails winner-take-all dynamics in the limit of infinite time (Amari, 1977). The model can therefore support a single active region following stimulus offset, but the time over which the dynamics converge is parameter dependent and potentially within the time constraints of many cognitive tasks (Trappenberg & Standage, 2005). The winner-take-all constraint does not necessarily apply during a stimulus interval, but nonetheless, the strong recurrent dynamics of PS circuits are potentially ill suited to multiple stimulus-driven representations; strong inputs are required to dominate the network's recurrent dynamics, negating the role of intrinsic circuitry. As such, the dynamics of PS networks may be better suited to the representation of one item at a time. Under non-PS parameters, mutual inhibition between regions of the network facilitates competition between stimulus-selective populations, but the recurrent dynamics are weaker than for PS parameters, more easily permitting multiple items to be simultaneously represented, scaled in proportion to the strength of their inputs. In effect, weaker dynamics allow the 'push–pull' of a diffusion process without imposing categorical choice and allow slow transitions between the respective populations dominating the network over time. Both these features would support the representation of salience in LIP. This prediction is consistent with the results of Standage et al. (2005), who found that under non-PS parameters, a population rate model of PPC could explain divergent experimental results on the distribution of visuospatial attention if driven by persistent mnemonic inputs (putatively from PFC). Gradual transitions in the non-PS network can be seen in Fig. 4.

While this class of model is commonly used to simulate visuospatial working memory tasks (e.g. Camperi & Wang, 1998; Compte et al., 2000) due to its support for the spatially periodic configuration of items in many such tasks (e.g. Chafee & Goldman-Rakic, 1998; Funahashi et al., 1989) and for its persistent storage regime, fast winner-take-all dynamics during a memory interval conflict with well-established multi-item capacity constraints of working memory (Cowan, 2001; Luck & Vogel, 1997; Miller, 1956). Our network (in the PS regime) can therefore represent each item of the periodic array, but it can only support one such item over a memory interval. The model can be adapted to support multi-item working memory by structuring the connectivity between pyramidal neurons and inhibitory interneurons (Edin et al., 2009; Macoveanu, Klingberg, & Tegnér, 2006), effectively partitioning the network into functionally separate modules. Mechanisms proposed for the stabilization of persistent mnemonic activity have a similar effect (Trappenberg, 2003), but they do so at the expense of the competitive dynamics required of decision circuitry (Trappenberg & Standage, 2005). We do not expect a given local circuit to account for the full capacity of working memory, but rather, we envision interactions between such circuits. For example, if one circuit were to support the representation of the items in a visual array, persistent storage could be provided by coupled circuits, perhaps one per item. If so, interference between such 'caching' networks might account for working memory capacity constraints. Further work is required to address such possibilities.

4.2. Other mechanisms hypothesized to support persistent mnemonic activity

Earlier studies proposing that persistent storage capability is a requirement of local circuit decision making focused on intrinsic (recurrent) network processing (Wang, 2002, 2008; Wong & Wang, 2006). Our model addresses this hypothesis and therefore continues in this vein, but recurrent synaptic activity is just one mechanism proposed to underlie persistent storage. Other mechanisms include intracellular calcium dynamics (Fransén, 2005; Fransén, Babak, Egorov, Hasselmo, & Alonso, 2006; Winograd, Destexhe, & Sanchez-Vives, 2008); feedforward network oscillations (Lisman & Idiart, 1995); and inter-cortical and cortico-subcortical interactions (see Constantinidis & Wang, 2004; Wang, 2001). While our model is capable of encoding a continuum of feature values such as spatial location, persistent activity encoding these values over a delay period is limited to a single frequency for a given value of NMDAR conductance strength (Fig. 2). Without some form of modulation, the model is therefore unable to simulate graded persistent activity. Such activity has been recorded in cortex during working memory tasks (Barak, Tsodkys, & Romo, 2010; Romo, Brody, Hernandez, & Lemus, 1999) and has been reproduced in a network model that makes decisions in a two-interval discrimination task (Machens, Romo, & Brody, 2005). Similar line attractor dynamics have also been used to model the memory of eye position in the brain stem (Seung, 1996, 1998). It is worth noting that stable persistent activity is generally regarded as a minority case among forms of delay period activity (Durstewitz & Seamans, 2006). More commonly, up and down-ramping activity is seen during these intervals, hypothesized to support prospective and retrospective coding respectively (see Brody, Romo, & Kepecs, 2003) as well as the encoding of temporal intervals (see Durstewitz & Seamans, 2006). Recently, ramping activity has been proposed to modulate local circuit dynamics during decisions, driving a transition from outside to inside the PS regime, where the rate of transition governs the speed–accuracy trade-off (Standage et al., in press).

4.3. Local and distributed processing

We have presented our findings in the context of sequential sampling models, where in the visuospatial domain, a single decision circuit integrates evidence for spatial locations until one representation exceeds a threshold level of activity, leading to an eye movement. This role of eye movement decision maker has been attributed to several cortical regions, including PPC (Roitman & Shadlen, 2002) and FEF (Hanes & Schall, 1996), as well as to the mid-brain superior colliculus (Paré & Hanes, 2003). We have further emphasized the decision making abilities of our model under parameters that either do or do not support PS, but it may not be necessary to draw categorical distinctions between PS and non-PS networks in the domain of decision making, nor between the physiological properties of cortical regions correlated with eye movement decisions (Chafee & Goldman-Rakic, 1998). By manipulating the strength of intrinsic NMDARs, we show a gradient of network dynamics and consequent speed–accuracy trade-offs (Fig. 6). The PS border sits on this gradient, but may be epiphenomenal in this context. In a framework of distributed decision making, a range of computational properties are conferred along the gradient, including PS. At one extreme, the strongest dynamics yield PS states robust to distractor stimuli, whereas somewhat weaker dynamics (eg. PS baseline) yield PS states more readily subject to interference (Compte et al., 2000). Depending on task demands, networks with both these properties would provide useful input to other brain regions directly involved in eye movement production, such as FEF and SC. At the other extreme are non-committal noise filters with dynamics too weak to make categorical decisions in difficult tasks. Such slow, conservative 'advice' would also be useful downstream, potentially balancing any errors from more decisive circuits. In our model, the behaviour of sequential sampling models is furnished by parameters between these extremes ($0.7 \leq \gamma_{NMDA} \leq 0.9$) where the speed–accuracy trade-off resembles experimental data (eg. Palmer et al., 2005). Clearly, networks in this range would be useful to downstream decision-related structures.

These results are consistent with a widely held view of eye movement decisions where no single circuit is responsible for integrating sensory evidence or making decisions (Schall, 2001). We posit that networks in cortical regions such as PFC, FEF and PPC, frequently correlated with integration of decision options, may play different roles in integrating these options by virtue of the strength of their dynamics. For example, the winner-take-all dynamics of PS networks would appear ideal for caching decisions and providing categorical bias to circuits involved in sensory processing, consistent with the biased competition theory of attention (Desimone & Duncan, 1995). As discussed above, weaker dynamics may play a complementary role, more readily allowing multiple items to be simultaneously considered by downstream decision-related structures, consistent with the concept of a salience map (Koch & Ullman, 1985; Treisman & Gelade, 1980). There is, of course, the possibility that the dynamics of decision circuits are modulated by task demands. For example, the same circuit could mediate PS and a salience map by modulation of intrinsic NMDARs, consistent with reports of increased dopaminergic activity during working memory tasks and dopamine enhancement of NMDA conductance in PFC (see Durstewitz et al., 2000).

Finally, earlier proposals that decision circuits should support PS (Salinas & Sejnowski, 2001; Wang, 2002, 2008; Wong & Wang, 2006) may have been influenced by the memory component of delayed response tasks; in single-circuit models in which persistent mnemonic activity and decision making are supported by the same mechanism, PS capability is required *a priori* to simulate these tasks. Similarly, PS capability guarantees categorical choice in single-circuit simulations of delayed response tasks, even in the absence of information to guide that choice (Wang, 2002). Given the general acknowledgement that persistent mnemonic activity may be supported by inter-circuit mechanisms in addition to intra-circuit ones (Chafee & Goldman-Rakic, 1998, 2000), this possibility highlights the need for coupled circuit models to guide further experiments. For instance, if LIP is not a PS network *per se*, then persistent activity in this cortical area must either be driven by activity somewhere else, such as PFC (see Constantinidis & Wang, 2004), or distinct parietal networks including LIP may be differentiated by their dynamics, as demonstrated by our simulations. Frontoparietal connectivity and the contributions of PFC and PPC circuits to working memory processing are receiving considerable attention (Babiloni et al., 2004; Chafee & Goldman-Rakic, 2000; curtis, Rao, & D'Esposito, 2004; Edin, Klingberg, Stodberg, & Tegnér, 2007; McNab & Klingberg, 2008). Similar attention is required in the domain of decision making.

If decision making relies on NMDARs for integration of evidence, it should be possible to interfere with decision making by pharmacological manipulation of NMDARs, as shown previously for persistent mnemonic activity and working memory more generally (Aura & Riekkinen, 1999; Dudkin et al., 1997). Recent experimental works supports this hypothesis, where the performance of monkeys in a visual discrimination task improved with low doses of the NMDA antagonist Ketamine, before deteriorating at higher doses (Shen, Kalwarowsky, Clarence, Brunamonti, & Paré, 2010). These findings are consistent with our simulations of PPC, where

for a range of values of intrinsic NMDAR strength, network performance improved before deteriorating at lower values (Fig. 6). Further experiments are required to constrain pharmacological impairment of NMDA to cortical regions such PFC and PPC during decision making tasks.

Acknowledgements

This work was supported by the Canadian Institutes of Health Research. We thank Kevin Johnston and Thomas Trappenberg for helpful comments.

Appendix. Supplementary data

Supplementary material related to this article can be found online at doi:10.1016/j.neunet.2011.05.004.

References

Abeles, M. (1991). *Corticonics: neural circuits of the cerebral cortex*. Cambridge, UK: Cambridge University Press.
Amari, S. (1977). Dynamics of pattern formation in lateral-inhibition type neural fields. *Biological Cybernetics*, *27*, 77–87.
Ardid, S., Wang, X.-J., & Compte, A. (2007). An integrated microcircuit model of attentional processing in the neocortex. *Journal of Neurological Sciences*, *27*, 8486–8495.
Aura, J., & Riekkinen, P. J. (1999). Blockade of NMDA receptors located at the dorsomedial prefrontal cortex impairs spatial working memory in rats. *Neuroreport*, *10*, 243–248.
Babiloni, C., Babiloni, F., Carducci, F., Cincotti, F., Vecchio, F., Cola, B., Rossi, S., Miniussi, C., & Rossini, P. M. (2004). Functional frontoparietal connectivity during short-term memory as revealed by high-resolution EEG coherence analysis. *Behavioral Neuroscience*, *118*, 687–697.
Barak, O., Tsodkys, M., & Romo, R. (2010). Neural population coding of parametric working memory. *Journal of Neurological Sciences*, *30*, 9424–9430.
Beck, J. M., Ma, W. J., Kiani, R., Hanks, T., Churchland, A. K., Roitman, J., Shadlen, M. N., Latham, P. E., & Pouget, A. (2008). Probabilistic population codes for Bayesian decision making. *Neuron*, *60*, 1142–1152.
Bogacz, R., Brown, E., Moehlis, J., Holmes, P., & Cohen, J. D. (2006). The physics or optimal decision making: a formal analysis of models of performance in two-alternative forced-choice tasks. *Psychological Review*, *113*, 700–765.
Bogacz, R. (2007). Optimal decision-making theories: linking neurobiology with behaviour. *Trends in Cognitive Science*, *11*, 118–125.
Brody, C. D., Romo, R., & Kepecs, A. (2003). Basic mechanisms for graded persistent activity: discrete attractors, continuous attractors, and dynamic representations. *Current Opinion in Neurobiology*, *13*, 204–211.
Bruce, C. J., & Goldberg, M. E. (1985). Primate frontal eye fields. I. Single neurons discharging before saccades. *Journal of Neurophysiology*, *53*, 603–635.
Camperi, M., & Wang, X.-J. (1998). A model of visuospatial working memory in prefrontal cortex: recurrent network and cellular bistability. *Journal of Computational Neuroscience*, *5*, 383–405.
Chafee, M. V., & Goldman-Rakic, P. S. (1998). Matching patterns of activity in primate prefrontal area 8a and parietal area 7ip neurons during a spatial working memory task. *Journal of Neurophysiology*, *79*, 2918–2940.
Chafee, M. V., & Goldman-Rakic, P. S. (2000). Inactivation of parietal and prefrontal cortex reveals interdependence of neural activity during memory-guided saccades. *Journal of Neurophysiology*, *83*, 1550–1566.
Churchland, A. K., Kiani, R., & Shadlen, M. N. (2008). Decision-making with multiple alternatives. *Nature Neuroscience*, *11*, 693–702.
Cisek, P. (2006). Integrated neural processes for defining potential actions and deciding between them: a computational model. *Journal of Neurological Sciences*, *26*, 9761–9770.
Cohen, J. Y., Pouget, P., Woodman, G. F., Subraveti, C. R., Schall, J. D., & Rossi, A. F. (2007). Difficulty of visual search modulates neuronal interactions and response variability in the frontal eye field. *Journal of Neurophysiology*, *98*, 2580–2587.
Compte, A., Brunel, N., Goldman-Rakic, P. S., & Wang, X.-J. (2000). Synaptic mechanisms and network dynamics underlying spatial working memory in a cortical network model. *Cerebral Cortex*, *10*, 910–923.
Constantinidis, C., & Wang, X.-J. (2004). A neural circuit basis for spatial working memory. *The Neuroscientist*, *10*, 553–565.
Cowan, N. (2001). The magical number 4 in short-term memory: a reconsideration of mental storage capacity. *Behavioral and Brain Sciences*, *24*, 87–185.
Cull-Candy, S. G., Brickley, S., & Farrant, M. (2001). NMDA receptor subunits: diversity, development and disease. *Current Opinion in Neurobiology*, *11*, 327–335.
Cull-Candy, S. G., & Leszkiewicz, D. N. (2004). Role of distinct NMDA receptor subtypes at central synapses. *Science STKE*, *2004*, re16.
Curtis, C. E., Rao, V. Y., & D'Esposito, M. (2004). Maintenance of spatial and motor codes during oculomotor delayed response tasks. *Journal of Neurological Sciences*, *24*, 3944–3952.
Desimone, R., & Duncan, J. (1995). Neural mechanisms of selective visual attention. *Annual Review of Neuroscience*, *18*, 193–222.
Destexhe, A., & Paré, D. (1999). Impact of network activity on the integrative properties of neocortical pyramidal neurons in vivo. *Journal of Neurophysiology*, *81*, 1531–1547.
Douglas, R. J., & Martin, K. A. C. (2004). Neuronal circuits of the neocortex. *Annual Review of Neuroscience*, *27*, 419–451.
Douglas, R. J., & Martin, K. A. C. (2007). Recurrent neuronal circuits in the neocortex. *Current Biology*, *17*, R496–R500.
Dudkin, K. N., Kruchinin, V. K., & Chueva, I. V. (1997). Effect of NMDA on the activity of cortical glutaminergic structures in delayed visual differentiation in monkeys. *Neuroscience and Behavioral Physiology*, *27*, 153–158.
Durstewitz, D., Seamans, J. K., & Sejnowski, T. J. (2000). Neurocomputational models of working memory. *Nature Neuroscience*, *3*, 1184–1191.
Durstewitz, D., & Seamans, J. K. (2006). Beyond bistability: biophysics and temporal dynamics of working memory. *Neuroscience*, *139*, 119–133.
Edin, F., Klingberg, T., Johansson, P., McNab, F., Tegnér, J., & Compte, A. (2009). Mechanism for top-down control of working memory capacity. *Proceedings of the National Academy of Sciences USA*, *106*, 6802–6807.
Edin, F., Klingberg, T., Stodberg, T., & Tegnér, J. (2007). Fronto-parietal connection asymmetry regulates working memory distractibility. *Journal of Integrative Neuroscience*, *6*, 567–596.
Fransén, E., & Lansner, A. (1995). Low spiking rates in a population of mutually exciting pyramidal cells. *Network: Computation in Neural Systems*, *6*, 271–288.
Fransén, E. (2005). Functional role of entorhinal cortex in working memory processing. *Neural Networks*, *18*, 1141–1149.
Fransén, E., Babak, T., Egorov, A. V., Hasselmo, M. E., & Alonso, A. A. (2006). Mechanism of graded persistent cellular activity of entorhinal cortex layer 5 neurons. *Neuron*, *49*, 735–746.
Funahashi, S., Bruce, C. J., & Goldman-Rakic, P. S. (1989). Mnemonic coding of visual space in the monkey's dorsolateral prefrontal cortex. *Journal of Neurophysiology*, *61*, 331–349.
Furman, M., & Wang, X.-J. (2008). Similarity effect and optimal control of multiple-choice decision making. *Neuron*, *60*, 1153–1168.
Fuster, J. (1973). Unit activity in prefrontal cortex during delayed-response performance: neuronal correlates of transient memory. *Journal of Neurophysiology*, *36*, 61–78.
Galarreta, M., & Hestrin, S. (1998). Frequency-dependent synaptic depression and the balance of excitation and inhibition in the neocortex. *Nature Neuroscience*, *1*, 587–594.
Gnadt, J. W., & Andersen, R. A. (1988). Memory related motor planning activity in posterior parietal cortex of macaque. *Experimental Brain Research*, *70*, 216–220.
Goldberg, M. E., Bisley, J. W., Powell, K. D., & Gottlieb, J. (2006). Saccades, salience and attention: the role of the lateral intraparietal area in visual behavior. *Progress in Brain Research*, *155*, 157–175.
Goldman-Rakic, P. (1995). Cellular basis of working memory. *Neuron*, *14*, 477–485.
Gonzalez-Burgos, G., Kroener, S., Zaitsev, A. V., Povysheva, N. V., Krimer, L. S. , Barrionuevo, G., & Lewis, D. (2008). Functional maturation of excitatory synapses in Layer 3 pyramidal neurons during postnatal development of the primate prefrontal cortex. *Cerebral Cortex*, *18*, 626–637.
Green, D. M., & Swets, J. A. (1966). *Signal detection theory and psychophysics*. New York: Wiley.
Gutkin, B. S., Laing, C. R., Colby, C. L., Chow, C. C., & Ermentrout, G. B. (2001). Turning on and off with excitation: the role of spike timing asynchrony and synchrony in sustained neural activity. *Journal of Computational Neuroscience*, *11*, 121–134.
Hanes, D. P., & Schall, J. D. (1996). Neural control of voluntary movement initiation. *Science*, *274*, 427–430.
Hasegawa, R. P., Matsumoto, M., & Mikami, A. (2000). Search target selection in monkey prefrontal cortex. *Journal of Neurophysiology*, *84*, 1692–1696.
Jahr, C. E., & Stevens, C. F. (1990). Voltage dependence of nmda-activated macroscopic conductances predicted by single-channel kinetics. *Journal of Neurological Sciences*, *10*, 3178–3182.
Koch, C., & Ullman, S. (1985). Shifts in selective visual attention: towards the underlying neural circuitry. *Human Neurobiology*, *4*, 219–227.
Kumar, S. S., & Huguenard, J. R. (2003). Pathway-specific differences in subunit composition of synaptic NMDA receptors on pyramidal neurons in neocortex. *Journal of Neurological Sciences*, *23*, 10074–10083.
Lisman, J. E., & Idiart, M. A. P. (1995). Storage of $7 + -2$ short-term memories in oscillatory subcycles. *Science*, *267*, 1512–1515.
Lisman, J., Fellous, J., & Wang, X.-J. (1998). A role for NMDA-receptor channels in working memory. *Nature Neuroscience*, *1*, 273–275.
Luck, S. J., & Vogel, E. K. (1997). The capacity of visual working memory for features and conjunctions. *Nature*, *390*, 279–281.
Ma, J. M., Beck, J. M., Latham, P. E., & Pouget, A. (2006). Bayesian inference with probabilistic population codes. *Nature Neuroscience*, *9*, 1432–1438.
Machens, C. K., Romo, R., & Brody, C. D. (2005). Flexible control of mutual inhibition: a neural model of two-interval discrimination. *Science*, *307*, 1121–1124.
Macoveanu, J., Klingberg, T., & Tegnér, J. (2006). A biophysical model of multiple-item working memory: a computational and neuroimaging study. *Neuroscience*, *141*, 1611–1618.
Miller, G. A. (1956). The magical number seven, plus or minus two: some limits on our capacity for processing information. *Psychological Review*, *63*, 81–97.
McNab, F., & Klingberg, T. (2008). Prefrontal cortex and basal ganglia control access to working memory. *Nature Neuroscience*, *11*, 103–107.
Palmer, J., Huk, A. C., & Shadlen, M. N. (2005). The effect of stimulus strength on the speed and accuracy of a perceptual decision. *Journal of Vision*, *5*, 376–404.

Paré, M., & Hanes, D. P. (2003). Controlled movement processing: superior colliculus activity associated with countermanded saccades. *Journal of Neurological Sciences*, *23*, 6480–6489.
Paré, M., & Wurtz, R. H. (1997). Monkey posterior parietal cortex neurons antidromically activated from superior colliculus. *Journal of Neurophysiology*, *78*, 3493–3497.
Paré, M., & Wurtz, R. H. (2001). Progression in neuronal processing for saccadic eye movements from parietal cortex area LIP to Superior Colliculus. *Journal of Neurophysiology*, *85*, 2545–2562.
Pouget, A., Dayan, P., & Zemel, R. (2000). Information processing with population codes. *Nature Reviews Neuroscience*, *1*, 125–132.
Prescott, S. A., & De Koninck, Y. (2003). Gain control of firing rate by shunting inhibition: roles of synaptic noise and dendritic saturation. *Proceedings of the National Academy of Sciences USA*, *100*, 2076–2081.
Ratcliff, R., & Smith, P. L. (2004). A comparison of sequential sampling models for two-choice reaction time. *Psychological Review*, *111*, 333–367.
Roitman, J. D., & Shadlen, M. N. (2002). Response of neurons in the lateral intraparietal area during a combined visual discrimination reaction time task. *Journal of Neurological Sciences*, *22*, 9475–9489.
Romo, R., Brody, C. D., Hernandez, A., & Lemus, L. (1999). Neuronal correlates of parametric working memory in the prefrontal cortex. *Nature*, *399*, 470–473.
Salin, P. A., & Prince, D. A. (1996). Spontaneous $GABA_A$ receptor-mediated inhibitory currents in adult rat somatosensory cortex. *Journal of Neurophysiology*, *75*, 1573–1588.
Salinas, E., & Sejnowski, T. J. (2001). Gain modulation in the central nervous system: where behavior, neurophysiology, and computation meet. *The Neuroscientist*, *7*, 430–440.
Schall, J. D. (2001). Neural basis of deciding, choosing and acting. *Nature Reviews Neuroscience*, *2*, 33–42.
Schall, J. D., & Hanes, D. P. (1993). Neural basis of saccade target selection in frontal eye field during visual search. *Nature*, *366*, 467–469.
Serences, J. T., & Yantis, S. (2006). Selective visual attention and perceptual coherence. *Trends in Cognitive Science*, *10*, 38–45.
Seung, H. S. (1996). How the brain keeps the eyes still. *Proceedings of the National Academy of Sciences USA*, *93*, 13339–13344.
Seung, H. S. (1998). Continuous attractors and oculomotor control. *Neural Networks*, *11*, 1253–1258.
Shen, K., Kalwarowsky, S., Clarence, W., Brunamonti, E., & Paré, M. (2010). Beneficial effects of the NMDA antagonist Ketamine on decision processes in visual search. *Journal of Neurological Sciences*, *30*, 9947–9953.
Smith, P. L., & Ratcliff, R. (2004). Psychology and neurobiology of simple decisions. *Trends in Neuroscience*, *27*, 161–168.
Standage, D. I., Trappenberg, T. P., & Klein, R. M. (2005). Modelling divided visual attention with a winner-take-all network. *Neural Networks*, *18*, 620–627.
Standage, D., You, H., Wang, D., & Dorris, M. C. (2011). Gain modulation by an urgency signal controls the speed-accuracy trade-off in a network model of a cortical decision circuit. *Frontiers in Computational Neuroscience*, *5* (7) in press (doi:10.3389/fncom.2011.00007).
Tegnér, J., Compte, A., & Wang, X.-J. (2002). The dynamical stability of reverberatory neural circuits. *Biological Cybernetics*, *87*, 471–481.
Thomas, N. W. D., & Paré, M. (2007). Temporal processing of saccade targets in parietal cortex area lip during visual search. *Journal of Neurophysiology*, *97*, 942–947.
Thompson, K., Hanes, D., Bichot, N., & Schall, J. (1996). Perceptual and motor processing stages identified in the activity of macaque frontal eye field. *Journal of Neurophysiology*, *76*, 440–455.
Trappenberg, T. P. (2003). Why is our capacity of working memory so large? *Neural Information Processing — Letters and Reviews*, *1*, 97–101.
Trappenberg, T. P., Dorris, M. C., Munoz, D. P., & Klein, R. M. (2001). A model of saccade initiation based on the competitive integration of exogenous and endogenous signals in the superior colliculus. *Journal of Cognitive Neuroscience*, *13*, 256–271.
Trappenberg, T. P., & Standage, D. I. (2005). Multi-packet regions in stabilized continuous attractor networks. *Neurocomputing*, *65–66*, 617–622.
Treisman, A. M., & Gelade, G. (1980). A feature-integration theory of attention. *Cognitive Psychology*, *12*, 97–136.
Tuckwell, H. (1988). *Introduction to theoretical neurobiology*. Cambridge: Cambridge University Press.
Usher, M., & McClelland, J. L. (2001). On the time course of perceptual choice: the leaky competing accumulator model. *Psychological Review*, *108*, 550–592.
Wang, X.-J. (1999). Synaptic basis of cortical persistent activity: the importance of NMDA receptors to working memory. *Journal of Neurological Sciences*, *19*, 9587–9603.
Wang, X.-J. (2001). Synaptic reverberation underlying mnemonic persistent activity. *Trends in Neuroscience*, *24*, 455–463.
Wang, X.-J. (2002). Probabilistic decision making by slow reverberation in cortical circuits. *Neuron*, *36*, 955–968.
Wang, X.-J. (2008). Decision making in recurrent neuronal circuits. *Neuron*, *60*, 215–234.
Wang, H., Stradtman, G. G., III, Wang, X.-J, & Gao, W.-J. (2008). A specialized NMDA receptor function in layer 5 recurrent microcircuitry of the adult rat prefrontal cortex. *Proceedings of the National Academy of Sciences USA*, *105*, 16791–16796.
White, E. L. (1989). *Cortical circuits: synaptic organization of the cerebral cortex; structure, function and theory*. Boston: Birkhauser.
Wilson, H. R., & Cowan, J. D. (1973). A mathematical theory of the functional dynamics of cortical and thalamic nervous tissue. *Kybernetik*, *13*, 55–80.
Winograd, M., Destexhe, A., & Sanchez-Vives, M. V. (2008). Hyperpolarization-activated graded persistent activity in the prefrontal cortex. *Proceedings of the National Academy of Sciences USA*, *105*, 7298–7203.
Wong, K.-F., Huk, A. C, Shadlen, M., & Wang, X.-J. (2007). Neural circuit dynamics underlying accumulation of time-varying evidence during perceptual decision making. *Frontiers in Computational Neuroscience*, *1*, 1–11.
Wong, K.-F., & Wang, X.-J. (2006). A recurrent network mechanism of time integration in perceptual decisions. *Journal of Neurological Sciences*, *26*, 1314–1328.